QUANTITATIVE PATHOLOGY USING DEEP LEARNING

BY

MICHAEL JOHN FANOUS

DISSERTATION

Submitted in partial fulfillment of the requirements
for the degree of Doctor in Philosophy in Bioengineering
in the Graduate College of the
University of Illinois Urbana-Champaign, 2022

Urbana, Illinois

Doctoral Committee:

Professor Mark Anastasio, Chair
Associate Professor Wawrzyniec Dobrucki
Professor Michael Insana
Professor Brad Sutton

ABSTRACT

The subfield of pathology known as ‘digital pathology’ encompasses the procedures for image acquisition, organization, distribution, labeling, and computational analysis.

Digital pathology is expanding quickly and has already produced a remarkable impact in academia and business[1]. For research, clinical trials, telehealth, remote image processing, and overall patient treatment, the capacity to quickly transmit and evaluate a considerable volume of pathology data is revolutionary[2]. The use of artificial intelligence is at the center of this new wave of innovation, dieselizing the astonishing advancements in this increasingly digital climate.

This Ph.D. thesis is centered around developing advanced pathology machine learning tools *to enhance both the analysis and measurement of pathology samples.* This dissertation provides a summary of my main pathology related research results, in chronological order, comprising an evolution in machine learning complexity applied to the quantitative assessment of pathology samples.

First, I studied pancreatic ductal adenocarcinoma (PDAC) tissue fiber properties using a segmentation algorithm, which constitutes a good reference point for automating the dissection of specific features in tissue biopsies to derive clinically relevant statistics.

After being approached by Abbott Laboratories to help examine the myelin content in certain areas of the brain, we used our research group’s quantitative phase imaging techniques to image 19 piglet brain tissue slides. I applied both manual segmentation schemes and deep learning methods to correlate the tissue properties with related size and diet statistics of the tissue subjects.

The results *exceeded our expectations* in terms of discernment capabilities at the single frame level, a task altogether impossible for an expert histopathologist.

Additionally, a series of blood smears slides were imaged and subjected to various deep learning devices to not only bypass the need for the standard Wright's stain, but automatically delineate and label four major white blood cell groups.

Finally, in an effort to simplify the pathology slide scanning procedure altogether, and after various attempts and approaches, we arrived at what is now termed 'GANscan.'

This is a deep learning microscopy method that enables a *thirtyfold increase* in whole-slide scanning durations using standard equipment and software. This technique has recently been reviewed and declared a "transformative solution [that] can be used to further accelerate the adoption of digital pathology"[3] by the eminent scientist Professor Ozcan in a review article on our technique.

ACKNOWLEDGEMENTS

I would like to thank, first and foremost, my late advisor Professor Gabriel Popescu, who was a brilliant scientist, a tremendous teacher, and a personal friend. This past summer marked the sudden and tragic passing of Professor Popescu, a colossal loss for the scientific community worldwide.

I would also like to express my gratitude to all my colleagues in the QLI research group for their help and camaraderie throughout my Ph.D. program, including Dr. Hassaan Majeed, Dr. Mikhail Kandel, Young Jae Lee, Masayoshi Sakakura, Yuchen He, Yunlei Zhao, Sajeeb Chowdhury, Xi Chen, Kelly Zhang, Neha Goswami, and Dr. Chenfei Hu.

In addition, I must acknowledge my other collaborators over the years, without whom my work would not have been possible, including Dr. Catherine Best-Popescu, Sourya Sengupta, Dr. Sheghua He, Dr. Krishnarao Tangella, Dr. Megan P. Caputo, Dr. Yanfen Li, Dr. Kristopher A. Kilian, Chuqiao Shi, Dr. Laurie A. Rund, Dr. Rodney W. Johnson, Dr. Tapas Das, Dr. Matthew J. Kuchan, Adib Keikhosravi, Dr. Andre Kajdascy-Balla, Dr. Kevin W. Eliceiri, and Dr. Nahil Sobh.

Finally, I would like to thank Professor Mark A. Anastasio very much for agreeing on short notice to chair the committee in Dr. Popescu's place. Also, I am grateful to the other members of my doctoral thesis committee for all their help and constructive criticism, namely Professor Michael Insana, Professor Brad Sutton, and Professor Wawrzyniec Dobrucki.

TABLE OF CONTENTS

CHAPTER 1: Introduction

1.1 Background and Approach

Image acquisition, management, distribution, annotation, and computer-aided analysis are all included in the subfield of pathology known as digital pathology.

Breakthroughs in digital pathology are occurring at an increasing rate, and a number of very sophisticated platforms are already established in academia and business[1]. Research, clinical trials, telemedicine, downstream image analysis, and overall patient care are transformed by the ability to quickly transmit and evaluate huge amounts of pathology data[2]. High throughput scanning microscopes, which are at the core of this revolution, comprise the first step and foundation of this rapidly evolving field. The use of several new scanning microscopes and their digital pictures by pathologists in their clinical workflow for primary diagnosis has already been authorized by regulatory bodies.

The next Machine Learning (ML) revolution in histopathology will undoubtedly be propelled by increasingly extensive annotated databases. The speed and throughput of modern digital pathology scanners, though, are among the main bottlenecks to all the related headway downstream. Each histology slide can produce gigapixels worth of data when scanned in its entirety (with an objective lens of 40/0.75NA, for example). Although recent improvements in hardware and software have sped up scanning times[2,4], there is still a rate-limiting step that hinders innovation in the field. This is because high-throughput scanners cost between $150K and $300K, making them few in number in many deployment spaces because buying multiple scanners is not economically viable.

The mechanical requirements of the scanning stage are frequently what cause the scanning speed rate-limiting step for a standard brightfield scanning microscope

There have been numerous initiatives to speed up the entire scanning of these microscopes.

One possibility is to upgrade the microscope apparatus with hardware elements, such as coded illumination[5-8], which necessitates a post-processing computing step to decode the encoded specimen data[9].

More recently, machine learning (ML) algorithms were used to speed up digital microscopic scanning. This included improvements in resolution, depth of field, and refocusing capabilities[10]. Also available now is the ability to computationally generate multiple stains on the same tissue section, which effectively speeds up the imaging process by multiplying the useful information channels from each slide[11].

In this thesis, I report on machine learning analysis techniques to study pathology slides, as well as on a novel technique for enhancing whole-slide scanning speeds[12].

The analysis section of this thesis will be related to quantitative pathology of pancreatic ductal carcinoma (PDAC), myelin content in the internal capsule, and white blood cells (WBCs) in blood smears.

The whole-slide scanning innovation, coined GANscan, works by switching from the *conventional "stop-and-stare" imaging approach to a continuous scanning strategy*. The resulting image is recreated by using a machine learning-based image restoration approach on a motion-blurred scanned image. This deep learning-based method replaces the requirement for specialized add-on hardware components and is applied on a common scanning microscope.

The method's primary contribution is decoupling the imaging speed from the stage movement. We used the Pix2Pix image translation framework[13] to accomplish this purpose. In this instance, the rapid movement of the stage causes a severely motion-blurred image, which serves as the input, but the label is a sharp, high-resolution image taken at regular speeds. This supervised

image-to-image translation[14] strategy, built on a Generative Adversarial Network (GAN)[15] model, enables pixel-level reconstructions of blurry images through precisely paired registered pictures.

A Generator and a Discriminator are the two competing networks that make up GANs. The Generator's job is to take an input image—in this case, one with significant motion blur—and produce an image that resembles the matched label, while the Discriminator's job is to provide feedback on the Generator's performance. The Generator is forced by the Discriminator to match the labels' sample distribution, producing outputs that are clear and convincing-looking.

After being trained, the deep neural network is used to deblur images that had been continually scanned at stage speeds of up to 5000 µm/s with an acquisition rate of 30 fps, or roughly 1.8 GPixels in 100 seconds, using a typical high throughput scanning microscope. The ground truth photos were taken at a stage speed of 50 µm/s, or 100 times slower, for comparison (see Figure 1.1).

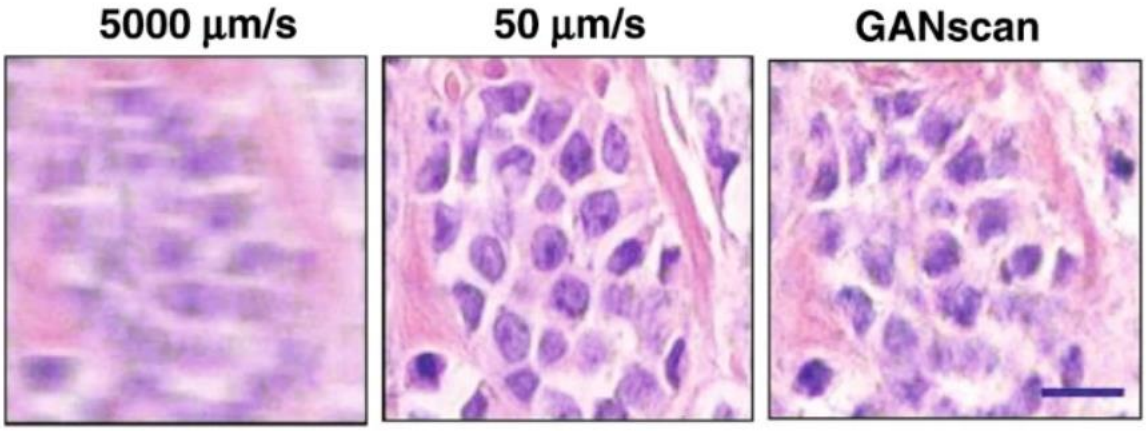

Figure 1.1 A demonstration of motion deblurring by GANscan.

We illustrate this using a variety of biopsies and tissue components, as well as brightfield and phase contrast microscopy methods.

Additionally, our method has demonstrated *outstanding success* for imaging a sample that is defocused by +/-5 μm. This is crucial for any potential practical application of the approach because defocusing is a common issue for these scanners (especially at high magnifications), and the significant speed boost *(X 30 times faster*) that this all-algorithmic method has achieved would have been largely lost with the increased number of focus correction steps.

By enhancing scanning microscope throughput, this strategy can improve clinical and research workflows and boost the use of digital pathology.

Without extra hardware alterations, it may make use of microscopes that are already in use in clinical settings. In general, our approach can power future computer-aided diagnosis systems and assist in democratizing research.

1.2 Thesis Overview

This thesis is organized as follows. In Chapter 2, I discuss a segmentation algorithm to investigate the fiber characteristics of pancreatic ductal adenocarcinoma (PDAC) tissue, which serves as a useful benchmark for automating the dissection of particular features in tissue biopsies to produce clinically useful statistics.

In Chapter 3 & 4, I discuss the outcome of Abbott Laboratories contacting our research group to assist in examining the myelin content in certain regions of the brain. I will explain the use of both manual segmentation systems and deep learning techniques. The results shown have exceeded our expectations in terms of single-frame discerning abilities, which is a task that would be completely beyond the scope of a skilled histopathologist.

In Chapter 5, I describe the work I have done on blood smear slides. The samples were scanned and exposed to a variety of deep learning tools in order to not only do away with the

conventional Wright's stain, but also automatically delineate and annotate four main white blood cell types.

I end with Chapter 6, wherein I discuss the culmination of my work as a Ph.D. candidate, namely how I arrived at what is now referred to as "GANscan", after making numerous attempts to streamline the pathology slide scanning process. Using common tools and software, this deep learning microscopy technique increases whole-slide scanning times by a factor of thirty.

CHAPTER 2: Quantitative Pathology of Pancreatic Cancer

2.1 Abstract

New quantitative prognostic markers are needed for improved pancreatic ductal adenocarcinoma (PDAC) prognosis. Second harmonic generation microscopy has been used to show that collagen fiber alignment in PDAC is a negative prognostic factor. In this work, a series of PDAC and normal adjacent tissue (NAT) biopsies were imaged with Spatial Light Interference Microscopy (SLIM). Quantitative analysis performed on the biopsy SLIM images show that PDAC fiber structures have lower alignment per unit length, narrower width, and are longer than NAT controls. Importantly, fibrillar collagen in PDAC shows an inverse relationship between survival data and fiber width and length ($p<0.05$).

2.2 Motivation and Overview

Globally, pancreatic cancer is the 12th most common malignancy and the seventh and eighth cause of cancer-related death in men and women, respectively [16]. Its occurrence is growing exponentially, and it is projected to be the second most lethal cancer in the US by 2020 [17]. Approximately 85% of pancreatic malignancies are classified as ductal adenocarcinomas. Pancreatic abnormalities are first confirmed and partially diagnosed through conventional imaging, such as helical computed tomography (CT) [18], contrast-enhanced ultrasound (US) [19], and enhanced magnetic resonance imaging (MRI) [20].^{18}F Fluorodeoxyglucose (FDG) positron emission tomography (PET) has emerged as another method that can detect malignant pancreatic tumors with high sensitivity and specificity [21]. Endoscopic ultrasound - guided fine-needle aspiration

biopsy is a reliable technique for classifying tissue of suspected PDAC patients [22,23], though it can produce false negative results [24].

When a suspicious region is indicated by imaging, a tissue biopsy is obtained and prepared for pathology examination with hematoxylin and eosin (H&E) staining. Diagnosis by a pathologist for most cancers is typically highly accurate, although sometimes the subjective human investigation results in inter-observer variability [25]. Prognosis of pancreatic cancer, on the other hand, is far less definitive, having the weakest record among digestive tract cancers [26]. It remains a challenge to ascertain the prospects of recovery after PDAC surgery, as well as the degree of a possible disease regression [27]. After tumoral excisions, more than 75% of PDAC patients have a survival period of less than 5 years. This poor outcome is due to residual lesions left behind by surgery or new metastasis sites, which lead to relapse [28-31].

One of the ongoing deficiencies in PDAC management is the lack of unique detectable qualities that can predict the likely course of the disease. The ability to evaluate the risk of systemic recurrence is vital, as it can help exclude the need for aggressive options, such as vascular resection and reconstruction [32]. PDAC tissue may be readily identified by its pronounced desmoplasia, which is composed of extracellular matrix (ECM) molecules, pancreatic stellate cells (PSCs), as well as other substances, such as cytokines, growth factors, and ECM metabolizing enzymes secreted by the immune system [33]. Recent efforts have demonstrated a strong correlation between stromal microenvironments and patient outcome [34]. It has been found that the extent of organization and symmetry in stromal ECM, particularly in the fibrillar collagen region, plays a critical role in tumor development [35-37]. During cancer progression, the structural integrity of fibrillar collagen is compromised, which leads to tissue strengthening, mechanical interactions [38], a change in metabolites [39] and conditions conducive to cell infiltration [35]. It has recently been

shown that PDAC-associated stroma has a markedly aligned configuration, differentiating it from that in benign pancreatic stroma [40]. Furthermore, it was found that stromal collagen alignment has significant potential as a quantifiable PDAC biomarker and is linked to patient survival following surgery [27]. These observations were first made using second-harmonic generation microscopy (SHGM) [41] which is specific to non-centrosymmetric structures, such as collagen fibers. SHGM is a valuable research tool, but might offer limited adoption in the clinic, as it uses bulky and expensive instrumentation and has limited throughput due to raster scanning. The LC-PolScope, an enhanced form of polarized light microscopy [42], has been proposed as a suitable alternative to SHGM for quantitatively imaging fibrillar collagen in tissues, and compared well against SHGM using breast and pancreatic cancer pathology slides [43]. It was shown that the LC-PolScope, a more economic, and simpler system to SHGM, can be used successfully for the quantification of collagen fibers in terms of orientation and alignment [43].

Though it is convenient to use imaging modalities that are specifically sensitive to fibrillar collagen such as SHGM and LC-PolScope, acquiring signal from other tissue features has advantages. For instance, it is constructive to have a comprehensive representation of a biopsy core, cell, ducts and matrix included, for label free diagnosis in surgical pathology. We present that spatial light interference microscopy (SLIM) [44] can be used for this purpose. Recently, it has been shown that similar collagen information can be extracted using SLIM, which is less expensive than SHGM and can be as much as a factor of ~1,000 faster [45]. Specifically, the collagen fiber orientation in cancerous breast tissue was quantified based on SLIM data [45]. It was shown that the composition, orientation, and alignment of collagen fibers in tumor-adjacent stroma affect tumor growth and metastasis. SLIM is not only sensitive to this fiber orientation but can also detect other components of the tumor biopsy such as tumor cells [46].

In this chapter, we use SLIM as a label-free quantitative phase imaging (QPI) technique [44,47], along with an established fiber quantification software approach [48], to explore how collagen fiber properties: alignment per length, width, length, and straightness, relate to malignancies and patient data profiles. Quantitative phase imaging is a method that can measure nanometer scale pathlength changes in a biological specimen [47]. Recent studies show that QPI has clear potential for clinical applications [49-52]. SLIM has previously been used toward the effective diagnosis of breast cancer, which is usually performed through qualitative H&E stained tissue examinations [46]. In addition to its ease of use, efficiency and conduciveness to fiber analysis, the phase images produced by SLIM have also been used to extract various tissue properties, such as scattering length (the average distance between two scattering events) of light scattered by the tissue [53]), optical anisotropy (the average cosine of the scattering angle, found to be reduced in low prostate survival cases [54]), and the spatial fluctuations in refractive index, known as disorder strength [55]. The refractive index of tissue is also accessible in SLIM images, and has previously been used as a marker for prostate malignancies [54]. Furthermore, SLIM uses broadband illumination light that diminishes speckle artifacts and lends itself well to automated segmentation tools that need both sharp morphological contrast and precise quantitative information [56,57].

In this chapter, we used our analysis to segment stromal fibers, including collagen, in both PDAC and NAT cores. In contrast to the previous fiber tracking work on SLIM breast tissue images, which only evaluated fiber orientation[58], here we incorporate four fiber properties and do not require any structural segmentation. Since SLIM is not uniquely sensitive to collagen, an involved process with filters was previously employed to exclude all signals except for the isotropic collagen fibers. Here, however, we leverage the greater number of fiber properties and the drastic morphological dissimilarity in PDAC and NAT cores to dispense with any prior feature

extraction. We found significant differences between the filament properties in the two groups and a strong correlation between these and patient survival.

2.3 Methods

2.3.1 Tissue Microarray (TMA)

The patient cohort consisted of 90 tumor cores and 90 normal adjacent tissue, and one marker core (US Biomax, Inc.,#HPan-Adel180Sure-010). From the PDAC group, 62 cases were ductal adenocarcinoma, 20 cases were adenocarcinoma, 4 were adenosquamous carcinoma, 3 were mucinous adenocarcinoma, and 1 was mucinous cystadenoma. Staging levels were I-II, IA, IB, II, IIA, IIB, and IV. The mean overall survival was 23.7 months (range 0-87 months). Sixty of the patients were males and thirty were females. The mean age of the patients was 58.3 years (range 36-83 years). An example of the brightfield cores can be seen in Figure 2.1.

A board-certified pathologist, who was blinded to clinical grading and all computed data, performed diagnosis on each core using the H&E brightfield images acquired by Aperio ImageScope (Leica Biosystems). The pathologist also indicated the presence of cancer cells and desmoplasia in PDAC histology, as well as healthy acini, veins, ducts, and islets of Langerhans in normal tissue. TMA cores containing necrotic debris or partially missing tissue were all omitted from the final analysis.

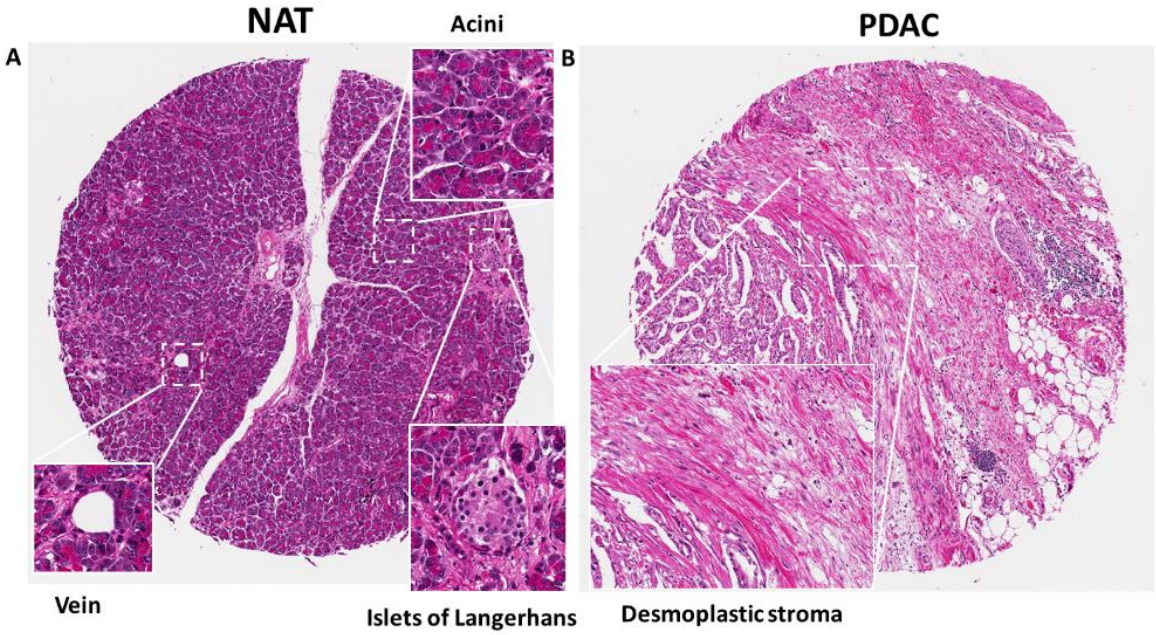

Figure 2.1 Stitched brightfield H&E images of whole pancreas biopsy cores (Hpan-Ade180Sur-01). **(a)** NAT pancreatic core with insets showing zoomed in regions of a duct, acini, a vein, and Islets of Langerhans. **(b)** Corresponding patient PDAC core, with inset showing the characteristic dense desmoplastic stroma.

2.3.2 Spatial Light Interference Microscopy (SLIM)

The cores were imaged with spatial light interference microscopy (SLIM) with a resolution of 380 nm using a Nikon Plan-APO 40x/0.95 N.A objective (Fig. 2.2). SLIM is composed of an inverted phase-contrast microscope with a module attachment at the output (CellVista SLIM Pro, Phi Optics, Inc.). A liquid crystal spatial modulator (SLM) placed at the back focal plane of a Fourier lens (Fig. 2.2) provides additional phase shifts between the scattered and unscattered light, in increments of $\pi/2$. The pattern projected on the SLM matches exactly the phase ring of the objective pupil. Four intensity images with different phase delays are acquired consecutively, enabling the computation of a phase map [44]. SLIM thereby generates quantitative phase images of the sample that, in turn, provides information on its dry mass density at femtogram precision [59]. All cores were acquired through an automated scan of 1388 x 1044-pixel tiles using our integrated

custom SLIM software [60]. The scanning procedure took approximately 20 minutes to prepare and, subsequently, each core was covered within 3.3. minutes at a rate of 1 frame/s. The total imaging dimensions amounted to 24 x 40.2mm^2, and consisted of 24,120 individual SLIM images, which were stitched to form a mosaic using a python algorithm developed in-house (Fig. 2.3(a-d)).

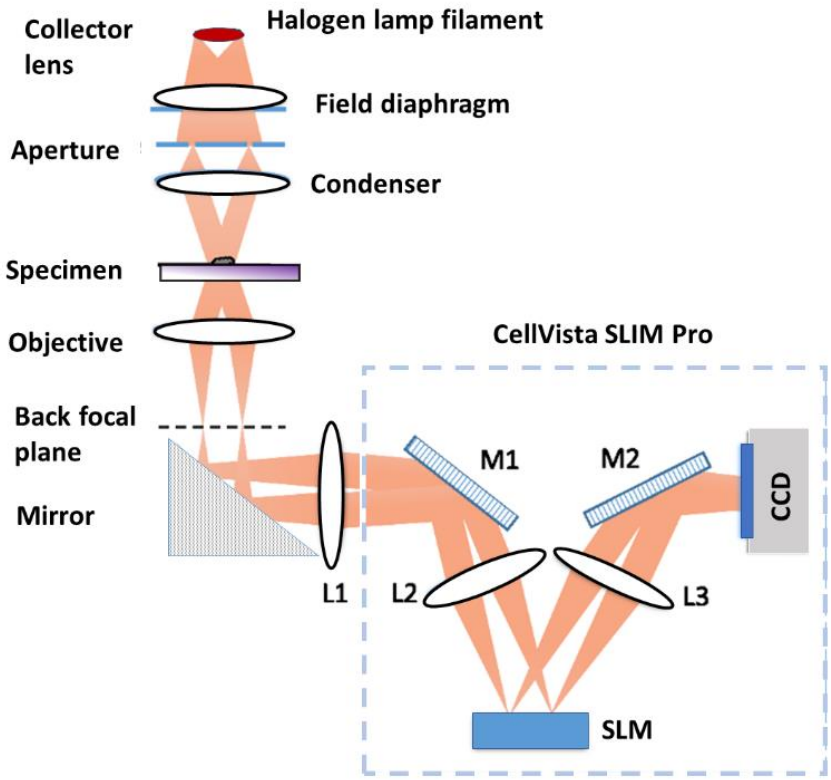

Figure 2.2 Schematic for SLIM. The SLIM module is attached to a commercial phase contrast microscope (Nikon Eclipse T*i*).

2.3.3 Fiber Tracking

Fibrillar structure analysis was performed on SLIM images using the default settings in the CT-FIRE software package, as previously described [37,40,56] (Fig. 2.3(e)). Alignment per length was calculated according to relative fiber angles in a core, spanning a range of 0.0-1.0 (1.0 indicates all fibers are parallel), divided by the length of the traced fiber in microns. Length and width were generated initially in pixels and then converted to microns according to a scale calibrated from the

40X Nikon objective. Straightness of fibers was calculated based on tangent angles at successive points tagged on a segmented line (1.0 denotes all fibers are in the same direction). To account for intra-tumoral PDAC heterogeneity on the TMA, all fibers from the cores, amounting to between 4,000 and 5,000 tracking fragments per core, were included in the analysis. We also incorporated the available patient information (grade, stage, gender, age) as covariates in our analysis to estimate their potential clinical application.

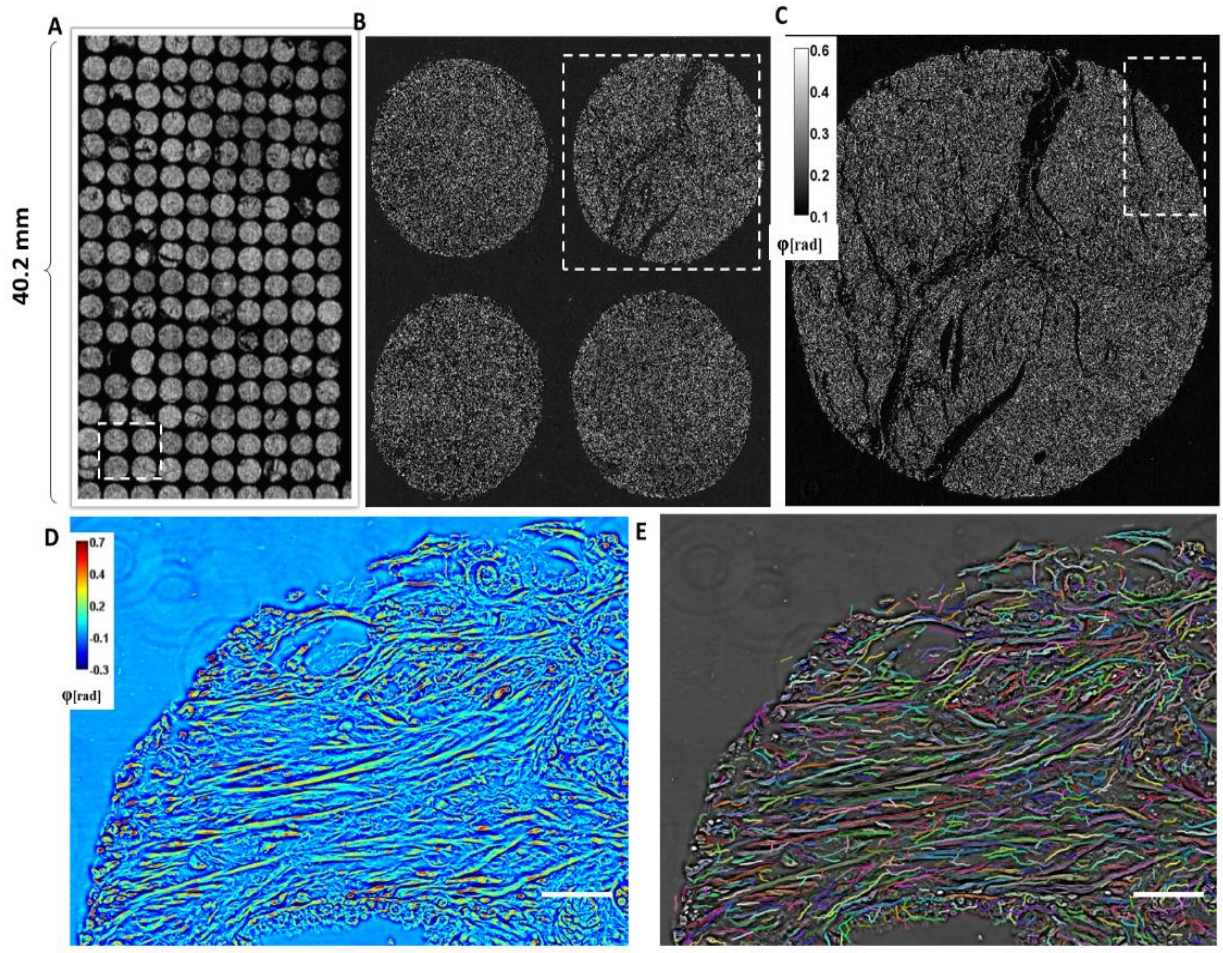

Figure 2.3 (a) Stitched SLIM images of the whole TMA slide (Hpan-Ade180Sur-01). **(b-d)** SLIM images of PDAC/NAT biopsy cores (scale bar 50 μm). **(e)** Corresponding CT-Fire mapping of fibers for D.

2.3.4 Statistical Analysis

Statistical analysis was performed in MATLAB™. The histograms were generated using data retrieved from each fiber. Differences between NAT and PDAC parameters were evaluated using standard deviations for alignment measurements - to account for differences in overall fiber alignment per core - and mean values for the other three properties, with p values obtained from student t-tests. The decision boundary for the principal component analysis (PCA) was obtained using a linear discriminant analysis (LDA) classifier. Survival curves were constructed according to the Kaplan-Meier estimation, with differences calculated according to the Log-rank test. Cutoff values were selected according to the first and last of histogram distributions. The cutoffs for alignment per length were below 0.9°/μm and after 1.15°/μm, for width 0.4μm and 0.5μm, for straightness 0.919 and 0.928, and for length they were 6.0μm and 7.9μm. Similar figures were applied to NAT computations. The correlation percentages were computed according to the Pearson's linear correlation coefficient [61].

2.4 Results

2.4.1 Relationship between PDAC and NAT fiber tracking properties

Since the TMA used in this study includes two cores per patient, we were able to image and quantify filamentary details in normal and PDAC regions from the same patient. Upon visual examination, there were evident discrepancies in morphology between cancerous and NAT cores, with notably dense desmoplasia present in PDAC tissue cores. To explore how filament structures relate to malignant characterization, we applied the fiber tracking algorithm on both PDAC and corresponding NAT cores. Since the SLIM signal from NAT cores is nearly as extensive as that from PDAC cores (Fig. 2.3(b)), there were similar amounts of tracking elements in both core types. The PDAC segments predominantly trace collagen fibers, while those of NAT cores track collagen

in addition to the boundaries of acini, veins, ducts, and islets of Langerhans (Fig. 2.1). Our data show that PDAC cores had fibrillar structures with less alignment per length, narrower width, and greater length and straightness than the corresponding NAT tissue (Fig.2.4). In addition to the four fiber properties being significantly different in PDAC compared to normal tissue, considerable distributions in all four fiber features were calculated in each core.

In order to enhance the distinguishing information between core types, quantitative data provided by SLIM was included, along with the four fiber parameters, and dimensionally reduced using PCA. LDA was thereafter performed to distinguish PDAC from NAT cores (Fig. 2.5(a)). In this case, the mean dry mass density was evaluated for each core according to previously detailed methods using SLIM [59]. A confusion matrix yielded an accuracy of 0.7. Using individual parameters may be more effective however, as ROC curves constructed for each fibrous property (Fig. 2.5(b)) show that straightness and length have the greatest diagnostic value, with AUCs of 0.83 and 0.82, respectively. There was no significant difference in the four calculated fiber properties between PDAC cores of low and high histological grade. Furthermore, there were no significant correlations found between the other patient characteristics and fiber properties.

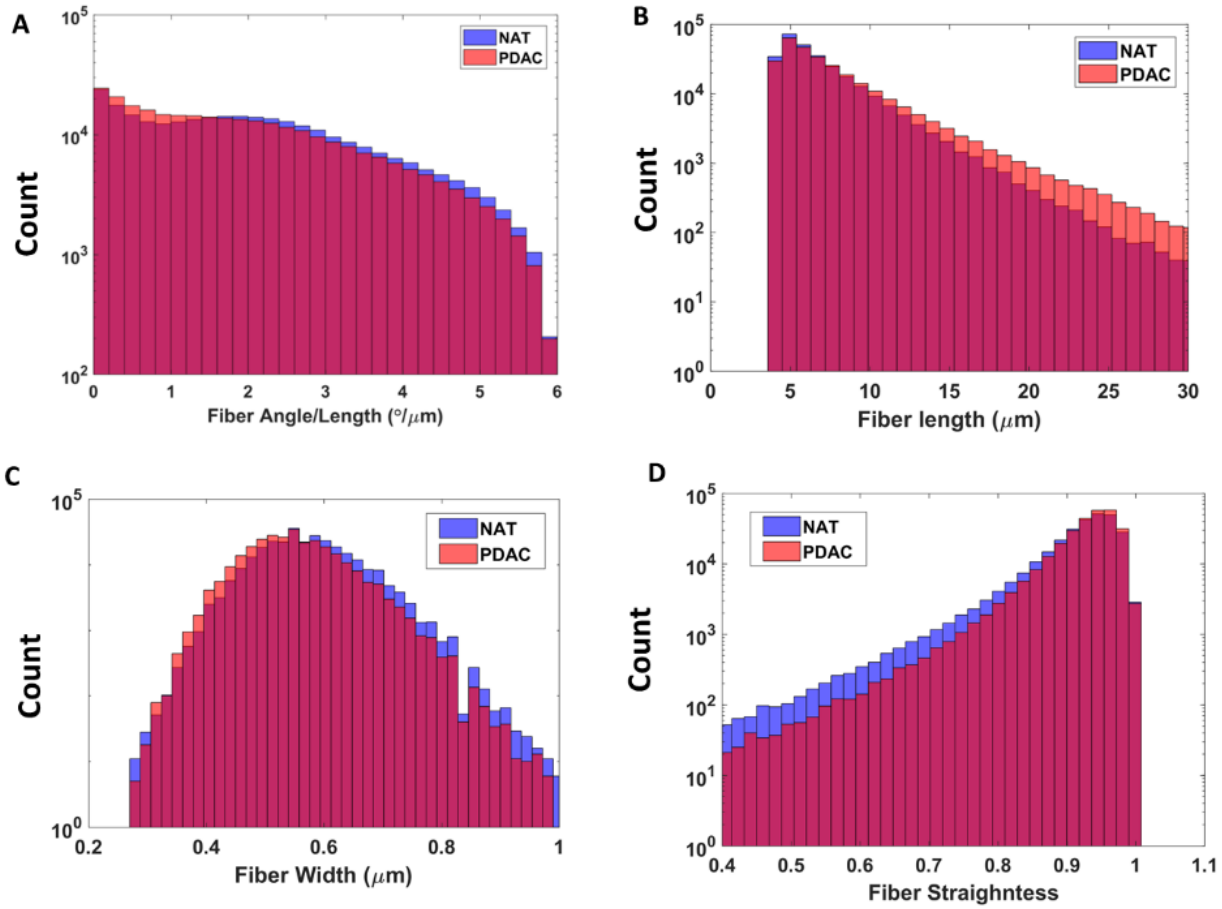

Figure 2.4 Histograms (log) of both normal adjacent tissue (NAT) and pancreatic ductal adenocarcinoma (PDAC) **(a)** fiber angle/length, **(b)** fiber width, **(c)** fiber length, and **(d)** fiber straightness of individual fibers across all cores.

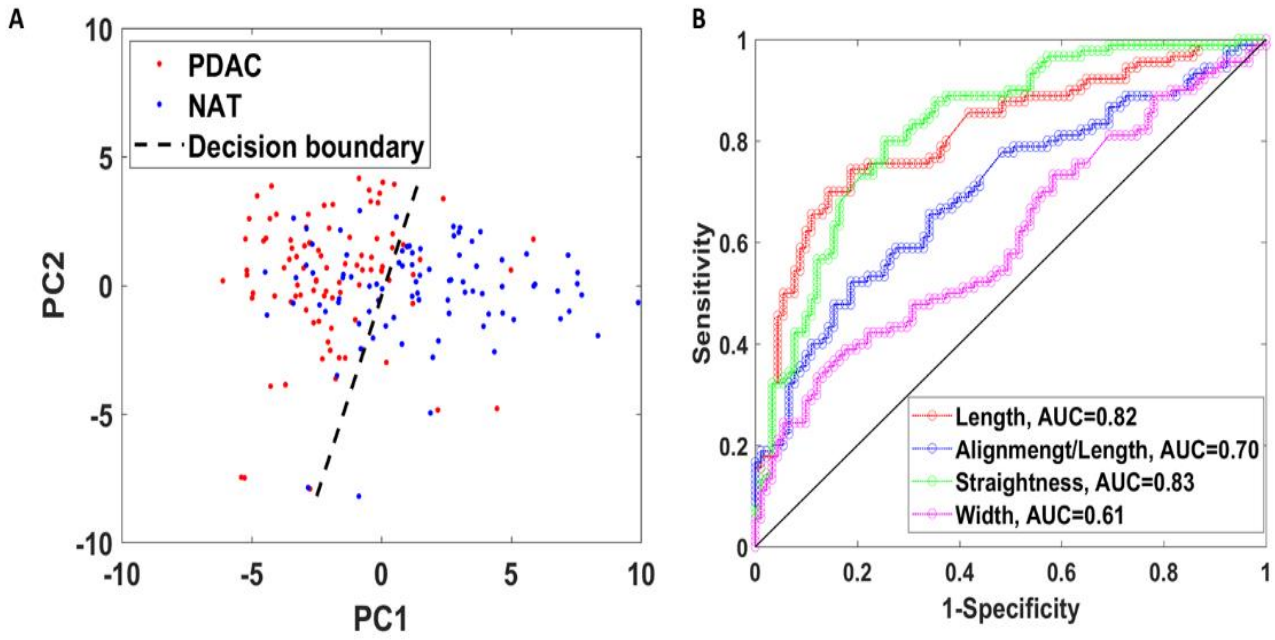

Figure 2.5 (a) Plot of first two principal components of mean width, straightness, length, alignment/length fiber parameters, as well as dry mass density for PDAC and NAT cores, with decision boundary. **(b)** ROC curves for discriminating cancerous tissue based on mean fiber length, alignment/length, straightness, and width.

2.4.2 Stromal fibers as marker for patient outcome

PDAC patients with high alignment per length of segmented fibers exhibit significantly reduced survival rates (Fig. 2.6(a)). Fiber width and length were greater in low survival cases, having associated survival periods of approximately 40 and 60 months, respectively, compared to 80 months for cases with narrower and shorter fiber profiles (Fig. 2.6(b) and 2.6(c)). Our results indicate that straightness has less predictive value in survival rates (Fig. 2.6(d)). The width and length distributions had the greatest standard errors, indicating largest intra-class variability. Surprisingly, the typical disease predictors in tissue, such as tumor stage and grade, were not significant in this patient cohort (Fig. 2.7). This result is likely due to most of our cases being low stage, mostly IB and IIB.

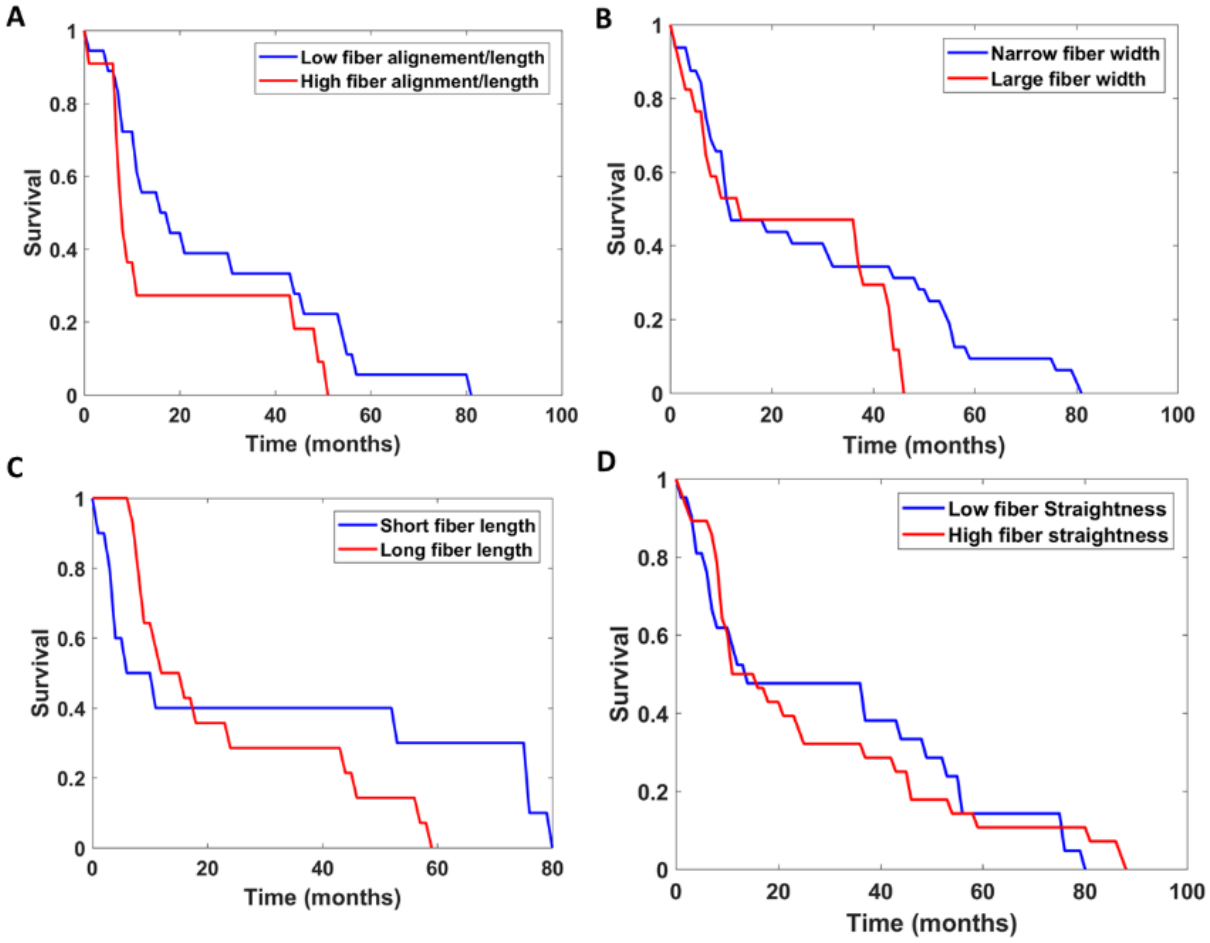

Figure 2.6 Kaplan-Meier survival curves for pancreatic ductal adenocarcinoma (PDAC), comparing different grades of **(a)** fiber alignment/length, **(b)** fiber width, **(c)** fiber length, and **(d)** fiber straightness. Log-Rank χ^2 of 50.7 (str), 37.43 (width), 25.7 (al), 50.8 (length).

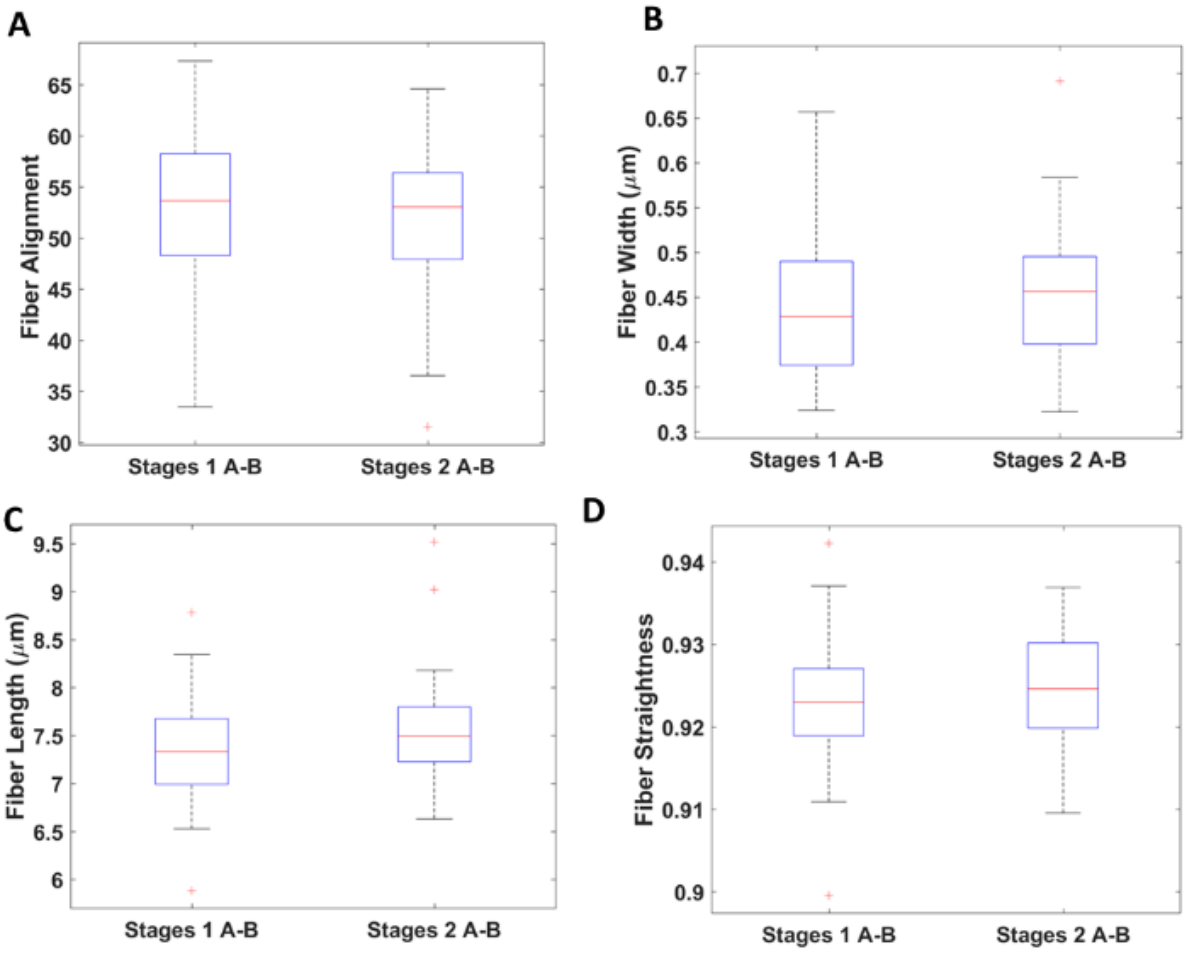

Figure 2.7 Difference between stage groups 1 A-B and 2 A-B in pancreatic ductal adenocarcinoma (PDAC) **(a)** fiber alignment, **(b)** fiber width, **(c)** fiber length, and **(d)** fiber straightness. p-values are 0.36, 0.98 ,0.184, 0.31, respectively.

2.4.3 Correlation of NAT fiber characteristics with patient data

The NAT tissue of PDAC survival rates did not differ significantly in terms of filament alignment per length, width, length, and straightness (Fig. 2.8). In the multivariate assessments of NAT cores, comprising stage, grade, age, gender data, no significant differences in the patient

cohort were found, which may indicate that NAT cores are not informative of neighboring cancerous tissue.

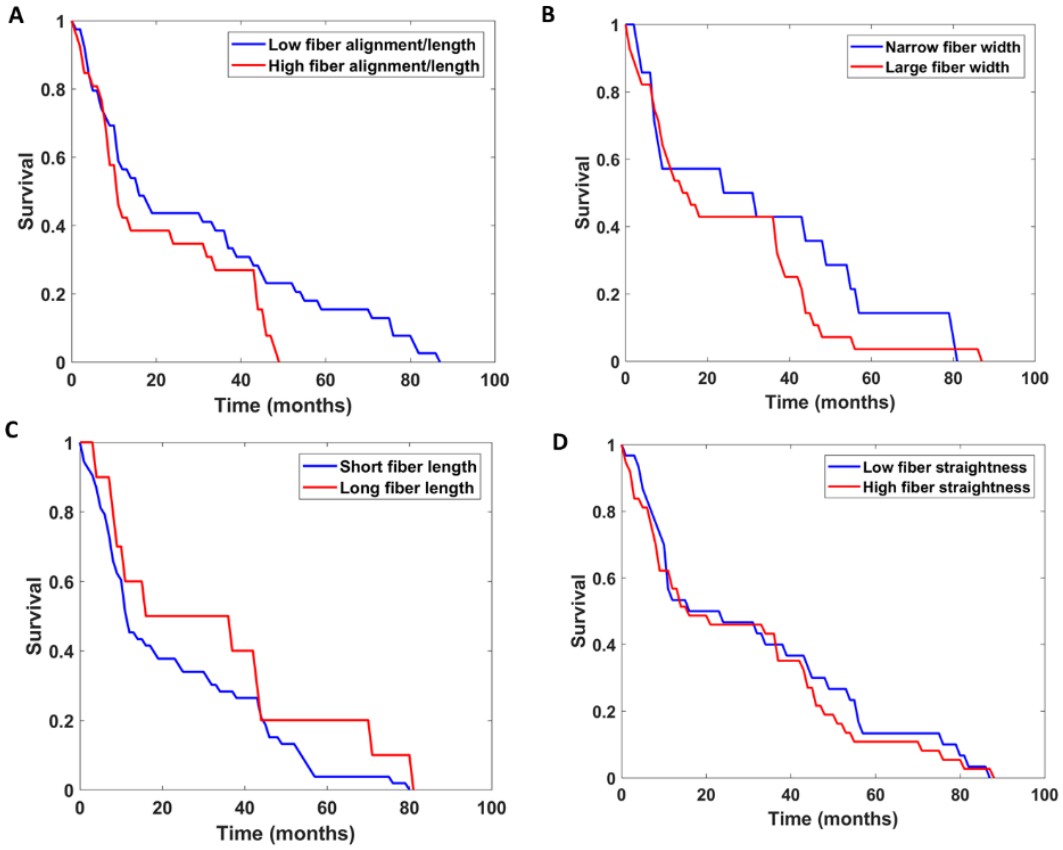

Figure 2.8 Kaplan-Meier survival curves for normal adjacent tissue (NAT), comparing different grades of **(a)** fiber alignment, **(b)** fiber width, **(c)** fiber length, and **(d)** fiber straightness. Log-Rank χ^2 of 38.61 (str), 37.43 (width), 21.9 (al), 44.15 (length).

2.5 Summary and Conclusion

The implementation of efficient and sensitive techniques to detect new PDAC markers is vital for effective treatment of this lethal condition. SLIM generates quantitative phase images that inform on useful tissue properties and has high-throughput tissue scanning capability. Using a

SLIM-based automated procedure, we show that PDAC cores differ sharply from NAT in terms of segmented properties, including alignment per length, width, length and straightness, enabling rapid and automated diagnostic stratifying potential.

This modality holds promise for clinical application without the need for prior structural processing. SLIM has the advantage over collagen-specific modalities, such as SGHM and LC-PolScope, of providing more inclusionary quantitative information of the cellular microenvironment such as cells and matrix that can be used to detect new prognostic markers. Furthermore, though SLIM is not uniquely sensitive to collagen signals, it holds great promise for diagnostic evaluations on label-free samples such as in surgical pathology application, since there is significant discrepancy in morphology between PDAC and NAT cores, which is fully described in the phase maps. Furthermore, it was found that both larger width and greater length of PDAC collagen fibers are associated with poor patient prognosis. To further explore the value in extracted fiber data, we evaluated the clinical relevance of the variables in patient profiles. The fiber data from NAT cores were evaluated with the same approach. No substantial heterogeneity was observed among patients for NAT, either in survival rates, or stage, grade, gender and age.

These findings establish novel insights on the ECM based morphological aspects of PDAC tissue and its relationship with those of normal adjoining regions. This is an especially important revelation since pancreatic cancer is commonly associated with bleak post-operative prospects.

In summary, we have demonstrated that combining quantitative phase imaging with a fiber tracking algorithm can assist in diagnostic and prognostic evaluations, which may prove beneficial in the clinical setting. Before our method becomes adoptable, further investigations on different tissue samples are needed to consolidate and fine-tune this process. Since SLIM provides a

quantitative map of tissue, it lends itself well to the application of machine learning tools to bypass and expedite tedious and expensive histological procedures, as well as refine tissue analysis.

CHAPTER 3: Quantifying Myelin Content in Brain Tissue using Color Spatial Light Interference Microscopy (cSLIM)

3.1 Abstract

Deficient myelination of the brain is associated with neurodevelopmental delays, particularly in high-risk infants, such as those born small in relation to their gestational age (SGA). New methods are needed to further study this condition. Here, we employ Color Spatial Light Interference Microscopy (cSLIM), which uses a brightfield objective and RGB camera to generate pathlength-maps with nanoscale sensitivity in conjunction with a regular brightfield image. Using tissue sections stained with Luxol Fast Blue, the myelin structures were segmented from a brightfield image. Using a binary mask, those portions were quantitatively analyzed in the corresponding phase maps. We first used the CLARITY method to remove tissue lipids and validate the sensitivity of cSLIM to lipid content. We then applied cSLIM to brain histology slices. These specimens are from a previous MRI study, which demonstrated that appropriate for gestational age (AGA) piglets have increased internal capsule myelination (ICM) compared to small for gestational age (SGA) piglets and that a hydrolyzed fat diet improved ICM in both. The identity of samples was blinded until after statistical analyses.

3.2 Introduction

Myelin is a critical component of the nervous system white matter. The myelin sheath surrounds axons and thereby provides the necessary insulation for the efficient transmission of neural electrical signals across brain regions[62]. Myelination of fiber bundles is one of the slowest processes of brain maturation in humans, starting at 16 weeks gestational age and increasing rapidly from 24 weeks through to the perinatal period and continuing until puberty[63]. The rapid

growth phase during the perinatal period represents a vulnerable time for neural development and is a critical period for small for gestational age (SGA) infants. Myelin formation plays a crucial role in the operation of diverse cognitive faculties during the perinatal period[64-68] and continuing throughout adulthood[69].

Particularly impacted by deficient myelination are intrauterine growth-restricted (IUGR) and low birth weight (LBW) infants. These infants are at higher risk of morbidity and mortality early in life[70] and display adverse neurological outcomes that include developmental disorders, learning and attention difficulties, behavioral issues, neuropsychiatric disorders and epilepsy that persist into adulthood[71-77]. Approximately 24% of newborn human infants are IUGR, and more than 20 million infants are born each year with LBW[78,79]. Currently, there are no available therapeutic interventions to prevent or treat brain damage in the IUGR newborn. Early dietary interventions aimed at mitigating the cognitive deficits associated with IUGR and LBW are important given that rapid growth occurs early in postnatal life.

Multiple modalities have been used to assess myelin deposition in biological samples. Luxol Fast Blue (LFB) is a dye that stains myelin in formalin fixed tissue[80]. LFB provides information on the presence of myelin in terms of its spatial distribution but does not allow quantification. Magnetic resonance imaging (MRI) at high field strength allows in vivo visualizations of human brain structures[81] and has simplified the analysis of myelin concentrations[82]. However, MRI detection is indirect, relying on the proton spins of water molecules. Although a reasonable agreement between MRI and LFB staining has been shown, MRI remains a low sensitivity method for myelin imaging[83].

Other efforts to quantify myelin in brain tissue have included the use of the proton-induced X-ray emission (PIXE), which generates X-rays with an energy spectrum that is characteristic of

a chemical component[82]. This enables a quantitative determination of the spatial distribution of components within a sample. However, its resolution is relatively poor and it involves tedious calculations and cumbersome equipment[81].

Here, we use the technique called color spatial light interference microscopy (cSLIM)[58] as a quantitative phase imaging (QPI) technique[47,49,52-55,84-88] to quantify myelin in brain tissue. As discussed in Chapter 2, QPI is a technique that can evaluate nanometer scale pathlength changes in biological specimens. The data in the phase image, $\varphi(x, y)$, is a numerical assessment of the nanoarchitecture of the tissue biopsy. This evaluation is direct, enabling the computation of the sample's dry mass density from phase information [89], and has a resolution that is three orders of magnitude higher than that of MRI [81].

Traditional interferometric methods use coherent light sources, which obstruct the contrast in images with speckle artifacts[90,91]. cSLIM overcomes this issue by exploiting a white light illumination, which averages the speckles and, overall, boosts the phase sensitivity[44,92-94]. The SLIM principle of operation relies on phase shifting interferometry applied to a phase contrast geometry. Thus, we shift the phase delay between the incident and scattered field in increments of $\pi/2$ and acquire 4 respective intensity images, which is sufficient to extract the phase image unambiguously. Because cSLIM uses a brightfield objective and RGB camera, one of the 4 intensities is the standard LFB color image. Thus, simultaneously, cSLIM yields both a brightfield image and a phase map, as illustrated in Figure 3.1. The contrast in the cSLIM (phase) images are produced by the tissue refractive index spatial inhomogeneity, which is an intrinsic morphological marker with relevance to key disease features[46,95]. Unlike previous QPI methods applied for diagnosis, cSLIM is employed on already stained tissue slides, can scan an entire biopsy slide quickly, and generate the brightfield image and corresponding phase map. Furthermore, the effects

of the stain on the phase image are normalized, using a procedure reported earlier[58]. One important application of cSLIM is to use the stain map from the brightfield image to create a binary mask, which is then applied to the phase image. This way, the intrinsic tissue architecture and density are analyzed on specific regions of interest, as revealed by the stain, yet, free of stain artifacts.

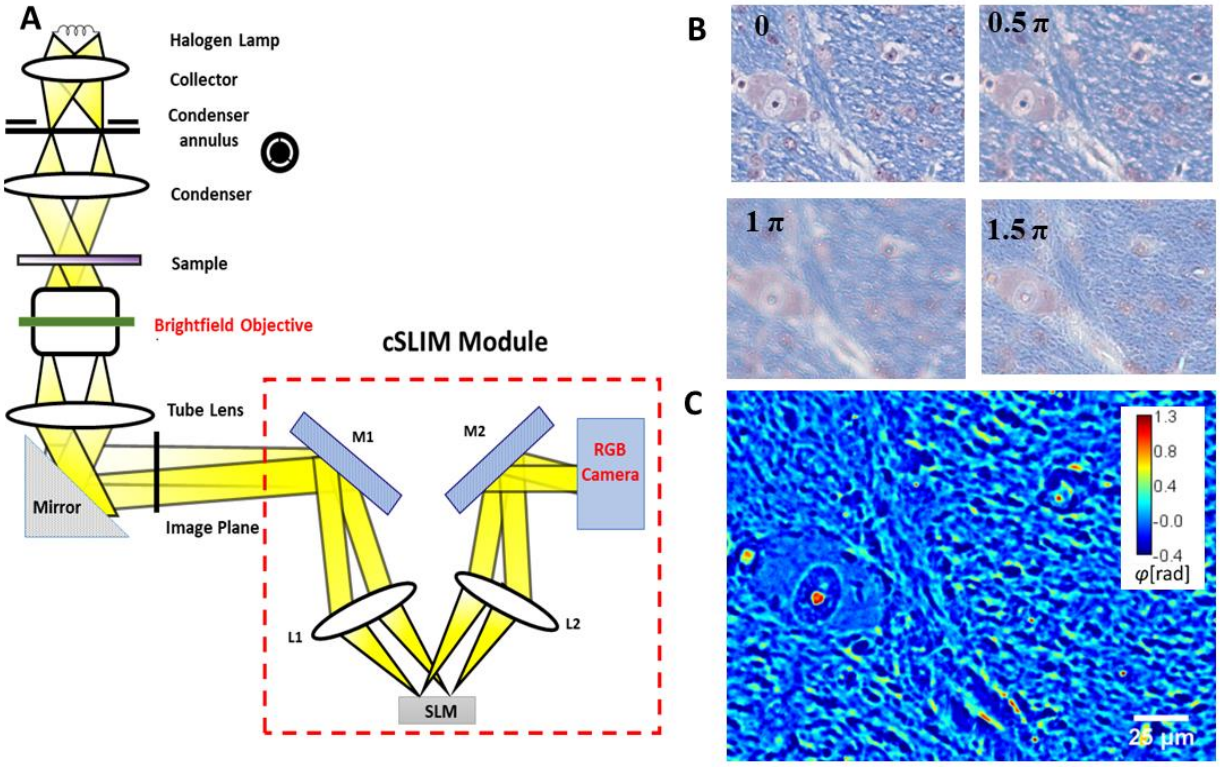

Figure 3.1 Schematic setup for cSLIM. **(a)** The cSLIM module is attached to a phase contrast microscope and uses a brightfield objective with an RGB camera. **(b)** The four phase-shifted color interferograms, with the initial unshifted frame corresponding to a brightfield image. **(c)** Computed SLIM image.

In an effort to first probe our technique's sensitivity, we employed the CLARITY method[96] on mouse brain tissue. Clarity removes the lipid component of myelin and renders the brain tissue transparent. The resultant cleared brain-hydrogel hybrid is physically stable and maintains the

internal structure of proteins and nucleic acids isotropically. Comparing measurements before and after applying the clarity procedure allowed myelin lipids to be assessed specifically in terms of absolute dry mass values[96].

Next, we applied our cSLIM approach to analyze myelin content in piglet brain tissue. Piglets are useful to study neurodevelopmental disorders, because like humans, they are gyrencephalic and they share common brain growth patterns. In order to validate our method, we used two variables: gestational age and diet. Previously, a proprietary blend of dietary hydrolyzed fats (HF) increased relative volumes of 7 brain regions and white matter volume measured by MRI in both SGA and AGA piglets compared to a control fat blend. We analyzed brain sections from these piglets using cSLIM while blind to the treatments. The results show that our method recapitulated the impact of both HF and gestational age on the HF myelin content in the internal capsule.

3.3 Methods

3.3.1 Animals and Diets

Tissues were obtained from piglets used in a previous study[97]. Piglets were PIC Camborough (dam) x PIC 359 (sire), full term, naturally delivered, sex-matched littermate pairs (n = 18 AGA, n = 18 SGA) obtained from the University of Illinois Swine Farm at 2 days old to allow colostrum consumption. Piglets underwent minimal routine processing on the farm (e.g., males were not castrated), but received iron dextran (Henry Schein Animal Health, Dublin, OH, USA) and antibiotic injection (Gentamicin Piglet Injection, Agri Laboratories, Ltd., St. Joseph, MO, USA) per routine farm practice and according to label. SGA was defined as piglets weighing 0.5-0.9 kg at birth, and AGA was defined as piglets weighing 1.2-1.8 kg at birth. Piglets were

placed individually into a caging system under standard conditions as described in a previous publication[98] and randomly assigned to HF or CON diet treatment groups in a 2 x 2 factorial arrangement of size (AGA or SGA) and diet (CON or HF). All animal care and experimental procedures were in accordance with the National Research Council Guide for the Care and Use of Laboratory Animals and approved by the University of Illinois at Urbana-Champaign Institutional Animal Care and Use Committee.

Diets were formulated to meet the nutritional needs of neonatal piglets[99] and were supplied in a premixed, ready to feed format by Abbott Nutrition (Columbus, OH, USA). CON formula contained 100% triglyceride rich oil as a fat source. HF formula contained a proprietary blend of soy free fatty acids, monoacuglycerol palmitate, and phospholipids. In HF diet, 50% triglyceride oil was replaced with HF blend. Piglets were weighed each morning and provided the liquid diet (300 mL formula/kg body weight/d) in 5 equal bolus feedings given at 09:00, 13:00, 16:00, 19:00, and 22:00. Supplemental water as not provided aside from that in the diet. At 26-29 days of age, piglets were anesthetized (telazol:ketamine:xylazine cocktail (100/50/50 mg/kg; 0.022 mL/kg body weight i.m.)) and then euthanized by intracardiac injection of sodium pentobarbital (Fatal Plus; 72 mg/kg body weight). Brains were quickly extracted, and the left hemisphere placed in 10% neutral buffered formalin (NBF; Leica Biosystems, Wetzlar, Germany) for fixation, refreshing the formalin solution after 24 hours to ensure adequate fixation.

3.3.2 Piglet Tissue Samples

The brains were cut in coronal sections 5 mm thick per block beginning 0.5 mm rostral to the optic chiasm. Blocks were soaked in 10% NBF overnight before processing. Fixed tissue blocks were then cut into 4 µm thick sections, mounted on glass slices and subsequently stained with LFB by the Veterinary Diagnostic Laboratory (University of Illinois Urbana-Champaign,

Urbana, IL, USA) according to standard protocols for formalin-fixed, paraffin embedded brain and spinal cord tissue sections. Following LFB staining, slides were selected for imaging. Hyper-stained slides, where the blue signal was obstructed, were omitted from imaging analysis as intense cresyl violet background staining may have interfered with cSLIM measurement. Final analysis included 10 AGA slides (5 HF fed and 4 CON fed), and 9 SGA (5 HF and 4 CON) slides. For all the imaging and analysis, we were blind to the sample diet categories. The internal capsule regions were selected for analysis because the area is myelin-rich myelin, as indicated by the dense dye regions (dark blue, in Figure 3.2 a).

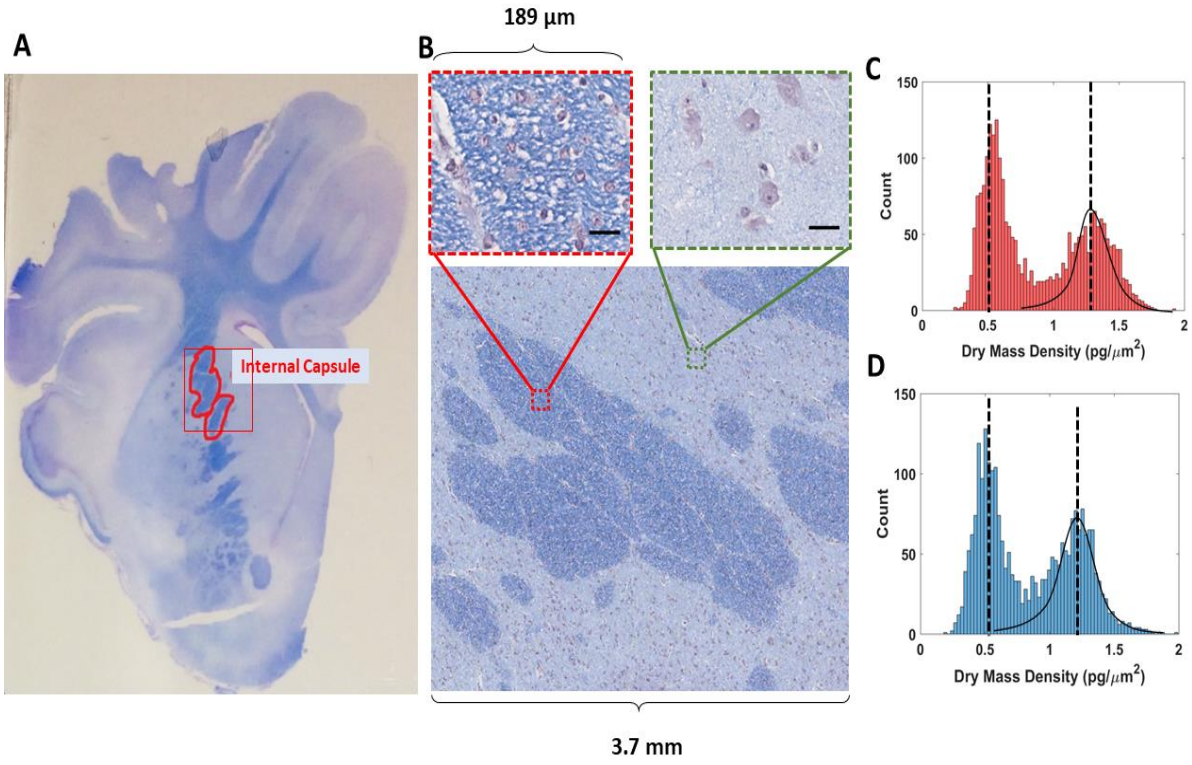

Figure 3.2 High and low myelin. **(a)** Picture of a slide of a piglet brain tissue with the internal capsule delineated in red. **(b)** A stitch of brightfield cSLIM images with selected single frames of high and low myelin regions (scale bars: 35 µm). **(c)** Histograms of the dry mass density values per quarter frame in one AGA tissue sample. **(d)** Histogram of the dry mass density values per quarter frame in one SGA tissue sample. Gaussian fitting is used to separate the high and low myelin regions.

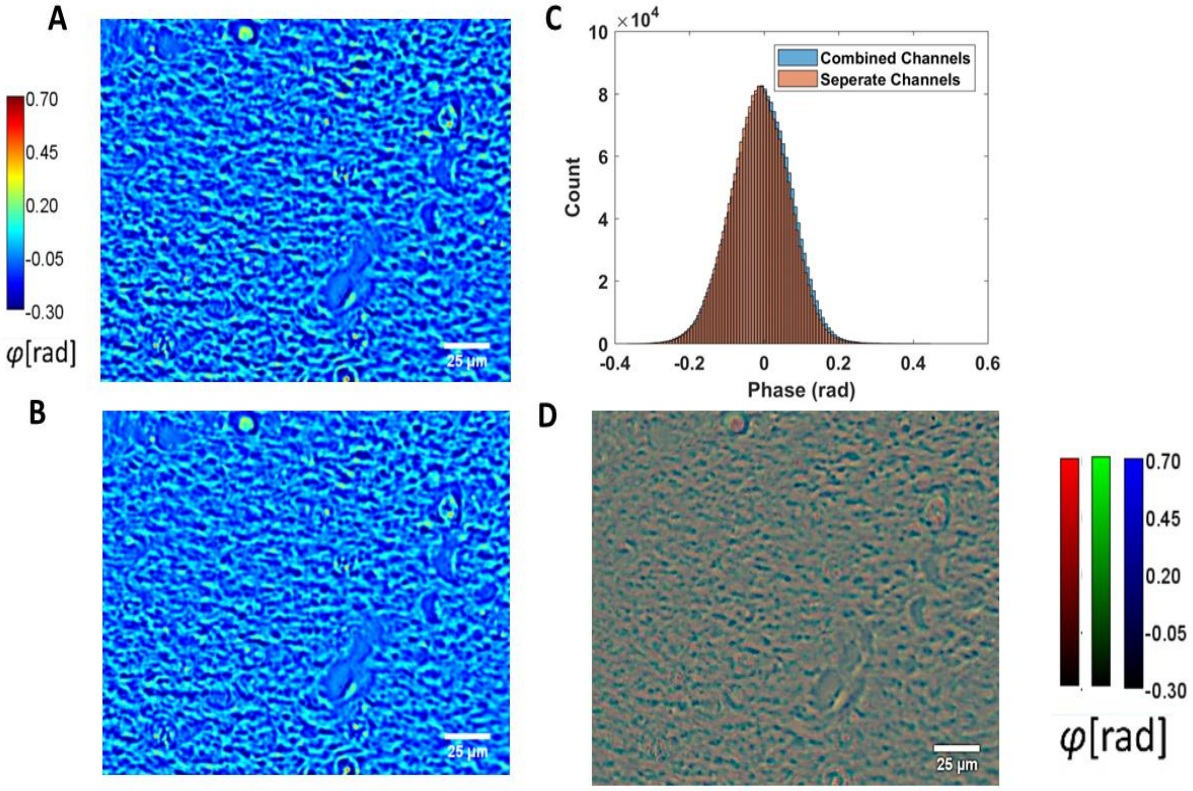

Figure 3.3 Color SLM calibrations**. (a)** Original SLIM image. **(b)** SLIM image obtained from different red, green, and blue SLM calibrations. **(c)** histograms of **(a)** and **(b)**. **(d)** 'RGB SLIM' images composed of red, green, and blue SLIM images respectively.

3.3.3 cSLIM

The cSLIM system was implemented using a commercial SLIM module (Cell Vista SLIM Pro, Phi Optics, Inc) attached to a commercial phase contrast microscope (Axio Observer Z1, Zeiss). The system was outfitted with a Zeiss EC Plan-Neofluar 40x/0.45NA objective and a Point Grey color camera. cSLIM is fully automated and operates as a whole slide scanner that provides simultaneously a standard brightfield image (e.g., of H&E, immunochemical stains, etc.) and a quantitative phase map[58].

The annular condenser ring is still employed and allows shifting of the unscattered light at the spatial light modulator (SLM) of the add-on module (Fig 3.1). For every phase shift, three intensity frames are acquired for each channel of the camera:

$$I(x, y; \varphi) = rR(x, r; \varphi) + gG(x, y; \varphi) + bB(x, y; \varphi), \quad (1)$$

where the weighing coefficients r, g, b are related such that $r + g + b = 1.$ For our measurements, we used $r = 0.1,\ g = 0.6,\ b = 03$, to generate a grayscale image, the ratios having been determined empirically by finding the equivalent central wavelength, λ, at which the phase modulation of the SLM occurs. The phase map is then computed from the four frames as previously described with SLIM[44]. The measurement with an RGB camera resembles interferometry with 3 different sources [58]. Combining the three channels makes the problem similar to the grayscale camera case, except the temporal autocorrelation function and coherence length are slightly different (see Supplementary Information in [58]). Since we calibrate the SLM with the three channels combined, the phase shifts are automatically corrected for dispersion effects. To demonstrate this, here we calibrated the SLM according to each channel separately and captured images of the same field of view for each color, with their respective calibration. We then compared the resulting SLIM image from one calibration (Fig 3.3a) with the one from the three calibrations (Fig 3.3b). The histograms of both images show an almost complete overlap (Fig 3.3 c). If we create an RGB composite of three SLIM images corresponding to each channel, we would obtain an image as shown in Fig 3.3d.

The effects of the stain on the phase map are accounted for in the normalization technique. Previous analysis showed that changes induced in the images by dispersion were weak and that the final phase map, after our applied normalization, remains equivalent to the original SLIM.

3.3.4 Dry Mass Measurement

The dry mass density ρ of the tissue section is computed from cSLIM phase images using the following relationship:

$$\rho(x, y) = \frac{\lambda}{2\pi\eta}\varphi(x, y), \qquad (2)$$

Where λ is the center wavelength of the optical source, $\eta = 0.2\,ml/g$, corresponding to an average of reported values, and $\varphi(x, y)$ is the phase value of the tissue at different points. The resulting dry mass density has units of mass/area. Once the phase map of myelin alone was generated, the total dry mass density was calculated by integrating ρ over all selected quarter frames.

3.3.5 Image Processing

We imaged the entire internal capsule from each slide. The data from each slide consisted of 625 cSLIM images, each the result of 12 intensity measurements (four phase shifted color images). The resolution is dictated by the diffraction limit. Our images are oversampled at 7.2 pixels per micron. To confirm that the entirety of the internal capsule was captured, a mosaic was constructed for each slide (Figs 3.2a-b). The regions adjacent to and surrounding the internal capsule were segmented out, because they contain primarily cell body content as indicated by the reduced LFB stain, prior to myelin content cSLIM quantification.

In order to separate the high and low myelinated regions, a histogram of dry mass for each quarter frame was evaluated, generating a bimodal pattern, which we described using gaussian fits, thereby selecting out the high myelin quarter frames from the rest of the sample (Fig 3.2b). After determining each quarter frame corresponding to the internal capsule, we applied a segmentation scheme to remove all the components of the tissue that do not correspond to myelin. The brightfield

image for each frame was first used to generate a binary mask specific to myelin through a color threshold and a filtering function (Figs 3.4 a-b). The SLIM counterpart image was then multiplied by the mask to produce a phase map specific to myelin (Figs 4 c-d). As a result, this procedure renders the phase signal specific to the blue areas in the color image. Thus, the staining is simply used to locate the myelin structures. The intensity values of the stain are only involved in determining a binary threshold, while the phase map is used to directly measure the dry mass density of the myelin. All measurements were made while blind to slide-diet pairings.

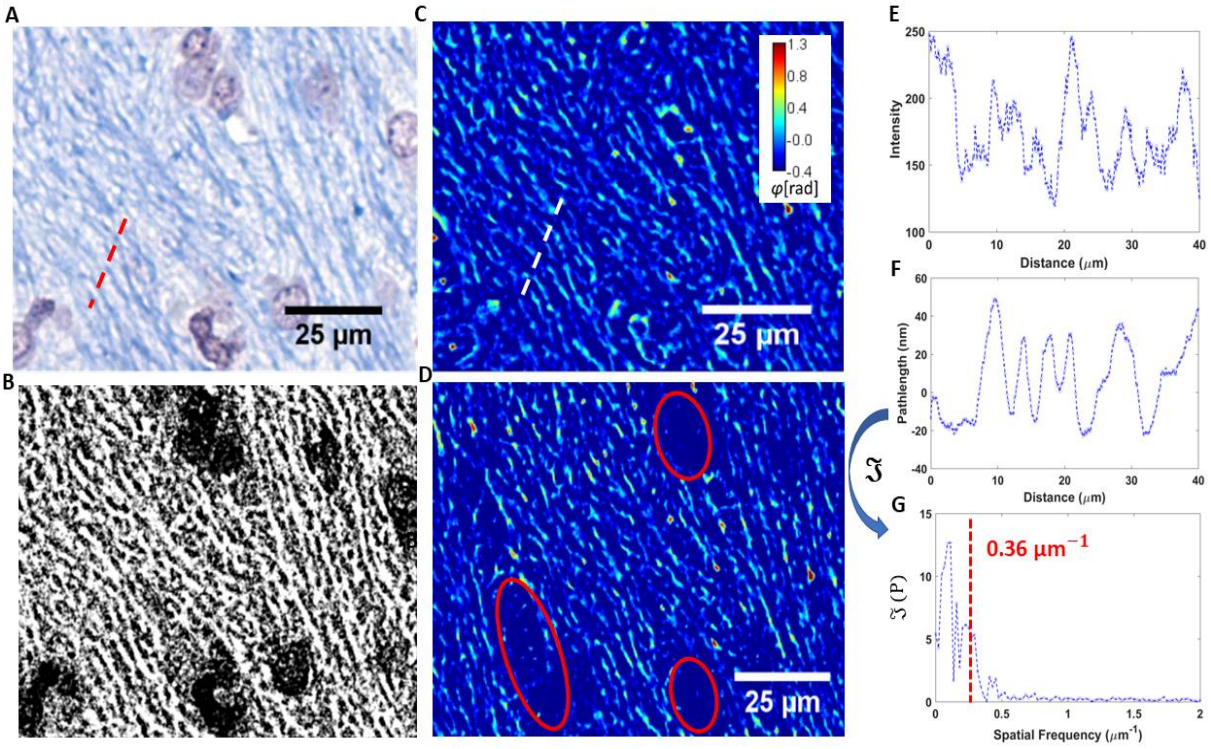

Figure 3.4 Myelin segmentation process. **(a)** A brightfield image is first used to create a **(b)** binary mask specific to myelin, which is then multiplied by the **(c)** corresponding SLIM image. **(d)** The result is a phase map uniquely describing the myelin content of the image, with former cellular areas (encircled in red) deleted. **(e)** Plot of the cross section in **(a)**. **(f)** Plot of the cross section in **(c)** and **(g)** its Fourier transform, which has a mean frequency of $0.36\ \mu m^{-1}$, corresponding to an average axonal width of $2.7\mu m$.

3.3.6 Myelin Sheath Diameter

Cross sections over myelinated axons were traced in both brightfield and corresponding SLIM images (Figs 3.4 a,c). The resulting spectra of intensity and pathlength are shown in Figs 3. 4 e-f. Taking the Fourier transform and computing the mean amplitude-weighted spatial frequency yields a value of $0.36\ \mu m^{-1}$, translating to $2.7 \mu m$ as the average external diameter of the myelin sheaths, which agrees well with previous findings[100].

3.3.7 CLARITY

Clearing brain tissue with the CLARITY method removes its lipids and therefore reduces drastically the myelin content. CLARITY was applied on coronal mouse brain (the piglet samples were permanently coverslipped) sections using 8% sodium dodecyl sulfate (SDS) according to a standard protocol[101]. Scans of 53 by 95 frames were captured and computationally stitched to form a mosaic image (Figs 3.5 a-b). The anterior commissure and the corpus callosum were targeted for analysis (Figs 3.5 a-b) because these regions are comprised primarily of myelinated axon tracts.

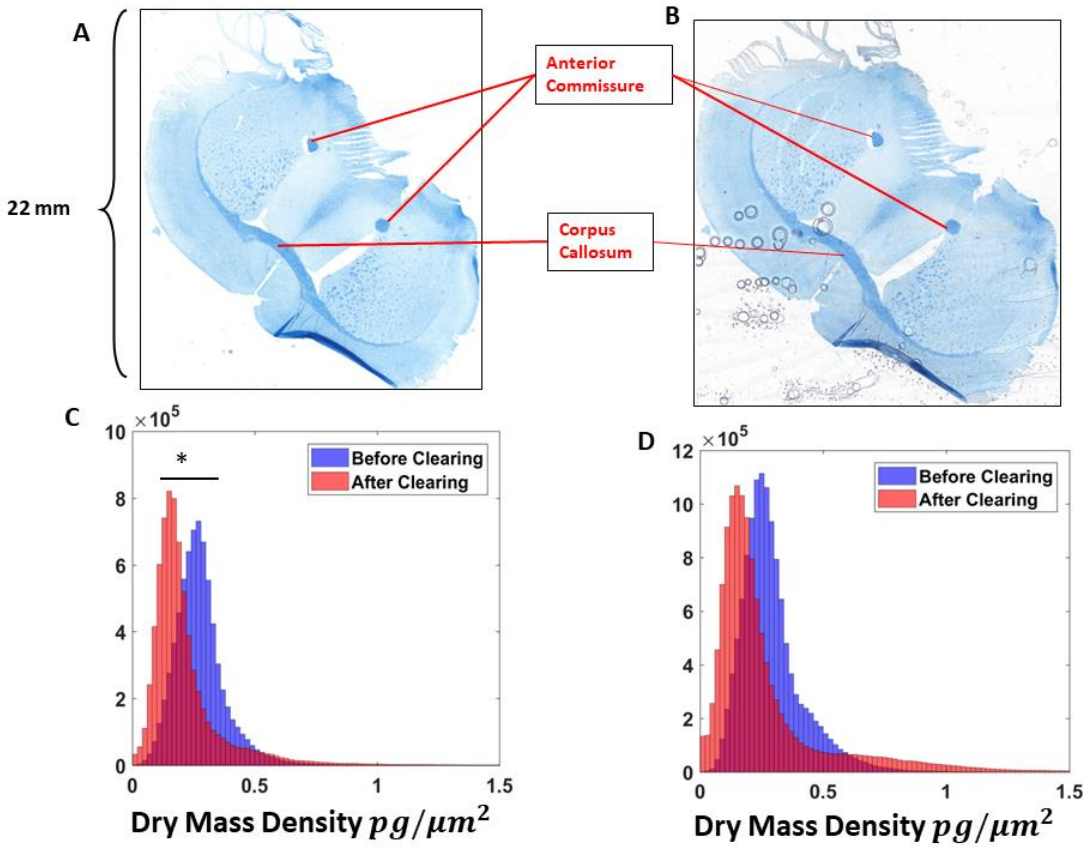

Figure 3.5 CLARITY results. 53 x 93 frame stitches of a mouse brain tissue **(a)** before and **(b)** after the clearing procedure. Dry mass density histograms of **(c)** the anterior commissure portions and **(d)** the corpus callosum structure. (* $p<0.05$).

3.4 Results

3.4.1 Control Experiment

To test the ability of cSLIM to assess the dry mass content of myelin, we cleared mouse brain sections stained with LFB and imaged the specimens before and after clearing. The samples were scanned by cSLIM in 53 by 93 frames and the same segmentation scheme was used to process the images. Fig 3.5 shows a composite image of a coronal mouse brain section, stained with LFB, before and after the clearing process. The anterior commissure and corpus collosum, indicated in Figs 3.5 a-b, were chosen for comparative analysis. Contrasting the tissue before and after

CLARITY revealed reductions in dry mass density measurements in both the anterior commissure, from an average value of $0.4\ pg/\mu m^2$ to $0.2\ pg/\mu m^2$, and the corpus callosum, from an average value of $0.4\ pg/\mu m^2$ to $0.3\ pg/\mu m^2$, which was significant in the case of the anterior commissure, but not in the case of the corpus callosum (Figs3.5 c-d). The clearing of the corpus callosum, which is a much larger structure, may have been less extensive than that of the smaller anterior commissure. Since the Luxol Fast Blue stain attaches to the protein content of the myelin, and its hue is still present after clearing (Fig 3.5 d), it is clear that part or all of the lipid content was removed. This confirms that the cSLIM is sensitive to the dry mass of myelin lipids.

3.4.2 Diet Composition and Myelin Dry Mass Density

We evaluated samples from 4 treatment groups: AGA and SGA piglets on HF or CON diet. The regions analyzed were the internal capsule, which represented a myelin-rich and the corresponding surrounding parenchyma, which represented a low myelin brain region. Juxtaposing the brightfield images of SGA samples with those of AGA revealed that the four sets of samples differed in the depth of color and density of cells. The internal capsule contained darker, more fibrous structures, whereas the low myelin areas contained more numerous, larger cell bodies (Figure 3.6).

Significant differences were found between control and HF diet samples in all four tissue classifications, as shown in Figure 3.7. Myelin dry mass density in the internal capsule was markedly higher in AGA compared to SGA piglets, (p <0.01). Similarly, higher myelin dry mass content was found in the surrounding parenchyma in AGA compared to SGA piglets (p<0.05). The mean values for dry mass surface density in the internal capsule was approximately $1\ pg/\mu m^2$ for the control AGA piglets, and approximately $0.8\ pg/\mu m^2$ for the control SGA piglets (Figs 3.7a-

b). Markedly lower average dry mass densities were found in the surrounding parenchyma for both AGA and SGA piglets ($\sim 0.5\ pg/\mu m^2$) (Figs 3.7 c-d). These results are consistent with the previously mentioned work on these piglets using MRI.

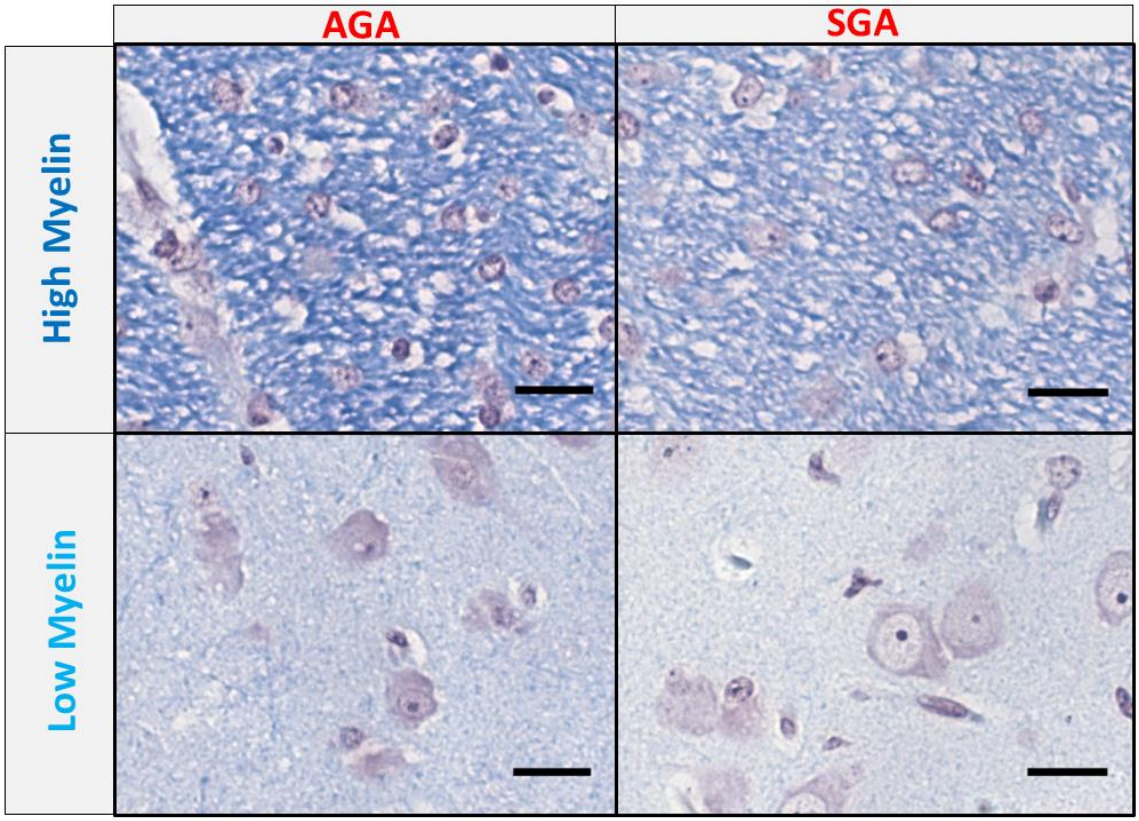

Figure 3.6 Comparison of brightfield frames**.** Single brightfield frames of high and low myelin areas in both appropriate for gestational age (AGA) and small for gestational age (SGA) samples. Scale bar: $35\mu m$.

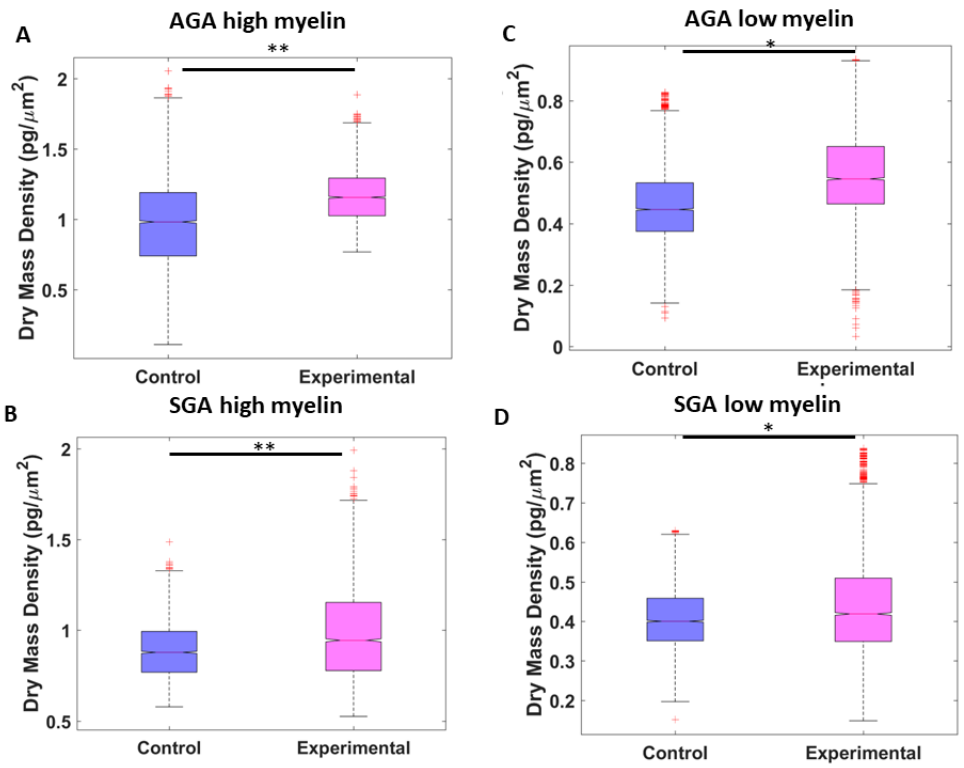

Figure 3.7 Dry mass comparisons. **(a)** Difference in dry mass density per quarter frame of total AGA tissue with high myelin, **(b)** SGA with high myelin, **(c)** AGA with low myelin, **(d)** and SGA with low myelin. (* $p<0.05$, ** $p<0.01$).

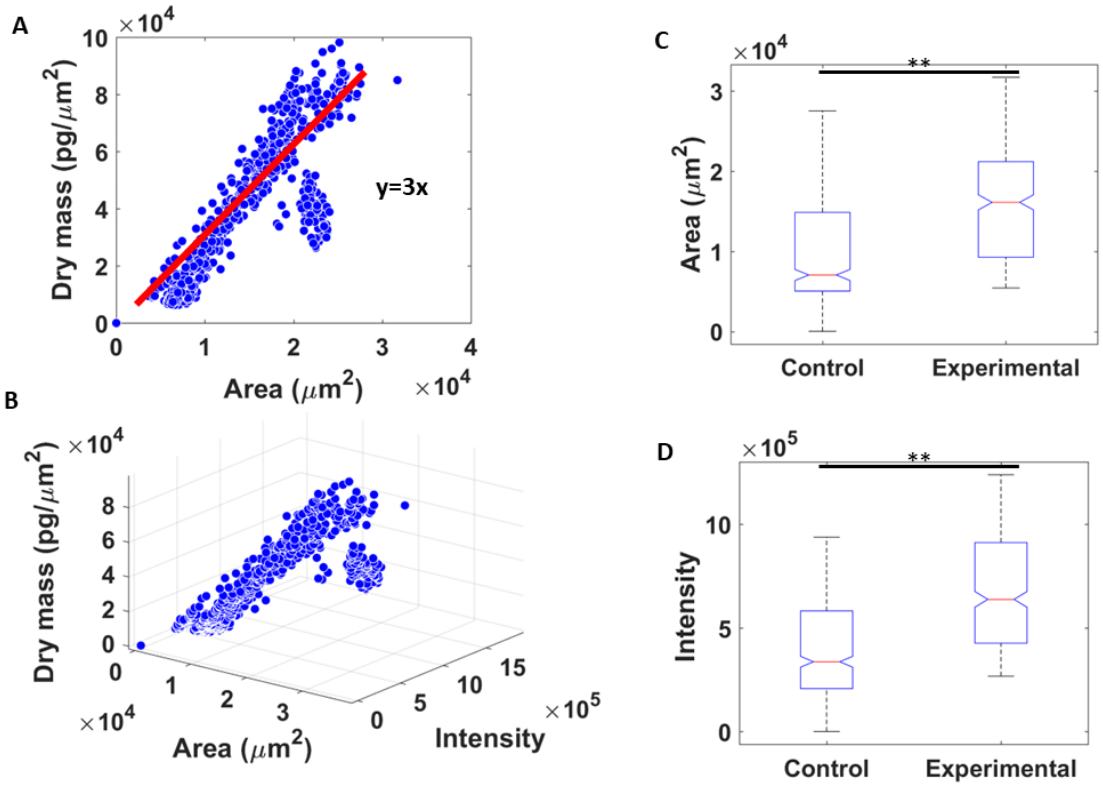

Figure 3.8 Relationship between dry mass, area and intensity. **(a)** Dry mass of myelin from 100 frames of 10 slides plotted against the area of the binary masks, **(b)** 3D plot of dry mass, area of the mask, and color intensity of the fibers, **(c)** difference between control and experimental slides in mask area, **(d)** and difference between control and experimental slides in color intensity (** $p<0.01$).

3.5 Summary and Discussion

Our findings extend the field of analytical techniques that can quantify myelin in complex brain slices. Specifically, we present evidence that our method can detect differences in myelin dry mass using both the CLARITY method in mouse brain samples, and a nutritional intervention previously shown to impact myelination in the internal capsule of SGA and AGA piglet brains. This is an important advance in the field given both the importance of myelination in brain development and function, and the difficulty of quantitatively measuring myelin in brain slices.

To date, myelin measurement studies have been largely qualitative or have involved indirect quantifications and cumbersome, costly procedures. Novel quantitative approaches that are efficient and accurate are needed to enhance our understanding of deficient myelination and assess possible nutritional remedies.

In order to compare dry mass differences from diet with those of the binary masks and color intensities, all three features were computed in 100 frames from each slide of the average category. The area values were calculated by summing the binary masks, and the intensity values were evaluated from segmented brightfield images. Fig 3.8a shows the correlation between dry mass density and the corresponding binary areas. Fig 3.8b is a 3D plot of all three properties, indicating a strong positive relationship. Figs 3.8 c-d show that significant differences between diet categories can be obtained using only the binary mask area and color intensity in brightfield images.

We employed CLARITY to mouse brain samples to validate the ability of cSLIM to detect variations in myelination under controlled conditions that specifically removed lipids. Coupled with a segmentation based on the LFB stain, we measured myelin differences with great sensitivity. Our methodology successfully detected CLARITY-mediated decreases in myelin dry mass. These findings indicated that cSLIM is sensitive to myelin lipid loss following demyelination.

We then tested the ability of cSLIM to recapitulate previously reported nutritionally and birth status driven differences in myelination in the internal capsule of piglets. These changes in myelin dry mass were substantially smaller in magnitude than the changes caused by CLARITY. Further, differences in myelination caused by birth status (SGA vs AGA) are likely to be qualitatively different from those caused by changes in dietary fat. We were able to reproduce the

higher internal capsule myelin dry weight in AGA compared to SGA piglets using cSLIM in blinded fashion. We also reproduced the HF-mediated increase in internal capsule myelin dry weight in both SGA and AGA piglet brain samples. Additionally, we compared the dry myelin weight in the parenchyma surrounding the internal capsule to both the relevant internal capsule and across AGA and SGA and found substantially lower myelin density. Taken together, our results demonstrated that cSLIM was able to detect differences in myelin dry weight across a wide range of myelin concentrations in challenging biological tissues.

In summary, we have introduced a new technique for quantifying myelin content in brain tissue. Our approach involves the combination of the cSLIM imaging modality with a specificity mask provided by the simultaneous brightfield image of the stained tissue. To test our system, we imaged samples from piglets of different gestational ages fed diets with or without HF. We were able to recapitulate previous MRI findings using cSLIM in a blinded protocol. cSLIM can thus quantitate myelin content with high sensitivity and offers great promise for aiding the design of nutritional interventions for brain health.

We plan further studies to calibrate and fine-tune our assessment of myelin. For example, we plan to evaluate the absolute protein content of myelin at the single axon level by creating specificity masks using fluorescent tags for myelin proteins, such as the proteolipid protein. Co-culturing neurons and oligodendrocytes would allow an investigation into the dynamic formation of myelin around a single axon, in real-time. The development of technologies and imaging modalities for directly investigating myelination, deficiencies of myelin, and the processes of demyelination (disease) and remyelination (repair) in the context of dietary interventions is warranted given the substantial disability and high mortality rate associated with human myelin disorders, and particularly, those associated with IUGR and SGA.

CHAPTER 4: Label-free screening of brain tissue myelin content using phase imaging with computational specificity (PICS)

4.1 Abstract

As discussed in Chapter 3, inadequate myelination in the central nervous system is associated with neurodevelopmental complications. Thus, quantitative, high spatial resolution measurements of myelin levels are highly desirable. We combined SLIM micrographs with an AI classifying model that allows us to discern subtle disparities in myelin distributions with high accuracy. This concept of combining QPI label-free data with AI for the purpose of extracting molecular specificity has recently been introduced by our laboratory as phase imaging with computational specificity (PICS). Training on eight thousand SLIM images of piglet brain tissue with the 71-layer transfer learning model Xception, we created a two-parameter classification to differentiate gestational size and diet type with an accuracy of 82% and 80%, respectively. To our knowledge, this type of evaluation is impossible to perform by an expert pathologist or other techniques.

4.2 Introduction

As discussed in Chapter 2, myelin is a proteolipid-rich membrane that covers axons and provides the necessary insulation to effectively transmit electrical neural signals throughout various brain regions [62]. As well, quantitative phase imaging (QPI) [47,49,53,55,84,86-89,102-112] is a label-free imaging approach that can evaluate pathlength changes in biological samples at the nanometer scale. QPI has numerous medical diagnostic applications [85]. Di Caprio et al have applied QPI to research sperm morphology [113], and Marquet et al. have used QPI to study living neurons [114], Lee et al. to study cell pathophysiology [115] and Din et al. to examine macrophages and hepatocytes[116].

Conventional quantitative phase methods, however, use coherent light sources that tarnish image contrast with speckles. With the use of a broadband field, SLIM overcomes this disadvantage, and measures nanoscale information and dynamics in live cells by interferometry [44].

In Chapter 2 we discussed the analysis of piglet brain tissue using color spatial light interference microscopy (cSLIM) [58,117], which uses a brightfield objective and an RGB camera, and generates 4 intensity images, one of which is a standard LFB color image. Thus, cSLIM simultaneously yields both a brightfield image and a phase map. We showed that appropriate for gestational age (AGA) piglets have increased internal capsule myelination (ICM) compared to small for gestational age (SGA) piglets, and that a hydrolyzed fat diet improves ICM in both[118] . However, this analysis was largely manual.

Recently, there has been growing interest in applying the capacity of AI to investigate specific datasets in medical fields [119-126]. AI has special image processing capabilities to discern multi-faceted features that would otherwise elude trained pathologists. Deep convolution networks provide the opportunity to test thousands of image related feature sets to recognize specific tissue configurations [127,128].

Here, we apply phase imaging with computational specificity (PICS)[129,130] a new microscopy technique that combines AI computation with quantitative data to extract precise molecular information. Specifically, we combine deep learning networks with SLIM data to define subtle myelin variations in brain tissue, a strategy undertaken for the first time to our knowledge. We used a SLIM-based tissue scanner in conjunction with deep learning methods to classify the associated gestational size and diet of the tissue, which is inherently linked to myelin distribution and mass density. Such a system does not require staining of tissue. However, we performed our measurements on LFB stained samples and computationally normalized the phase maps to account

for the effects of the stain [58]. The refractive index of stained tissue is expected to vary from that of unstained tissue because of the absorptive properties of the stain. Our normalization technique has been developed by comparing the phase maps of the same tissue samples before and after staining. Furthers details on this calculation can be found in the original cSLIM paper[58].

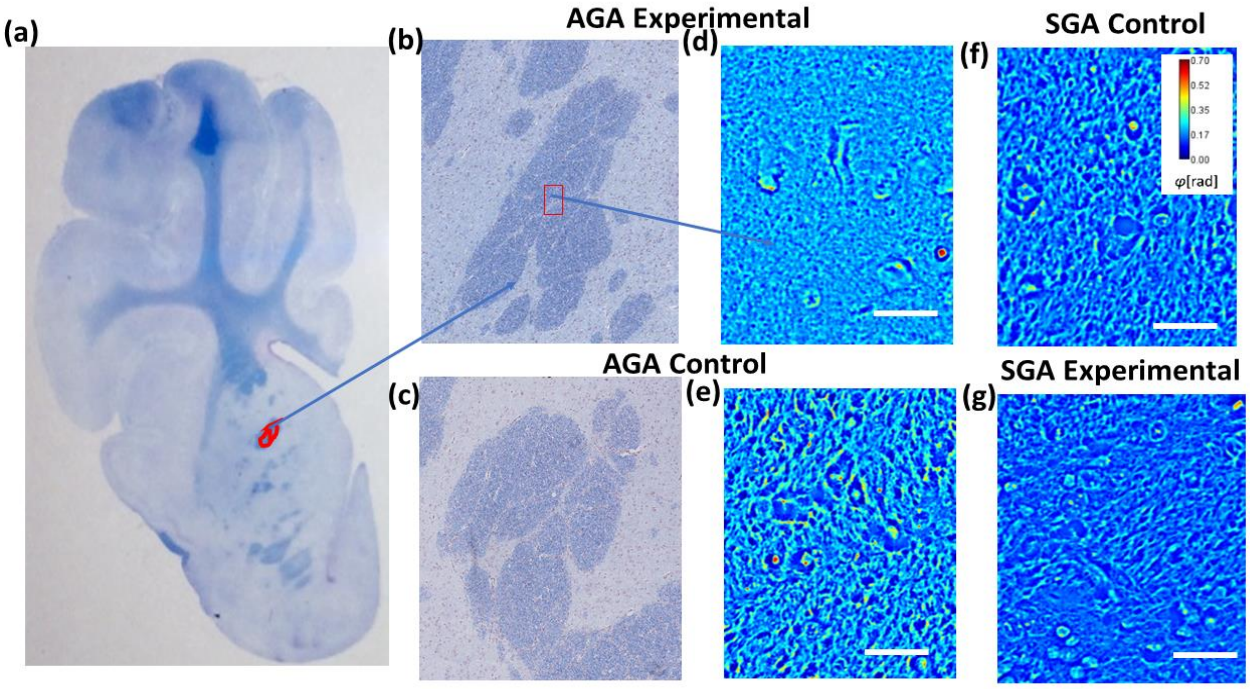

Figure 4.1 (a) Image of one of the 16 brain sections with the internal capsule demarcated in red. **(b)** Stitched mosaic of an internal capsule of an AGA piglet with experimental diet obtained using 625 cSLIM images. **(c)** Stitched mosaic of an internal capsule of an AGA piglet with control diet obtained using 625 cSLIM images. **(d)** Sample AGA experimental-diet frame, **(e)** sample AGA control-diet frame, **(e)** sample SGA control-diet frame, **(g)** sample SGA experimental-diet frame. Scale bar 50 μm.

4.3 Methods

4.3.2 Phase Imaging with Computational Specificity (PICS)

We have combined deep learning with SLIM data to predict gestational size and diet regimen from single images. Our label-free SLIM scanner comprises custom hardware and in-house developed software. The interface enables scanning of the slide with automated focus adjustment. Depending on the focus points selected for the four edges of the area to be imaged, an

interpolation of z-values is calculated to ensure adequate focus throughout measurement. The size of a frame in this case is 255 µm x170 µm (1624 pixels x 1224 pixels), and the lateral step size is 1580 µm and 1180 µm, horizontally and vertically, which allows sufficient overlap to create stitches. The duration of the scan for 25 x25 images is 10 minutes after the setup of focus points. The SLIM principle of operation relies on phase shifting interferometry applied to a phase contrast setup (see Ref. 30 for details). An add-on module (Cell Vista SLIM Pro, Phi Optics, Inc) with a spatial light modulator is connected to a commercial phase contrast microscope (Axio Observer Z1, Zeiss). We shift the phase delay between the incident and scattered field in increments of $\pi/2$ and acquire 4 respective intensity images, which suffices to extract the phase image unambiguously. Figure 4.1 shows examples of SLIM images of piglet brain tissue corresponding to the area of the internal capsule (IC).

4.3.3. Deep Learning Model

We employed a transfer learning approach in our deep learning framework to construct our machine learning classifier. This technique is recommended for training a model when there is a relatively small number of image instances.

As outlined in Figure 4.2 a, we selected the Xception model, which comprises 71 layers and has been pretrained on a large dataset of over 1.6 million images of different sizes and groups. Xception is the most accurate pretrained model with the least number of parameters[131,132]. We also selected this model due to its robust feature extraction capacity and superior performance with our data instances over alternatives, such as ResNet [133] and MofileNet [134]. We fine-tuned the base model to include two dropout layers of 0.75 (Fig. 4.2. a).

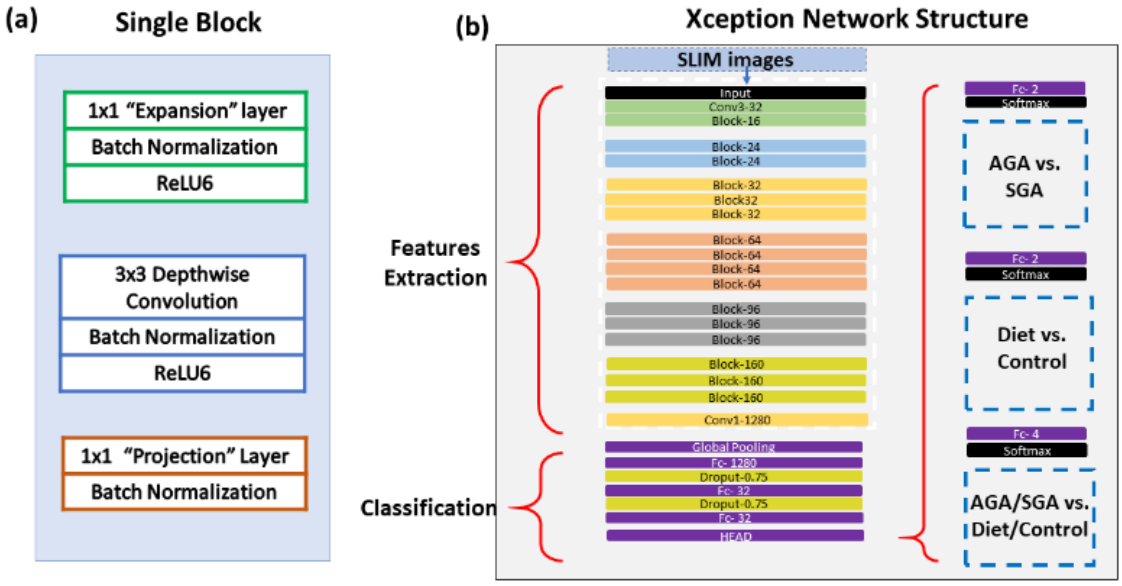

Figure 4.2 (a) Machine learning Xception network components of a single block. **(b)** Entire network structure with a finetuned classification segment and three different output models.

4.4 Results

4.4.1 Data

Our training data included 8,016 out of the total 10,000 SLIM images of piglet brain samples, obtained from 16 sections of different piglets divided equally between four categories: AGA-diet, SGA-diet, AGA-control, and SGA-control. Full IC reconstructions and sample frames are illustrated in Figures 4.2 b-c. 992 images were reserved in each category and randomly selected for validation as well as for testing. Brightfield images were not included in the model, as we wanted to achieve label-free detection without any stain. The patch size of 1624 x 1224 pixels coincided with the field of view of our imaging equipment. Images were augmented for training using rotation, x-axis flip, and y-axis flip. The phase distributions of the various groups are displayed in Figures 4.3a-f. Each graph displays one of the six possible pairings of the four

categories. Figures 4.3a-b show the different phase distributions caused by diets in the same gestational classes, while figures 4.3 c-d show such differences caused by gestational age in the same diet categories. Figures 4.3 e-f contrast mixed diet-age distributions. The closeness and extent of overlap for each combination illustrates the minute numerical differences in the pixels, suggesting that diagnostic capabilities are largely due to differences in spatial distributions and phase density. This is further substantiated in the statistical differences in dry mass measurements of the same samples found in our previous study [117] only after applying binary myelin masks to the quantitative data.

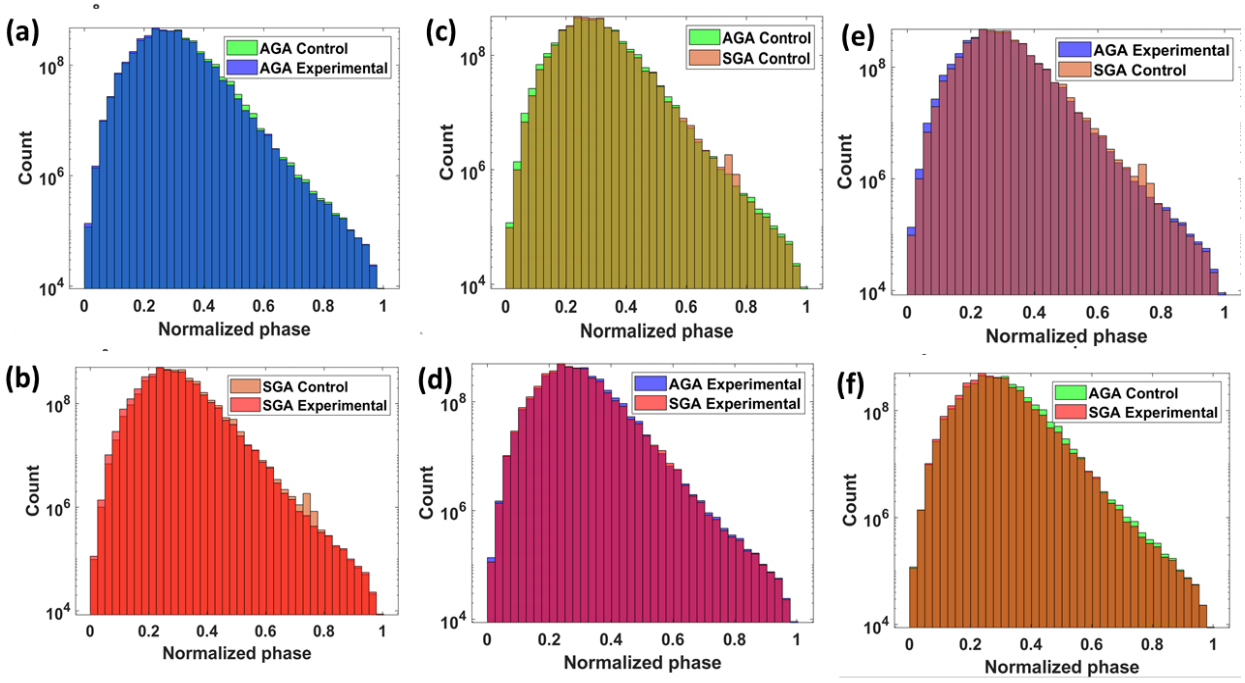

Figure 4.3 Histograms of the count of pixel data in SLIM images for **(a)** AGA groups, **(b)** SGA groups, **(c)** Control diet groups, **(d)** Experimental diet groups, and **(e-f)** mixed gestational age and diet groups.

4.4.2 Model Accuracy and Loss

Model accuracy and losses for three types of classifications are shown in Figure 4.4. In the case of distinguishing brain tissue based on diet regimens, we obtained an accuracy of 80% (Fig. 4.4 a) and a loss of 0.35 (Fig. 4.4 b). These results are significant considering that the subtlety of these difference would otherwise be undiscernible to a trained histopathologist. There is negligible underfitting or overfitting in these models and they could be characterized as having appropriate and balanced fitting. In the case of classifying phase maps based on gestational size, the results were slightly stronger with an accuracy of 82% (Fig. 4.4 C) and a loss under 0.3 (Fig. 4.4 d). There is minimal underfitting in this model, however the training loss is noisy near the final epochs, while the validation loss is relatively smooth, likely due to a greater variety of instances in the training set and the large number of parameters being evaluated. Lastly, the results for the classification of both diet and gestational age categories are, as is expected, considerably lower with an accuracy of 63% and a slight degree of underfitting (Fig. 4.4 e). The loss values are also higher than individual comparisons, tapering off at the final epochs around 0.8 instead of 0.3 (Fig. 4.4 f).

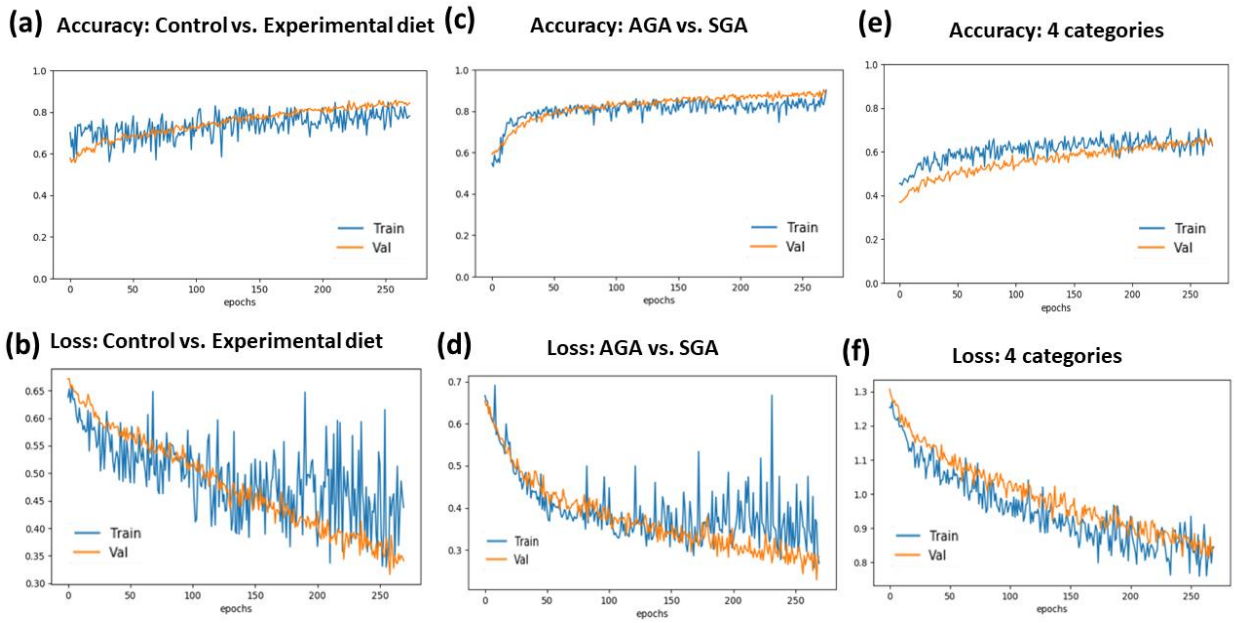

Figure 4.4 Plots for diet classification **(a)** accuracy and **(b)** loss, **(c)** gestational size accuracy and **(d)** loss, and **(e)** all categories accuracy and **(f)** loss.

4.4.3 Confusion Matrices for Validation and Loss

The confusion matrix offers a quantitative indication of the performance of a classifier. There are four classes in our confusion matrix: “Diet - AGA”, “Control - AGA”, “Diet - SGA”, and “Control - SGA”. This confusion matrix can have three kinds of errors: the sample can be labelled incorrectly in terms of diet, gestational size, or both. In the case of a perfect classification model, the confusion matrix is diagonal with only true negatives or true positives. Figure 4.5a shows a 4x4 confusion matrix for the classification of each category on all test images from 16 slides.

The first row, corresponding to the Control-AGA category, indicates 80% of samples labelled correctly with most errors attributed to designating the samples with the same diet but with a *small* gestational size. The second row, corresponding to Diet-AGA, has 74% correct

labelling, with most errors due to a mismatch of the diet type. The third row, for Control-SGA, has 71% correct labeling and the last row, for Diet-SGA, has only 62% correct labelling, with 14% mislabeled as Control-SGA. The AGA categories outperform those of SGA, presumably due to a lower myelin abundance inherent in the smaller gestational size, which may have been counterbalanced by the experimental diet, thereby confusing the Diet-SGA category with either AGA classes.

To further validate our model on slides that were not used for training, we evaluated images from an untrained slide that is associated with an experimental diet and SGA. This is a test that is separate and additional to the 10% of images used for testing from the 16 sections. The results, shown in a confusion matrix (Fig. 4.5.b), were better than anticipated, exceeding the performance of test images in this category, with a true positive rate of 72 % for both size and diet, with 77% for just diet, and 94% for just size.

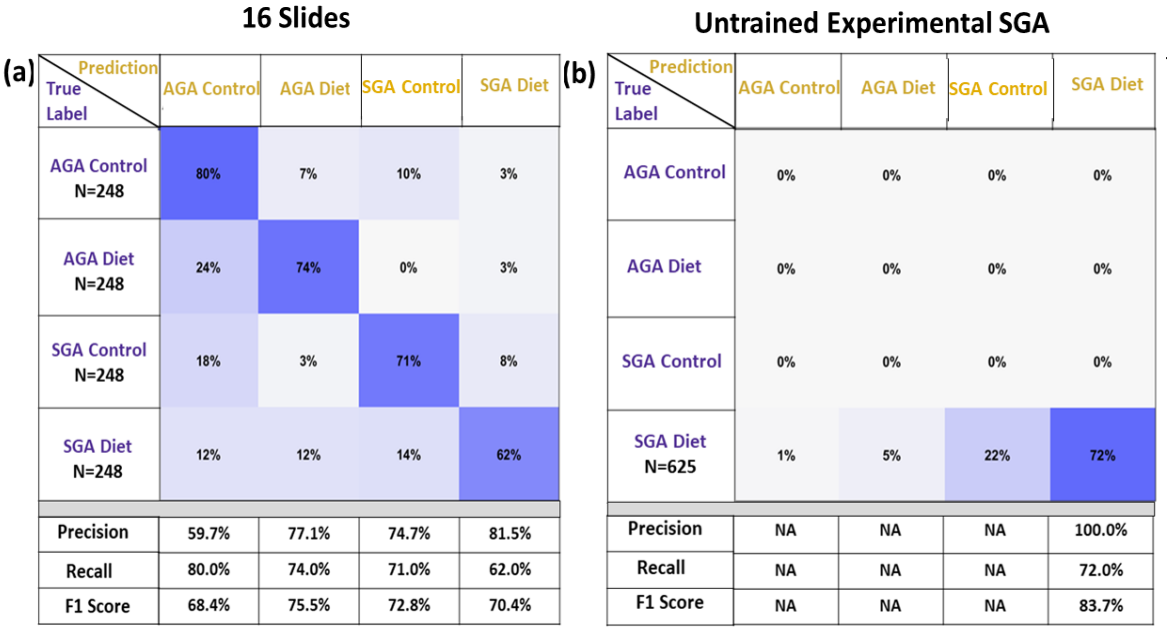

Figure 4.5 (a) Confusion matrix for classification of all four categories on the 16 slides that were used for training, and **(b)** confusion matrix of an untrained Experimental diet-SGA slide.

4.5 Conclusions

Current histopathological findings depend on manual investigations of stained tissue slices under a microscope by a trained pathologist. The alternative methods of assessing myelin density, such as MRI and PIXE, are indirect, cumbersome, and costly. Here, we present evidence that our method of combining AI with spatial light interference microscopy (SLIM) can quickly determine differences in myelin content without the use of molecular stains or manual analysis. This is an important contribution to neuroscience, especially given the significance of myelination in brain development and the current challenges of measuring myelin quantitatively.

We demonstrated that applying AI to SLIM images delivers excellent performance in classifying single phase maps of brain tissue to detect the level of myelin adequacy. The approximately 80 percent accuracy outcomes for both binary distinctions, and 62 percent for all four categories, indicate that the proposed method may be useful in quick screenings for cases of suspected myelin disorders. These results are significant as it would otherwise be impossible for a trained histopathologist to distinguish such myelin discrepancies. Not only does this technique offer automatic screening, but multiple tissue samples can be analyzed rapidly as the overall throughput of the SLIM tissue scanner is comparable with that of commercial whole slide scanners. One way to improve on these results without simply adding more images, while keeping the samples label-free, would be to infer additional information through digital staining. This has already been performed successfully with phase images[129], RI tomography[135], and autofluorescence[11]. In our case, artificially recreating the LFB stain or a myelin proteolipid protein fluorophore could help enhance our results.

Future scope thus includes evaluating myelin content with multiple modalities and creating specificity masks using fluorescent tags for constituent proteins. Employing PICS to mimic such tags would facilitate investigations into the dynamic generation of myelin around axons in real-time.

CHAPTER 5: White Blood Cell Detection, Classification and Analysis using Phase Imaging with Computational Specificity (PICS)

5.1 Abstract

Treatment of blood smears with Wright's stain is one of the most helpful tools in detecting white blood cell abnormalities. However, to diagnose leukocyte disorders, a clinical pathologist must perform a tedious, manual process of locating and identifying individual cells. Furthermore, the staining procedure requires considerable preparation time and clinical infrastructure, which is incompatible with point-of-care diagnosis. Thus, rapid and automated evaluations of unlabeled blood smears are highly desirable. In this chapter, we used color spatial light interference microcopy (cSLIM), a highly sensitive quantitative phase imaging (QPI) technique, coupled with deep learning tools, to localize, classify and segment white blood cells (WBCs) in blood smears. The concept of combining QPI label-free data with AI for the purpose of extracting cellular specificity has recently been introduced in the context of fluorescence imaging as phase imaging with computational specificity (PICS). We employed AI models to first translate SLIM images into brightfield micrographs, then ran parallel tasks of locating and labelling cells using EfficientNet, which is an object detection model. Next, WBC binary masks were created using U-net, a convolutional neural network that performs precise segmentation. After training on digitally stained brightfield images of blood smears with WBCs, we achieved a mean average precision of 75% for localizing and classifying neutrophils, eosinophils, lymphocytes, and monocytes, and an average pixel-wise majority-voting F1 score of 80% for determining the cell class from semantic segmentation maps. Therefore, PICS renders and analyzes synthetically stained blood smears rapidly, at a reduced cost of sample preparation, providing quantitative clinical information.

5.2 Introduction

White blood cells (WBCs) are essential components of the immune system and of the body's protection against infections. The five key forms of WBCs are lymphocytes (including B and T cells), eosinophils, neutrophils, monocytes and basophils. In healthy individuals, these WBC populations have specific concentration ranges and any deviations from these parameters are clinically informative [136].

Wright's staining of blood smears is one of the most common methods for detecting white blood cell aberrations[137]. However, it is time-consuming and laborious for a clinical pathologist to detect and identify individual cells in order to diagnose leukocyte abnormalities. Furthermore, the staining procedure is involved, which altogether makes diagnosis tied to a clinical infrastructure. Another way to calculate WBC relative percentages is with flow cytometry, where fluorescently labeled antibodies are used to differentially mark WBC populations [138]. With long-established laboratory procedures, this approach is widely used in clinical practice. Modern cytometers, such as mass cytometers, can evaluate up to 40 parameters in any single measurement. However, they are limited to analyzing cell phenotypes based on the expression degree of antibody labels, similar to fluorescence-based cytometers[139].

Recent efforts to further facilitate these tasks by analyzing label-free white blood cells include the use of intensity-based imaging flow cytometry [138,140], in which the benefits of digital microscopy, such as the measurement of morphology, are combined with the high-throughput and statistical certainty of a flow cytometer. Using this technique, white blood cells can be detected, classified and counted. However, this method requires expensive equipment, involved sample preparation, is of low resolution, and does not provide quantitative information on cellular components.

Phase imaging approaches typically use coherent light sources, which compromises multiple factors of image quality, such as signal-to-noise ratio (SNR) and contrast, due to speckles. SLIM overcomes this drawback by using a broadband field to derive nanoscale details and dynamics in live cells using interferometry[44]. This system, as discussed in Chapter 3, uses a brightfield objective and an RGB camera, and generates 4 intensity images, a regular color micrograph being one of them. This image, $\varphi(x,y)$, is a data matrix relating to the nanoarchitecture of the imaged sample.

As shown in Chapter 4, there has recently been a surge of interest in using AI to analyze relevant datasets in medical fields [119-126] . AI has unique image processing capabilities allowing it to detect multi-dimensional features that qualified pathologists would otherwise miss. Deep convolutional networks enable thousands of image-related feature sets to be tested to recognize complex biological data [127,128].

Here, we apply phase imaging with computational specificity (PICS)[129,130,141], a novel microscopy technique that combines AI computation with quantitative data, to analyze WBCs in blood smears. Specifically, we combine deep learning networks with cSLIM micrographs to detect, classify and segment four types of white bloods cells: neutrophils, lymphocytes, monocytes, and eosinophils. To the best of our knowledge, this is the first time such a strategy has been implemented. Such a system does not require staining of cells as we convert phase maps, which contain biologically relevant data into Wright's stain brightfield images. This is unprecedented and indisputably valuable for standard clinical produces requiring the accurate assessment of WBCs without the use of tedious preparations and extraneous labels.

5.3 Methods

5.3.1 Blood Smears Preparation

Eighteen blood smears stained with Wright's stain were used for our analysis. Each smear was scanned in a configuration of 12x12-40 frames, depending on the size of the 'zone of morphology,' to avoid clumped areas at the application point as well as sparse areas near the feathered edge. Examples of brightfield and counterpart phase images (3x4 frame stitches) of the smears are shown in Figures 5.1 a-b, with zoom-in instances of a neutrophil, monocyte, eosinophil, and lymphocyte in Figures 5.1 c-f. Each slide was imaged to produce both brightfield and quantitative channels. The classifications of boundaries and segmentations were performed manually in MATLAB using the 'Image Labeler' application. Basophils were omitted from analysis due to insufficient numbers needed for training and validation. The ground truth classification of the WBCs was performed by a board-certified hematopathologist. The procedures used in this chapter for conducting experiments using human subjects were approved by the institute review board at the University of Illinois at Urbana–Champaign (IRB Protocol Number 13900). Furthermore, all blood smear slides came already fully prepared, and all methods were carried out in accordance with relevant guidelines and regulations, and dissociated from patient statistic, with informed consent that was obtained from all subjects and/or their legal guardians.

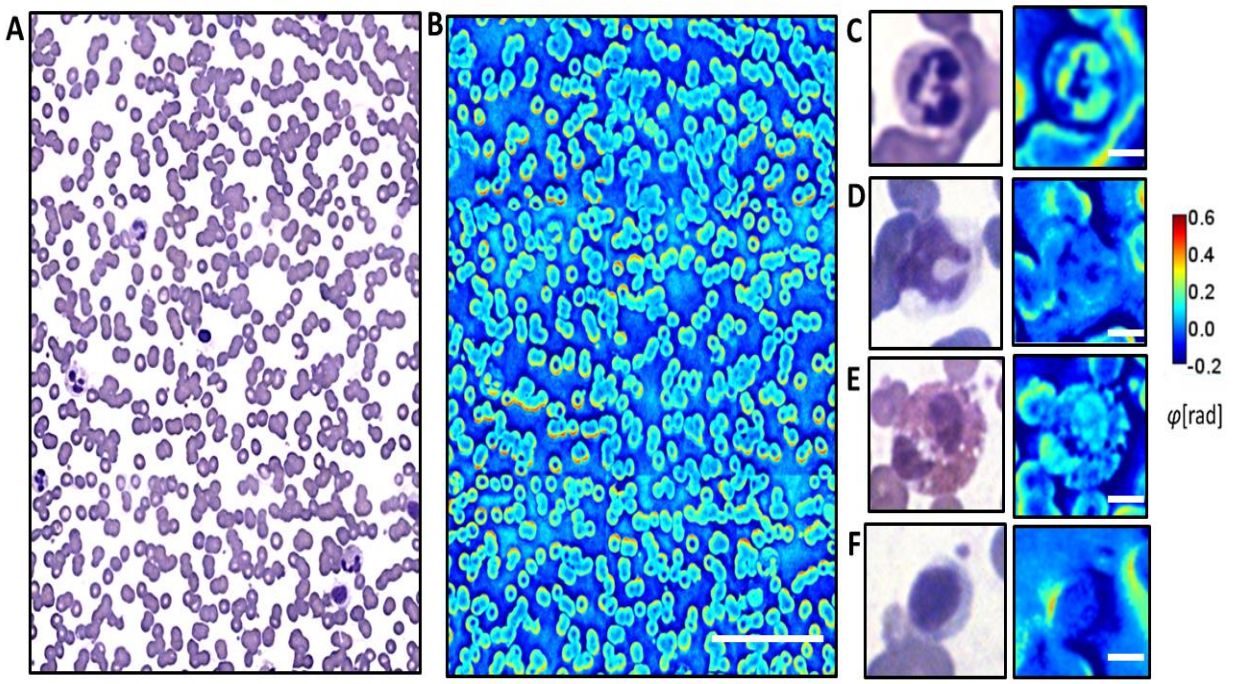

Figure 5.1 Blood smear images. **(a)** 3x4 stitch of brightfield images from a single scan. Scale bar: 200 µm. **(b)** corresponding SLIM images to **(b)**. Examples of **(c)** a neutrophil, **(d)** monocyte, **(e)** eosinophil, and **(f)** lymphocyte in brightfield and phase channels. Scale bars: 5 µm.

5.3.2 Image-to-image translation

The purpose of converting phase images to the original brightfield version is for situations when an unstained slide is imaged, or a slide is captured with a grayscale camera. The phase map created with cSLIM is the equivalent of these versions. A translation from QPI to Wright's stain, as far we know, has never been heretofore achieved.

The conversion of SLIM micrographs to artificial brightfield images of stained WBCs was accomplished using a conditional generative adversarial network (GAN) based network called pix2pix[13]. GAN models have been very successfully at converting micrographs types from one modality to another[119,142]. A total of 504 images were used for processing and among these 50 images were held out as test images. The remaining images were split between training and

validation in an 8:1 ratio. In this pix2pix network, there are two components: a generator (G) and a discriminator (D). The task of the discriminator is to distinguish between a real image and the fake image generated by the generator. The generator and discriminator play an adversarial min-max game, the GAN loss can be mathematically written as:

$$L_{cGAN}(G,D) = E_{x,z}[\log D(x,y)] + E_{x,z}[\log(1 - D(x,G(x,z))] \quad (5.1)$$

where $E_{x,z}$ is the expected value over real and fake instances, x is the input image, and z is the random noise. This trains the generator *G* to create artificial images which are supposed to fool the discriminator. An L1 loss is also combined with this GAN loss for more stable training. An Adam optimizer[143] with a learning rate of 0.0002 was used to train the generator and the batch size was set to 2. Input SLIM images were downsampled to 512X512 to fit the GPU memory.

The semantic segmentation was performed in multiple steps as shown schematically in Figure 5.2. The EfficientDet model[144] was used for localization and classification of different WBC classes. A U-Net was used to generate binary segmentation maps of WBC cells. The localizations and binary maps were combined to generate semantic segmentation map through a process described below. The same test images were used in these steps also. The training and validation data were split randomly 5 times, and with each trained model the localization, classification and segmentation was performed with the same set of testing images. The detailed descriptions of these steps are given below.

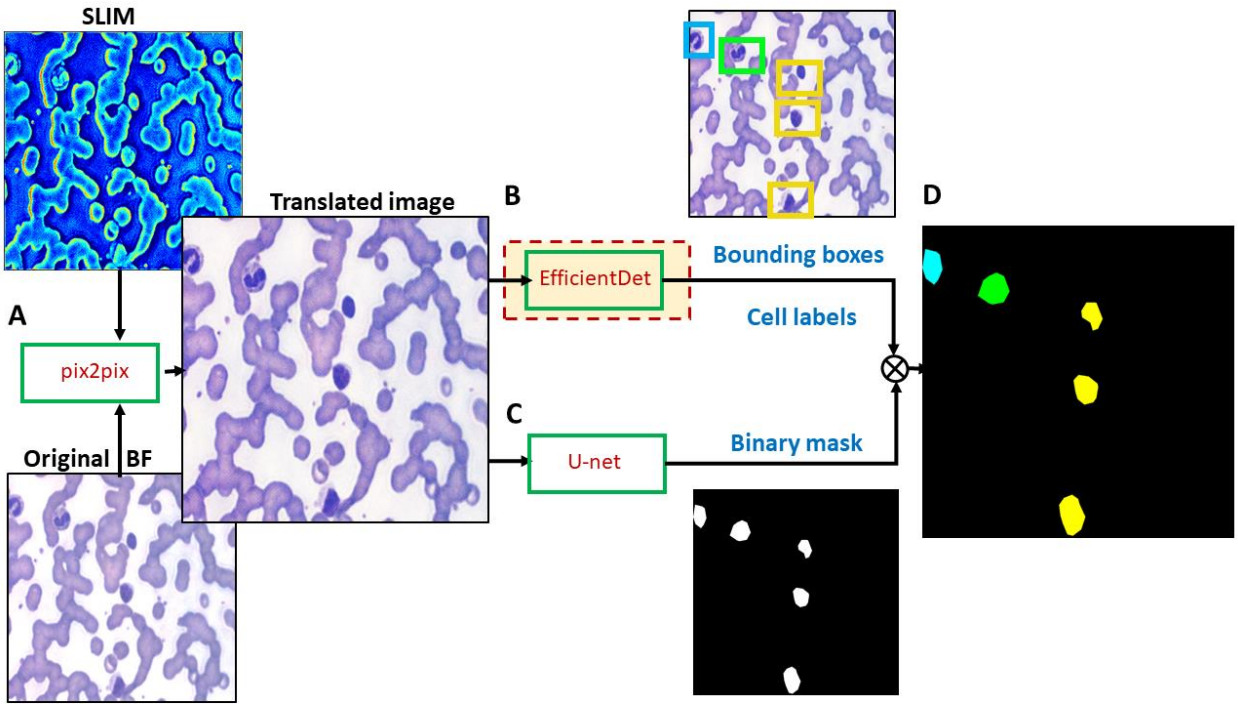

Figure 5.2 Image processing. **(a)** The procedure for analyzing WBCs begins with an image-to-image translation with pix2pix from SLIM to brightfield. **(b)** The translated image is then trained with EfficientDet to locate and classify all cell types, **(c)** in parallel with a U-net that produces binary masks of the WBCs. **(d)** Finally, combining both networks enables the semantic segmentation of different WBCs in each frame.

5.3.3 Localization and Classification of WBCs

The localization and classification of white blood cells were performed by a state-of-the-art deep learning-based object detection model, EfficientDet[144]. The EfficientDet model took an image as input and predicted localization-bounding boxes with associated WBC class labels. An example of a rectangular label is shown in Figure 5.3. In Figure 5.2, a generic schematic is shown where the input of the EfficientDet model is a translated brightfield image. In this chapter, the architecture of the EfficientDet was specified as EfficientDet-D0. It uses EfficientNet-B0 as the backbone network for feature extraction. The weights of EfficientNet-B0 in the EfficientDet model were initialized with an EfficientNet-B0 that was pre-trained on the ImageNet dataset [145] for an image classification task. The whole EfficientDet network was subsequently fine-tuned by use of

the translated images in the training set. In the fine-tuning process, the EfficientDet was trained by minimizing a compound focal and smooth L1 loss that measures the classification errors and bounding box prediction errors, respectively[144]. The loss function was minimized with an Adam optimizer[143] with a batch size of 8. The learning rate was set to 5×10^{-5}, which was determined based on the network performance on the validation set. The network training was stopped if the mean average precision (mAP) of validation set did not increase for 10 consecutive epochs. The EfficientDet network weights that yielded the highest validation mAP during the training process were selected to establish the final EfficientDet model.

The trained EfficientDet was tested on the unseen testing set with mAP as the performance metric. The mean classification and localization time per frame was 140 ms. For a more robust evaluation, the training process described above was repeated five times corresponding to the five random partitions of training and validation data. These five EfficientDet models were tested on the same unseen testing set. The corresponding outcomes are discussed in the *Results* section of this chapter.

5.3.4 Binary Segmentation WBCs

For binary segmentation of WBC cells, a U-Net network was used. The U-Net model took a translated brightfield image as input and predicted a binary map in which each pixel represented either WBC class or background class. An example of how cells were labeled for this is shown in Figure 5.3 b. In Figure 5.2, a general schematic is shown where the input to the U-Net model is a translated brightfield image and the output is a binary segmentation map.

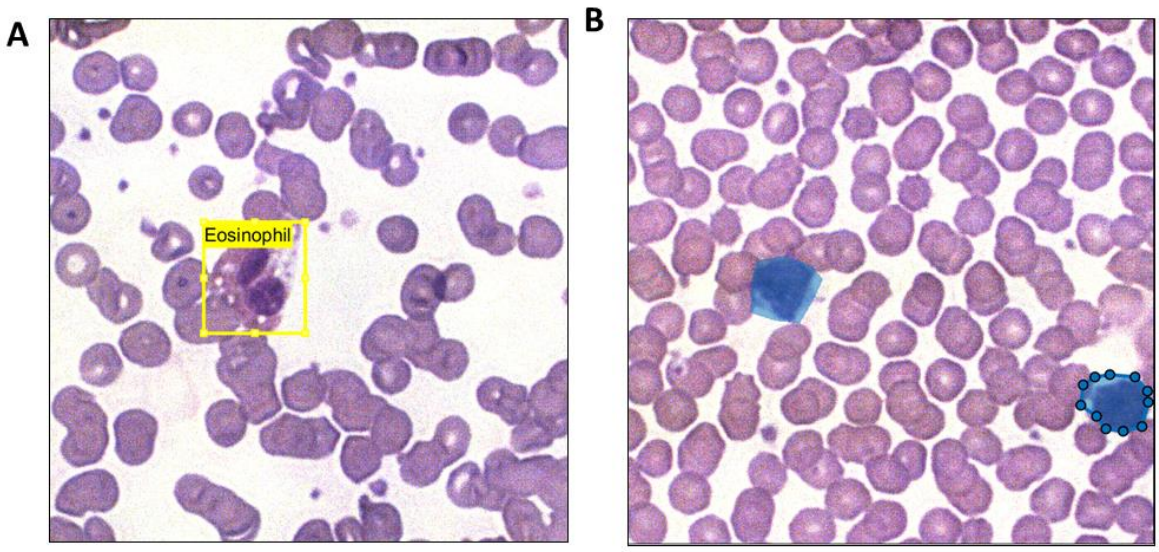

Figure 5.3 Labelling examples using the MATLAB imageLabeler for both **(a)** rectangle (in this case of an eosinophil) and **(b)** pixel labels (in this case of two lymphocytes).

The architecture of the U-net consists of 5 blocks and 4 blocks in the expansion path and contraction path, respectively. Each block in the expansion path includes a convolutional layer, Max-pooling layer, and a BatchNorm layer; each block in the contraction path includes a convolutional layer, an up-sampling layer, and a BatchNorm layer.

The training and validation sets used for U-Net were consistent with those used for the previous EfficientDet model training. In this step, the ground truth for each image sample was the binary mask map of WBCs. The U-Net was trained by using an Adam optimizer[143] to minimize the mean squared error loss that measures the difference between the ground truth segmentation map and the prediction of the U-Net. The learning rate and batch size were 3×10^{-5} and 2, respectively. The validation loss was monitored in the training process. The network training was stopped if there was no decrease in validation loss for 5 consecutive epochs, while we chose the weights corresponding to the lowest validation loss. The training process was repeated five times based on the same partitions of training and validation data described previously. Additionally, the

testing dataset was the same as described in the previous section of image-to-image translation, with mean processing times of 110 ms per frame.

5.3.5 Semantic Map Generation

In the previous two steps, localization-classification of WBC cells using EfficientDet model and binary segmentation by U-Net model were described. This step combined the results of these previous two steps to generate semantic maps. In Figure 5.4, for a given translated brightfield image, the output of the EfficientDet model and U-Net model were combined to generate the semantic segmentation map. The semantic segmentation map was generated by combining the predicted labeled boxes and binary maps in a pixel-wise manner, described as follows: the pixels outside cell regions in the binary map were classified into the background class. For pixels inside cell regions, if they also existed inside one unique labeled box, these pixels were classified into the WBC class of the associated cell box; if a pixel was contained within two or more labeled boxes, which was observed to be a very rare case in our studies, the pixel was classified into the WBC class of the labeled box with the highest confidence score according the majority class; in all other cases, the pixels were assigned to the background class.

With the five pairs of trained EfficientDet and U-Net models in the previous two steps, five semantic maps were generated for a given translated image. The five semantic maps were finally combined into one for a more reliable prediction by applying a pixel-wise majority-voting process. The combined semantic map was the final predicted semantic map for the image. Pixel-wise recall, precision, and F1 scores were used to evaluate the semantic segmentation performance of the proposed approach on the unseen testing set. The pixel-wise recall, precision, and F1 scores were

computed between the predicted semantic maps and their ground truth values for all the images in the unseen test. The corresponding results are discussed in the *Results* section.

5.4 Results

Our dataset included 504 images that were selected from the scans to include white blood cells. We analyzed 267 neutrophils, 117 eosinophils, 192 lymphocytes, and 82 monocytes. There were insufficient basophils to include in the set. Due to the natural proportion of white blood cells to one another, with neutrophils comprising 40-60%, lymphocytes 20-40%, monocytes 2-8%, and eosinophils 1-4% of total WBCs [146,147], it was difficult to deliberately make an even number of cells in each category. Although the SLIM images contribute new structural information, the color disparity in some of the cellular components is sometimes diminished, such as in WBC nuclei.

In Figure 5.4, a sample translated brightfield image, generated by the image-to-image translation model from an input SLIM image, is shown along with the corresponding original brightfield images. Visually, both the images appear identical. Upon closer inspection, it can be seen that some of the WBC nuclei are not as dark in hue as in the original images, and the background is slightly grainy in some areas. Figure 5.4 d shows the combined GAN and L1 loss plots of the generator. The model weights corresponding to the lowest validation loss were chosen to generate the translated brightfield images from the test set SLIM images. The quantitative results for localization, classification and segmentation are described in the following sections.

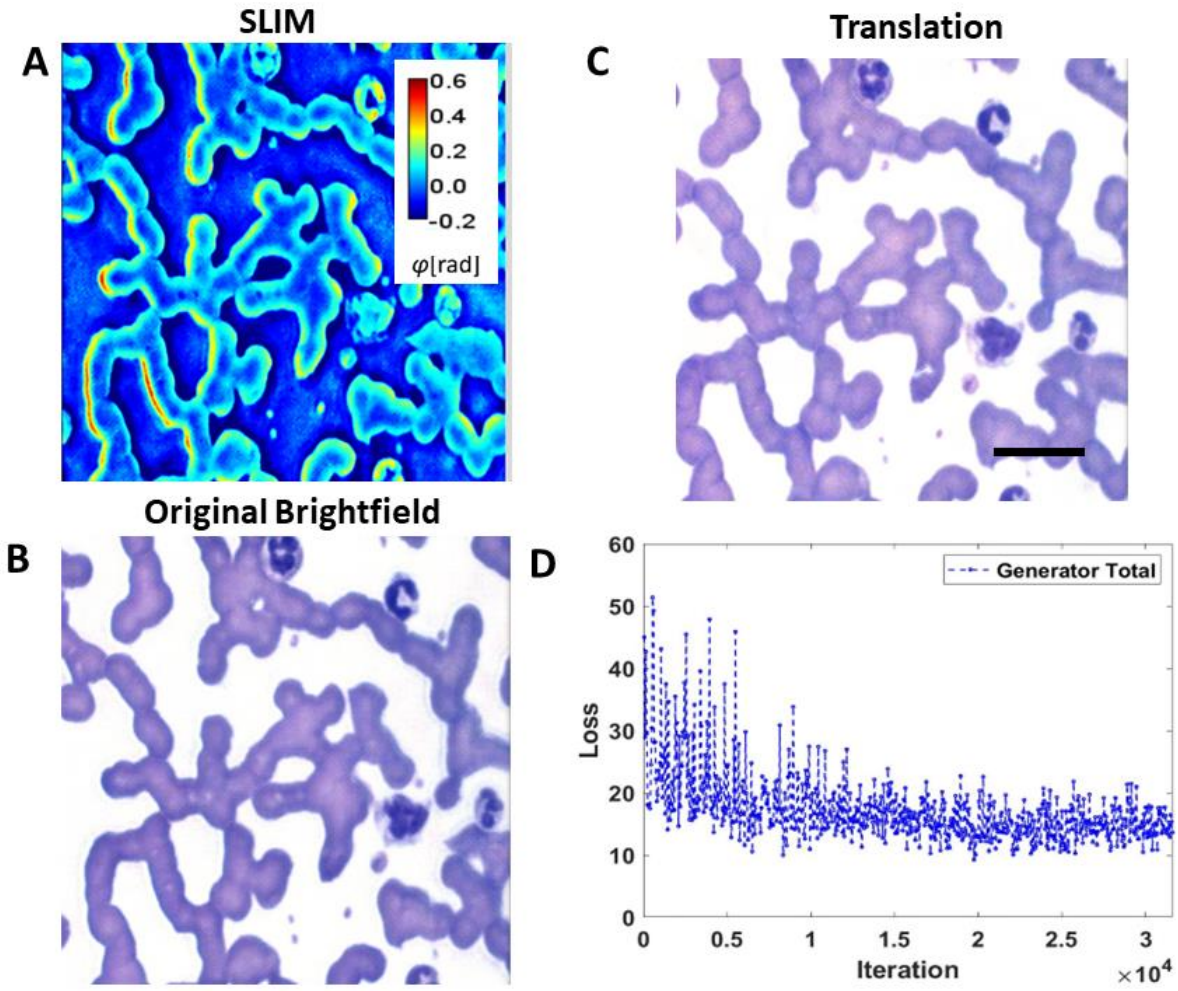

Figure 5.4 Image-to-image translations. **(a)** Example of an input SLIM micrograph. **(b)** Corresponding brightfield image that serves as ground truth. **(c)** The translated brightfield output of the model. **(d)** Loss plot of the training sessions, combing GAN and L1 losses. Scale bar: 25 μm.

5.4.1 Localization and Classification

The mean and standard deviation of mAPs for the four categories (neutrophils, eosinophils, lymphocytes, and monocytes) corresponding to five sets of testing are shown in Table 1. For a comparative analysis, we employed the same strategy to train five EfficientDet models with annotated SLIM images and ground truth brightfield images, respectively. The corresponding results are shown in Table 1.

Table 5.1. Localization and Classification. Mean average precision (AP) values for localization and classification of all five test sets, using EfficientDet, for SLIM, brightfield and translated images.

Category	Test 1 mAP	Test 2 mAP	Test 3 mAP	Test 4 mAP	Test 5 mAP	*mean mAP*
SLIM images	0.7581	0.7543	0.7301	0.7196	0.6696	0.7263 +- 0.032
Brightfield images	0.8476	0.8545	0.8544	0.8736	0.8112	0.848 +- 0.02
Translated images	0.7742	0.7805	0.6877	0.7569	0.7363	0.7469 +- 0.03

In general, the brightfield and translated images both produced better results for the four WBC categories in terms of the average mAPs over the five test sets. An example of a labeled translated image is shown in Figure 5.5 a. In this case, there is an eosinophil in the bottom left corner that is recognized and correctly labeled with 99% certainty. In the top right corner, a neutrophil is correctly labeled with 91% certainty. These values are not indicative of all respective cell types, even in the case of localization and classification, but only pertain to these specific cases. The Precision-Recall curves for each WBC in all tested translated images are shown in Figure 5.5b, with comparisons of original image types in Figure 5.6.

The best performance is that of the eosinophils, with a precision score of 90.09%, likely due to a very distinctive red granular cytoplasm, and the lowest is that of lymphocytes, with 56.6 %, likely because many large lymphocytes appear similar to small monocytes, even to a trained pathologist. These translated images were produced using only quantitative phase image input and can therefore be regarded as being equivalent to unlabeled blood smears.

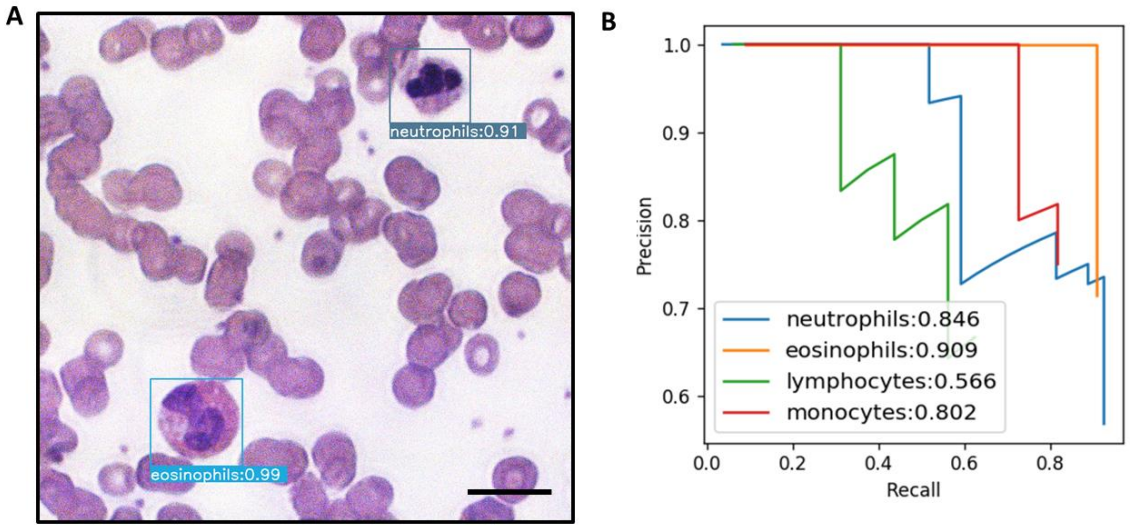

Figure 5.5 Localization and classification. **(a)** Example of an input translated brightfield micrograph with an eosinophil and neutrophil located and classified with 99% and 91% certainty, respectively. **(b)** Precision-Recall curves for all cell categories in all images. Scale bar: 20 µm.

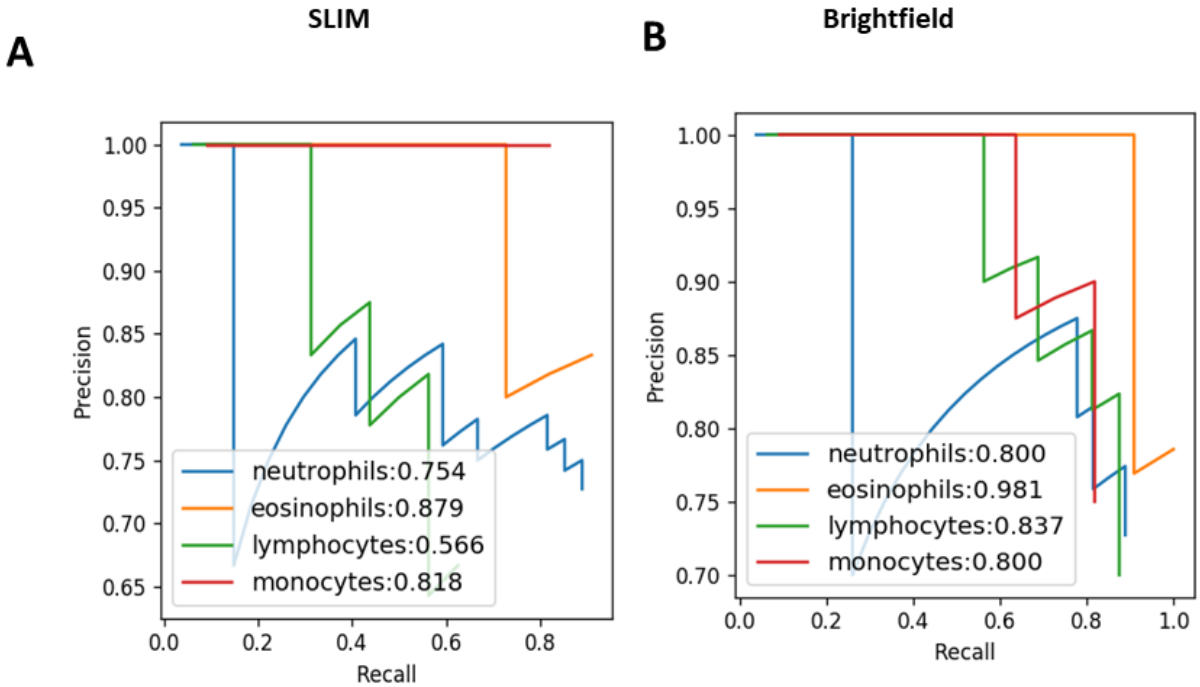

Figure 5.6 Precision-recall curves for SLIM **(a)**, and brightfield **(b)** images.

5.4.2 Segmentation

The results of the semantic segmentation on translated images are listed in Tables 5.2-3. These numbers are based on pixel-wise F1 scores. Eosinophils had the highest scores, with 86.7%, and neutrophils and lymphocytes had the lowest, with 68.5%, for reasons similar to those in localization and classification tasks. These results confirm the reliability of the translated model to convert unseen, unstained quantitative phase images into typical Wright's stain brightfield images.

Table 5.2. Semantic Segmentation. Semantic segmentation results in terms F1 scores for all five test sets, and the average values for all three image versions.

	Test 1	Test 2	Test 3	Test 4	Test 5	average
SLIM	0.785	0.769	0.749	0.762	0.709	0.7548+-0.026
BF	0.81	0.819	0.82	0.831	0.796	0.8152+-0.012
Trans	0.796	0.81	0.749	0.742	0.735	0.7664+-0.031

Table 5.3. Majority Voting**.** Results based on the combination of all five semantic maps for a reliable prediction with majority-voting: F1 scores for image and cell classes, with average values in the rightmost column.

Class	Background	neutrophils	eosinophils	lymphocytes	monocytes	average
SLIM	0.996	0.716	0.925	0.591	0.701	0.786
BF	0.997	0.755	0.901	0.696	0.797	0.829
Trans	0.997	0.685	0.867	0.685	0.757	0.798

An example of a WBC segmentation is shown in Figure 5.7 for SLIM, brightfield and translated cases. In this example there is a neutrophil in the top right corner, one in the bottom left corner, and a lymphocyte in the bottom left corner. Figures 5.7 d-f are the predicted labels from the model, and Figures 5.7 g-i are the ground truth, with further examples presented in Figure 5.8. Both brightfield and translated images have predicted labels similar to the ground truth, with all three cells correctly identified.

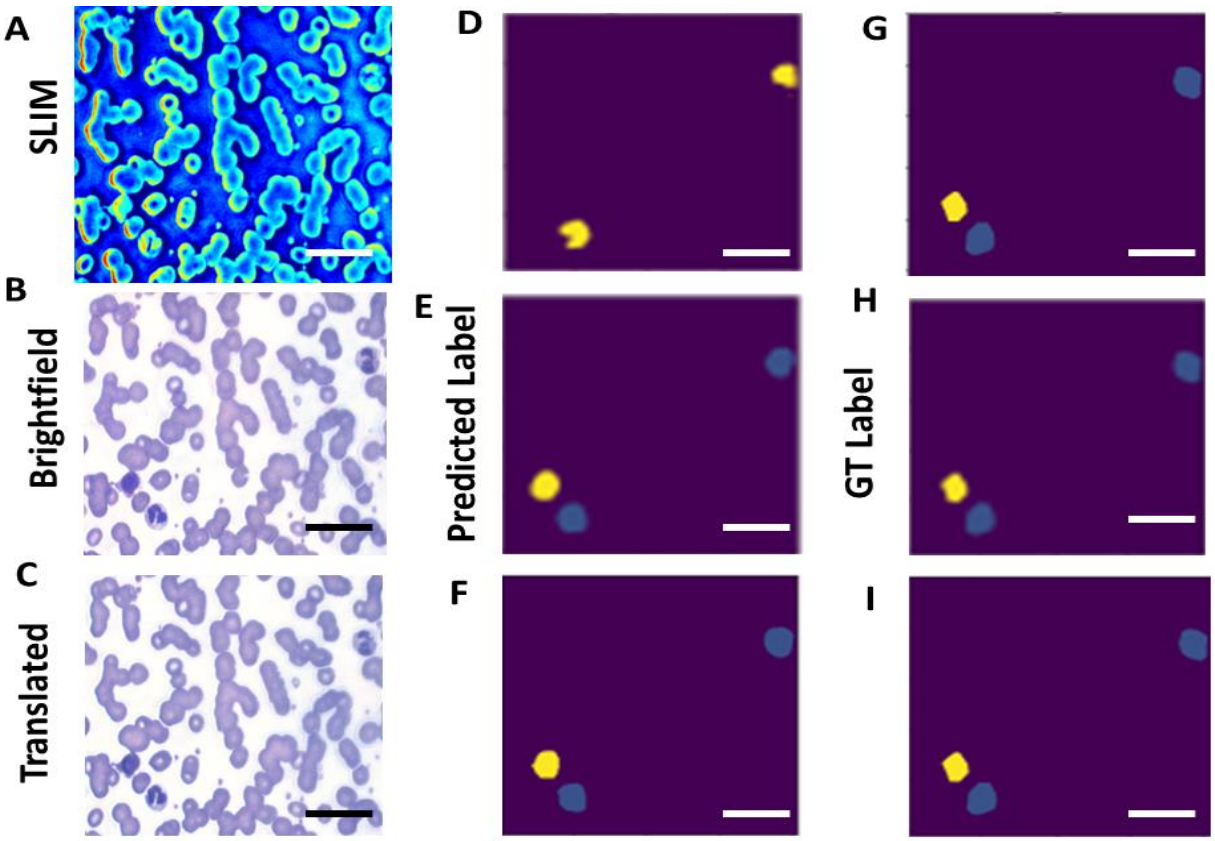

Figure 5.7 Semantic segmentation results. **(a)** Example SLIM input, **(b)** example brightfield input, and **(c)** example translated input. **(d-f)** Corresponding predicted labels, and **(g-i)** corresponding ground truth labels. Scale bars; 20 µm.

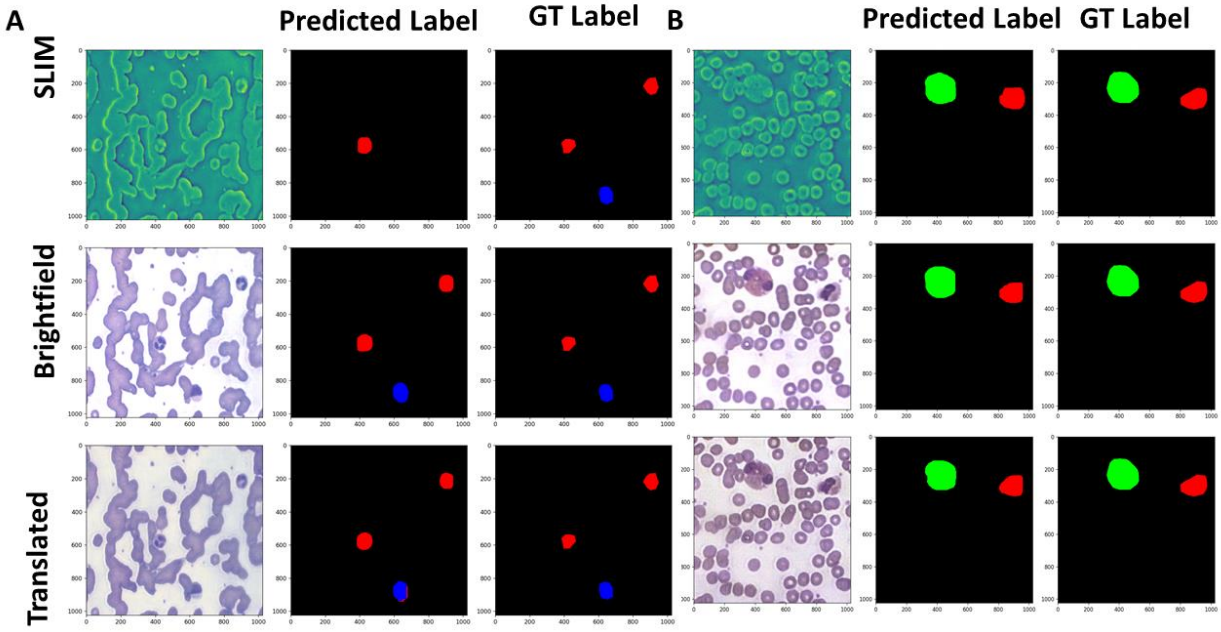

Figure 5.8 Prediction examples for a frame with **(a)** two neutrophils(red) and a lymphocyte (blue) and **(b)** a frame with an eosinophil (green) and a lymphocyte (red).

5.5 Discussion

Here, we present evidence that our method of combining AI with color spatial light interference microscopy (cSLIM) can quickly identify different white blood cells, such as neutrophils, monocytes, lymphocytes and eosinophils, without manual analysis. This is an important contribution to blood smear analysis, especially given the significance and multitude of leukocyte complications. We demonstrated that applying AI to cSLIM images delivers excellent performance in first artificially generating brightfield micrographs and afterwards localizing and classifying different WBCs. The results for all four categories indicate that the proposed method may be useful in quick screenings for cases of suspected leukocyte disorders.

Not only does this technique offer automatic screening, but multiple blood smear slides can be evaluated rapidly as the overall throughput of the cSLIM scanner is comparable with that

of commercial whole slide scanners. Inferring additional information through digital staining would be one way to improve upon these results other than simply adding more images, while keeping the samples label-free. This has recently been accomplished with phase images[148], RI tomography[135], and autofluorescence[11]. In our case, artificially recreating various fluorescent tags to identify specific components of white blood cells, such as a molecular tag for human neutrophil elastase (HNE), could help enhance our results. Future scope includes evaluating more images with sufficient instances of basophils and bands to add to the current WBC categories list, as well as imaging blood smears with specific leukocyte abnormalities, such as autoimmune neutropenia and leukemia.

CHAPTER 6: GANscan: Continuous Scanning Microscopy using Deep Learning Deblurring

6.1 Abstract

Most whole slide imaging (WSI) systems today rely on the "stop-and-stare" approach, where, at each field of view, the scanning stage is brought to a complete stop before the camera snaps a picture. This procedure ensures that each image is free of motion blur, which comes at the expense of long acquisition times. In order to speed up the acquisition process, especially for large scanning areas, such as pathology slides, we developed an acquisition method in which the data is acquired continuously while the stage is moving at high speeds. Using generative adversarial networks (GANs), we demonstrate this ultra-fast imaging approach, referred to as GANscan, which restores sharp images from motion blurred videos. GANscan allows us to complete image acquisitions at 30x the throughput of stop-and-stare systems. This method is implemented on a Zeiss Axio Observer Z1 microscope, requires no specialized hardware, and accomplishes successful reconstructions at stage speeds of up to 5,000 μm/s. We validate the proposed method by imaging H&E stained tissue sections. Our method not only retrieves crisp images from fast, continuous scans, but also adjusts for defocusing that occurs during scanning within +/- 5μm. Using a consumer GPU, the inference runs at <20ms/ image.

6.2 Introduction

Numerous microscopy applications require large fields of view (FOV), including digital pathology [149], micro-mirror and biosensor assembly [150], and *in vivo* imaging [151]. Acquisition time demands are a major bottleneck to fixing modest or partially filled FOVs in standard microscopy techniques. Improvements in both hardware and computation are thus actively sought to push the efficiency of optical measurements beyond traditional boundaries. Accelerating either image

acquisition or analysis can have drastic benefits in diagnostic assessments and has been shown to provide critical advantages in cell detection[152], disease screening[153], clinical studies[154] and histopathology[155,156].

In standard microscope systems, the objective lens dictates the resolution and field-of-view (FOV), forcing a trade-off between the two parameters. In commercial whole slide scanners, the FOV is extended through lateral scanning and image mosaicking. Most forms of microscopy require serial scanning of the sample region, which slows down measurement acquisitions and diminishes the temporal resolution.

There are three classes of strategies used in traditional microscopy for slide-scanning. The first technique uses the so called “stop-and-stare" style, which entails sequentially moving the sample across a scanning grid, pausing the stage, and exposing the camera for discrete recordings. This tactic generates high-quality images as a result of long measurement durations, but is not especially time-efficient[157]. A second technique involves illuminating a moving sample with bursts of light that help circumvent the motion blur, which would otherwise compromise the image resolution. As a result of the short exposure times with this method, the resulting images have a relatively poor signal-to-noise ratio (SNR)[157]. Thus, there is a cost to optimizing image clarity or acquisition speed in these approaches. Third, there are line scanning [158] and time-delay integration (TDI) [159] methods, which use 1D sensors, where a camera vertically handles continuous signals line by line to reduce read-out time and increase SNR. However, even the latest versions of these instruments require specialized imaging equipment and readout methods[160,161].

Different imaging methods have been proposed to improve the throughput of scanning-based microscopy techniques, such as multifocal imaging[162] and coded illumination[157]. Computational methods of microscopy imaging[163-167], such as ptychography, which scans and

fuses portions of spatial frequencies, can produce large FOVs with resolutions that surpass the objective's diffraction limit. However, these solutions end up either complicating the microscopy system configuration, deteriorating the image quality, or extending the post-processing period. Additionally, iterative algorithms that are used in Fourier ptychography to reconstruct an image from a sequence of diffraction patterns often suffer from convergence issues[168].

The mechanical specifications of the scanning stage, rather than the optical parameters of the microscope, generally hinder the throughput performance of WSI systems[169]. The space-bandwidth product (SBP), which is the dimensionless product of the spatial coverage (FOV) and the Fourier coverage (resolution) of a system, can quantify the information across an imaging system[170]. Enhancements to the SBP have been the objective of various innovations in imaging techniques [5,6,9,171-173], but typically require either specialized hardware or time-consuming post-processing.

The advent of accessible deep learning tools in recent years has led to a new host of strategies to address lingering microscopy challenges [172], including super-resolution imaging [174], digital labeling of specimens[119,129,175-180], Fourier ptychography microscopy[171], and single-shot autofocusing[181], among others[182]. These methods, which take advantage of recent breakthroughs in deep learning, need no modification to the underlying microscopic gear and produce faster and more comprehensive imaging results than traditional image reconstruction and post-processing algorithms. Generative adversarial networks (GANs), which comprise two opposing networks competing in a zero-sum dynamic, have been especially prominent in image-to-image translation tasks, due in large part to their outstanding execution of pixel-to-pixel conversions[119,142].

In this work, we propose a computational imaging technique, termed GANscan, which employs a GAN model to restore the spatial resolution of blurred videos acquired via continuous

stage scanning at high speeds using a conventional microscopy system. Our method involves continuously moving the sample at a stage speed of 5,000 μm/s and an acquisition rate of 30 frames per second (fps). This acquisition speed is on par with the state-of-the-art TDI technology of 1.7-1.9 gigapixels in 100 seconds [159,161]. However, unlike TDI, our approach is using standard optical instrumentation, which lowers the threshold for broad adoption in the field.

In contrast to other high-throughput imaging endeavors, GANscan adds no complexity to the hardware, with single frame restorations that can be computed in a matter of milliseconds. The results of this novel technique demonstrate that basic modifications in measurements, coupled with artificial intelligence (AI), can provide the framework for any rapid, high-throughput scanning operation.

This chapter is structured as follows: first, we present the workflow for continuous imaging microscopy in both slow and fast acquisitions. Second, we describe the theory behind blur motion artifacts and why deconvolutions are limited in restoring the spatial bandwidth of control images. Third, we discuss the imaging procedures and registration of slow-moving samples with the motion-smeared ones. Fourth, the parameters of the GANscan network are explained, as well as the data processing techniques prior to model training. Lastly, reconstruction performances are evaluated using an unseen test set, including a test set from different patients, which is also compared against stop-and-stare controls and deconvolutions using standard image metrics.

6.3 Theory and Results

6.3.1 Workflow

Figure 6.1 depicts the workflow of our approach. To demonstrate the benefits of this technique, we imaged a large sample of a pathological slide of a ductal carcinoma in situ (DCIS) biopsy,

covering roughly half a standard microscopy slide area (~30 mm x 15 mm), as well as an unstained blood smear. All slides studied in this work were divorced from patient statistics, with consent from Carle and Christie Clinic in Urbana, Il, and their use was approved by the institute review board at the University of Illinois at Urbana–Champaign (IRB Protocol Number 13900). Both slides were scanned in a row-major configuration, capturing movies across the slide horizontally (Fig. 6.1a). There were no modifications to a standard commercial microscope (Axio Observer Z1, Zeiss), and the only adjustments in the measurement were the speed of the stage and the continuous recording of the camera. In order to obtain ground truth images for training, the same rows were captured at a slow (50 μm/s) stage speed and at the same exposure time of 2 ms. Once pairs of sharp and defocused images were assembled through Pearson correlations, a GAN network was trained to enable restoring unseen motion blurred micrographs (Fig 6.1b).

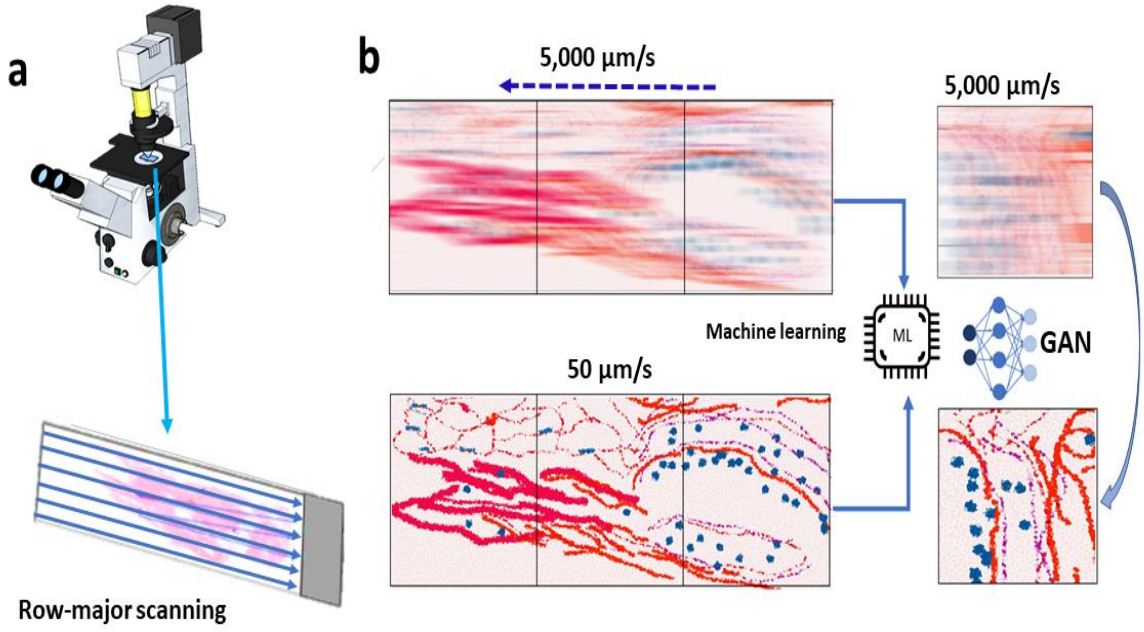

Figure 6.1 (a) Scanning stage of the AXIO observer Zeiss microscope with an example slide showing the row-major continuous scanning direction. **(b)** Motion blurred reconstruction scheme using a slow-moving stage as the control for GAN training.

6.3.2 Theory

At rest, let the image be $I(x,y)$. During the sample translation, the translated image, $\underline{I}$, has the following time dependence:

$$\underline{I}(x,y;t) = I(x+vt,y) \quad (1)$$

where v is the stage speed. Considering the camera integration time T, the "blurred" detected frame is then:

$$\begin{aligned}\underline{I}(x,y) &= \int_{-T/2}^{T/2} I(x+vt,y)dt \\ &= \int_{-\infty}^{\infty} I(x+vt,y)\prod(\frac{t}{T})dt\end{aligned} \quad (2)$$

where $\prod(\frac{t}{T})$ is the 1D rectangular function of width *T*. The integration is the sum of the frames accumulated during the acquisition time T (Fig. 2a).

Using the central-ordinate theorem [183]:

$$\underline{I}(x,y) = \Im_t\{I(x+vt,y)\prod(\frac{t}{T})\}\big|_{\omega=0} \quad (3)$$

Where ω is the angular frequency. Since $I(x+vt,y) = I[v(t+\frac{x}{v}),y]$, the temporal Fourier transform reads

$$\begin{aligned}I(x+vt,y) &= I\left[v\left(t+\frac{x}{v}\right)\right] \\ &\leftrightarrow I[\frac{\omega}{v},y]e^{-i\frac{\omega x}{v}}\end{aligned} \quad (4)$$

where $\leftrightarrow$ indicates the Fourier transformation.

Using the convolution theorem [47], Eq. 3 can be rewritten as:

$$\begin{aligned}\underline{I}(x,y) &= I[\frac{\omega}{v},y]e^{-i\frac{\omega x}{v}}]\circledv_{\omega} sinc(\omega T)\Big|_{\omega=0} \\ &= \int_{-\infty}^{\infty} I[\frac{\omega-\omega'}{v},y]e^{-i\frac{(\omega-\omega')x}{v}}]sinc(\omega' T)d\omega'\Big|_{\omega=0} \quad (5) \\ &= e^{-i\frac{\omega x}{v}}\int_{-\infty}^{\infty} I(\omega',y)sinc(\omega' T)e^{-i\frac{\omega' x}{v}}d\omega'\Big|_{\omega=0}\end{aligned}$$

In Eq. 5, we recognize a Fourier transform of a product, which yields the following convolution operation,

$$\underline{I}(x,y) = I(\frac{x}{v},y)\circledv_{\frac{x}{v}} \prod(\frac{x}{vT}) \quad (6)$$

where $\circledv_{\frac{x}{v}}$ indicates the convolution operator over the variable *x/v*, which has dimensions of time.

This result captures the physical description of the image *spatial* blurring as the result of a *temporal* convolution operation. Thus, the smeared image is the sharp image convolved along the direction of the scan by a rectangular function, which has a width proportional to the acquisition time. For a scanning speed of $v = 5,000\,\mu m/s$ and $T = 2\,ms$, $vT = 10\,\mu m$. This corresponds to a length roughly twenty times the diffraction resolution of our imaging system.

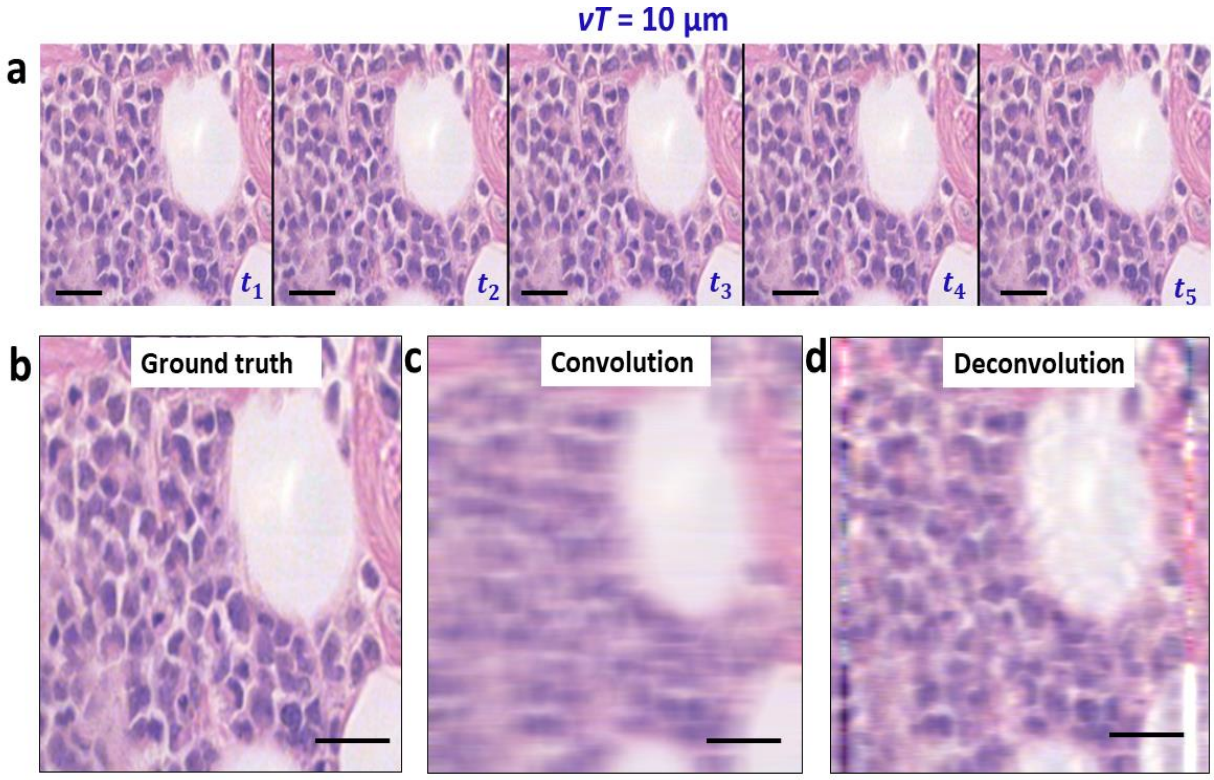

Figure 6.2 (a) A few frames from a video taken with a stage speed of 50 µm/s, with time labels indicating a slow forward movement. **(b)** Middle image of the sharp sequence **a** used as ground truth. **(c)** The convolution of **(b)** with the blur function. **(d)** The deconvolution of **(c)** with the blur function. Scale bar **25 µm.**

6.3.3 Deconvolution

We performed the 1D *deconvolution* on our acquired images, thus, inverting the effect of Eq. 5, and used the results as the standard of comparison for the deep learning results. These deconvolutions were evaluated by first establishing the best match through the 'convolve' filter in ImageJ, and then using the same line dimension in MATLAB with the 'deconvblind' function. This tool deconvolves an image via the maximum likelihood algorithm and a starting estimate of the point-spread function (PSF), which in our case is a single row of 47 pixels of value 1.

A sample frame of the biopsy and its convolution with the line of the blur width are shown in Fig 6.2 b-c, and deconvolving again produces the original frame but with compromised high spatial frequencies (Fig.6.2d). The artifacts of lines along both edges of the image are a result of the filter brushing against the boundaries of the image. The deconvolution operation succeeds at shrinking features horizontally to restore their true width. However, the image still suffers from poor overall resolution, due in part to the higher spatial frequencies being suppressed through the convolving effect of imaging a rapidly moving sample. This shortcoming is our principal motivation of employing deep learning techniques to predict the standard spatial bandwidth.

6.3.4 Image Acquisition

Images were acquired with a commercial microscope (Axio Observer Z1, Zeiss) in brightfield and phase contrast settings and a Point grey color camera, using a Zeiss EC Plan-Neofluar 40x/0.45 NA objective. The samples were a ductal carcinoma in situ (DCIS) breast tissue biopsy and an unstained blood smear of a healthy patient. The stage speed and coordinates were precisely manipulated using the Zeiss MTB (MicroToolBox) software, and the camera settings, such as shutter time (2 ms), frame rate (30 pfs), and gain (8 dB), were selected using the Grasshopper GRAS- 2054C software. For stitching images, a vertical step size of 200 μm was used, and horizontal videos were acquired for 1 minute at the slow speed of 50 μm/s to ensure the correspondence of 15 horizontally adjacent frames in the video captured at 5000 μm/s. The videos of each row at the accelerated stage speed was 0.6 seconds. After the image acquisition, off-line processing involved image registration of blurry and sharp images through MATLAB with Pearson correlation estimates. For the 5,000 μm/s datasets, we extracted 256x256 crops from paired images to create a training volume of 1050 image pairs.

We performed deconvolutions on each input test image and compared them with GANscan results, as shown in Figure 6.3. The mean SSIM of the GANscan biopsy images is 0.82, while the deconvolved images had an SSIM of 0.73, when compared to the same control images. The mean SSIM of the GANscan phase contrast images is 0.73, while the deconvolved images had an SSIM of 0.66, when compared to the same control images. PSNR values were also calculated with GANscan outperforming deconvolutions 27 to 26 for both image types. All analysis was performed in MATLAB.

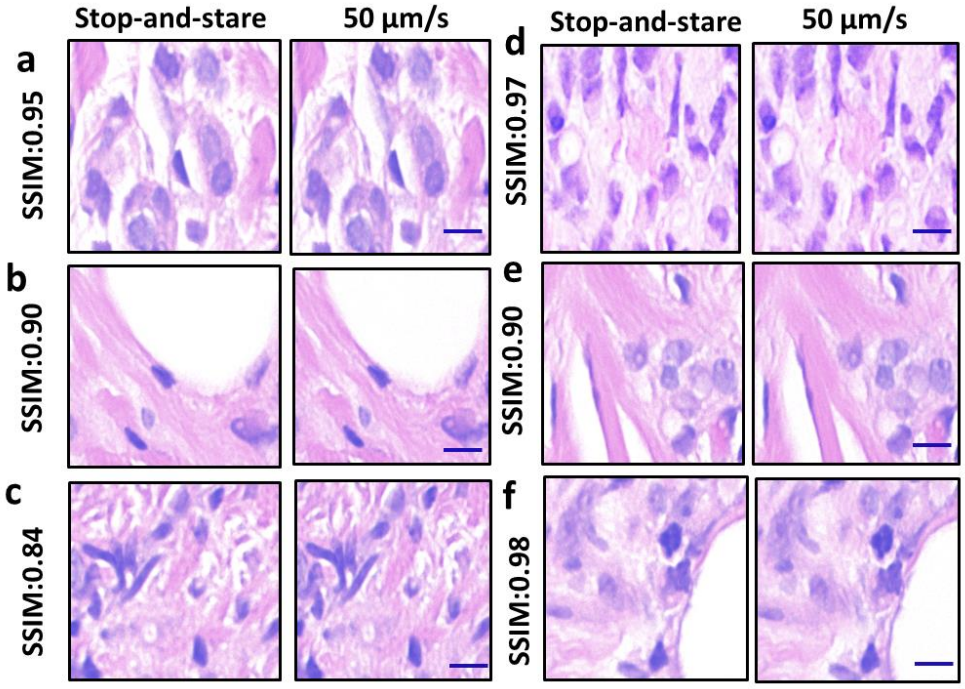

Figure 6.3 (a-f) Example comparisons of stop-and-stare images with images recorded at 50µm/s with SSIM values. Scale bar **5 µm**.

6.3.5 Image Pair Registration

In order to prepare pairs of blurred and sharp images for training, consecutive sharp images in the fast videos were matched to their motion-smeared counterparts by evaluating the maximum Pearson correlations in a set of slightly shifted clear images (Figs. 6.4, 6.5). The "ground truth" images were captured at a stage speed of 50 μm/s, which, at the acquisition time of 2 ms results in a blur size of 0.1 μm, *i.e.*, below the diffraction limit of our system. As a result, there are approximately 100 frames in the sharp videos for each image in the 5,000 μm/s, motioned blurred videos, as shown in Figure 6.4.

Evaluating the Pearson correlation between the input (smudged) frame and a series of potential ground truth frames produces values ranging from 0.4 to 0.76. The frame associated with the highest Pearson correlation value was selected as the ground truth. It should be noted that the rapidly captured images expose the camera to a larger field of view than the slowly-captured ones by the length of the blur, which is 10 μm for a scanning speed of 5,000 μm/s. This difference is delineated in Figure 6.4.

In order to confirm the reliability of the ground truth images obtained at 50 μm/s, standard stop-and-stare images were also acquired for comparison as part of a test set. This was achieved by serially scanning images with a lateral shift of 1 μm, mimicking the distribution of slowly moving images but fully halted. It was necessary to capture sufficient images in order not only to perfectly register the stop-and-stare images with the 50 μm/s images, again using a Pearson correlation computation, but also with the blurry images. As shown in Figure 6.3, the stop-and-stare images look identical to the 50μm/s images, with SSIM values upwards of 0.9. Variability in values is possibility indicative of noise inherent in the images. These are further compared with the moving ground truths against the reconstructed images, discussed below.

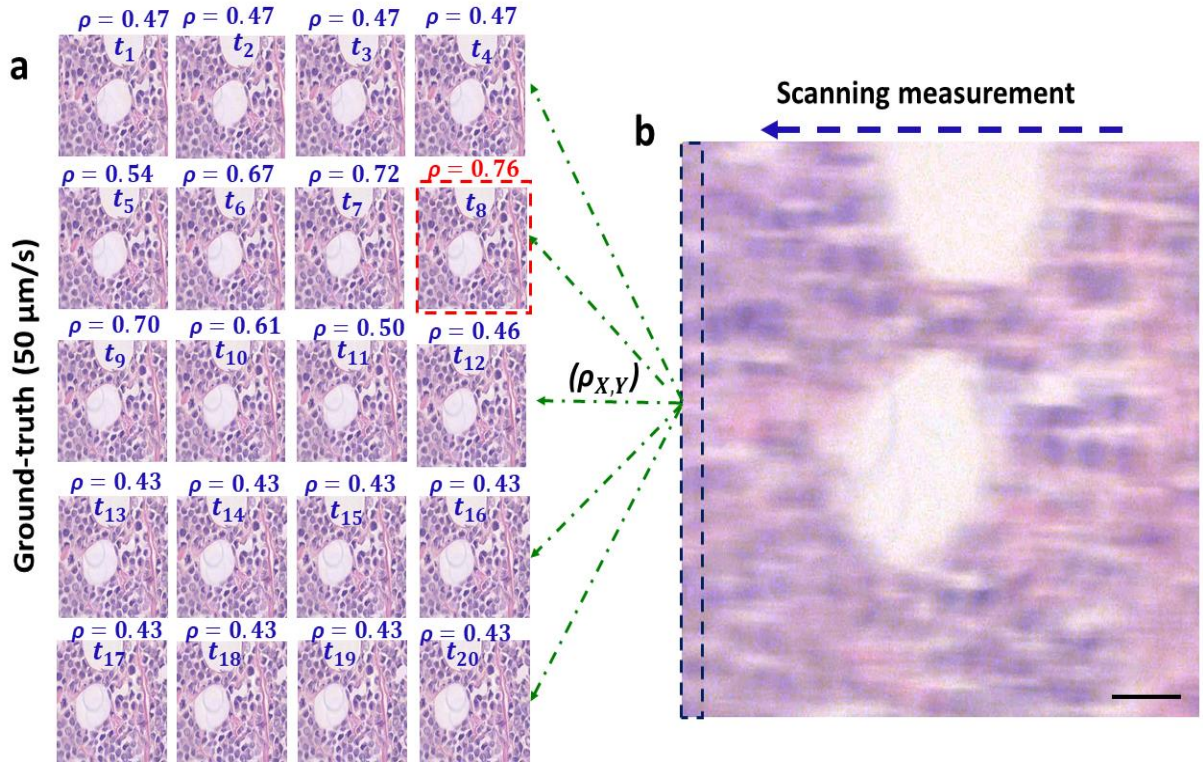

Figure 6.4 (a) Registration of images through maximum Pearson coefficient between sharp frames at 50 μm/s and **(b)** the blurry one at 10,000 μm/s**.** The scanning measurement is compared with each sharp contender (green dashed lines) and the resulting coefficient score is listed above each image. The best match is delineated in red, indicating the sharp image bearing the overall highest resemblance to the streaked measurement. The dashed rectangle at left edge of **(b)** outlines the extra margin of features contained in a blurry image (10 μm).

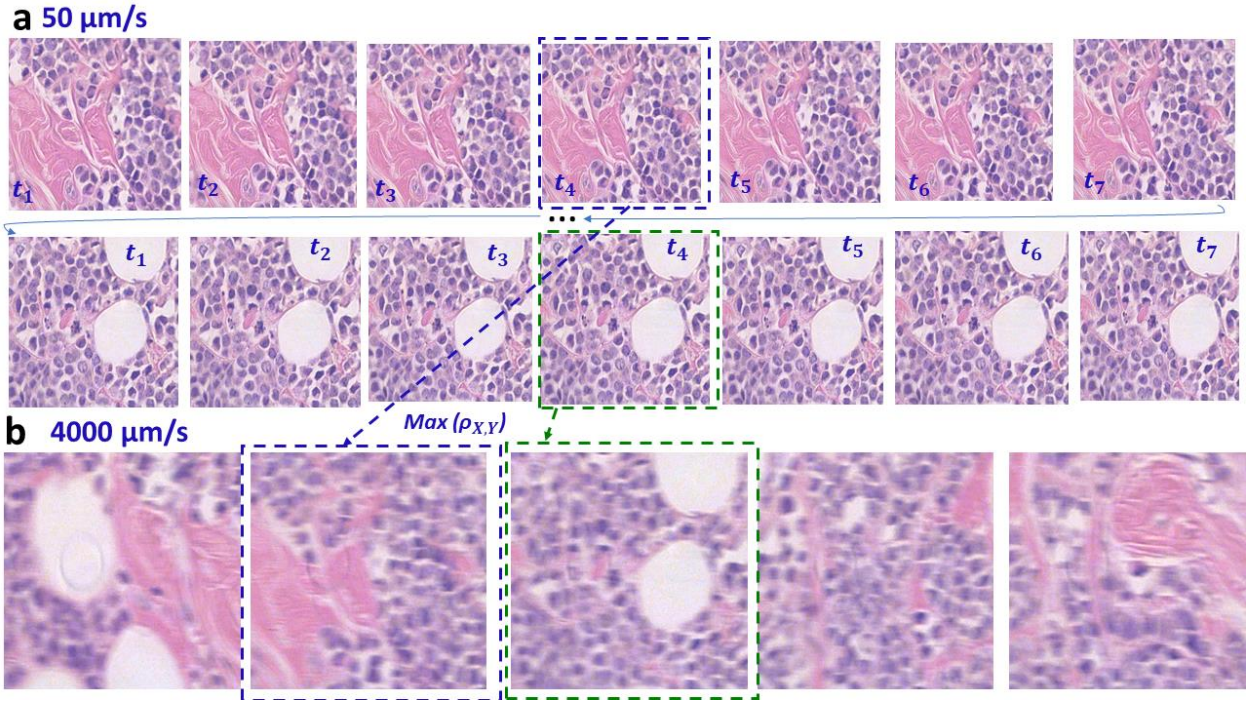

Figure 6.5 Registration of images through maximum Pearson coefficient between **(a)** sharp frames at 50 µm/s and **(b)** blurry ones at 4000 µm/s**.** The images are labelled with time stamps indicating a forward moving slow stage and best matches indicated with dashed lines.

6.3.6 Generative Adversarial Network (GAN)

Once the registered pairs were assembled, they were cropped and resized to dimensions of 256x256x1-3 (3 RGB color channels for brightfield and 1 channel for phase contrast images) for faster computation, with 1,050 images earmarked for training and 50 reserved for testing for both sample types. The architecture of the model consists of a generator U-net with eight encoding and decoding layers, and a four downchannel discriminator, all displayed in Figure 6.6. As shown in Figure 6.7, the network input is the motion-blurred image and the control is the slowly scanned, sharp image. Since the slide was scanned in a row-major style, the margin of additional field of view is always on the same side, which is likely to help the network to undo the motion distortion.

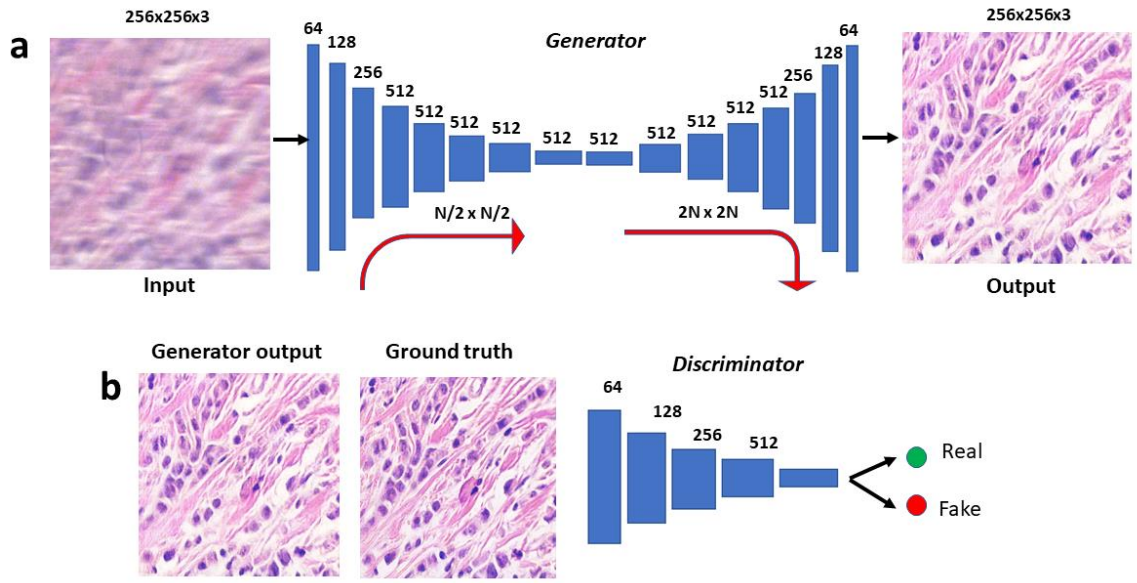

Figure 6.6 Model architecture. **(a)** The network consists of a generator model, **(b)** and a discriminator model, competing with one another. The generator endeavors to render a sharp image and trick the discriminator into judging it as authentic.

The GAN model was trained for over 200 epochs (Fig. 6.7c) until the loss function plateaued. Our results indicate that running the model on the training set produces nearly perfect restorations (Fig. 6.7d). The spatial power spectrum of the input image (Fig 6.7e) clearly shows a smaller range of higher spatial frequencies than that of the restored image (Fig 6.7f). Interestingly, the power spectrum of the input image has higher spatial frequencies along the vertical axis as a result of the smearing produced along the x-axis, whereas the power spectrum of the restored image is broader and more isotropic.

A separate model for repairing out-of-focus images was computed using 2420 training image pairs (taken from two different slides), with nearly half of the blurry set captured at four different levels of focus: -10 µm, -5 µm, +5 µm, and +10 µm. The rest of the parameters were the same as the models described above, with the ground truth images all being in perfect focus.

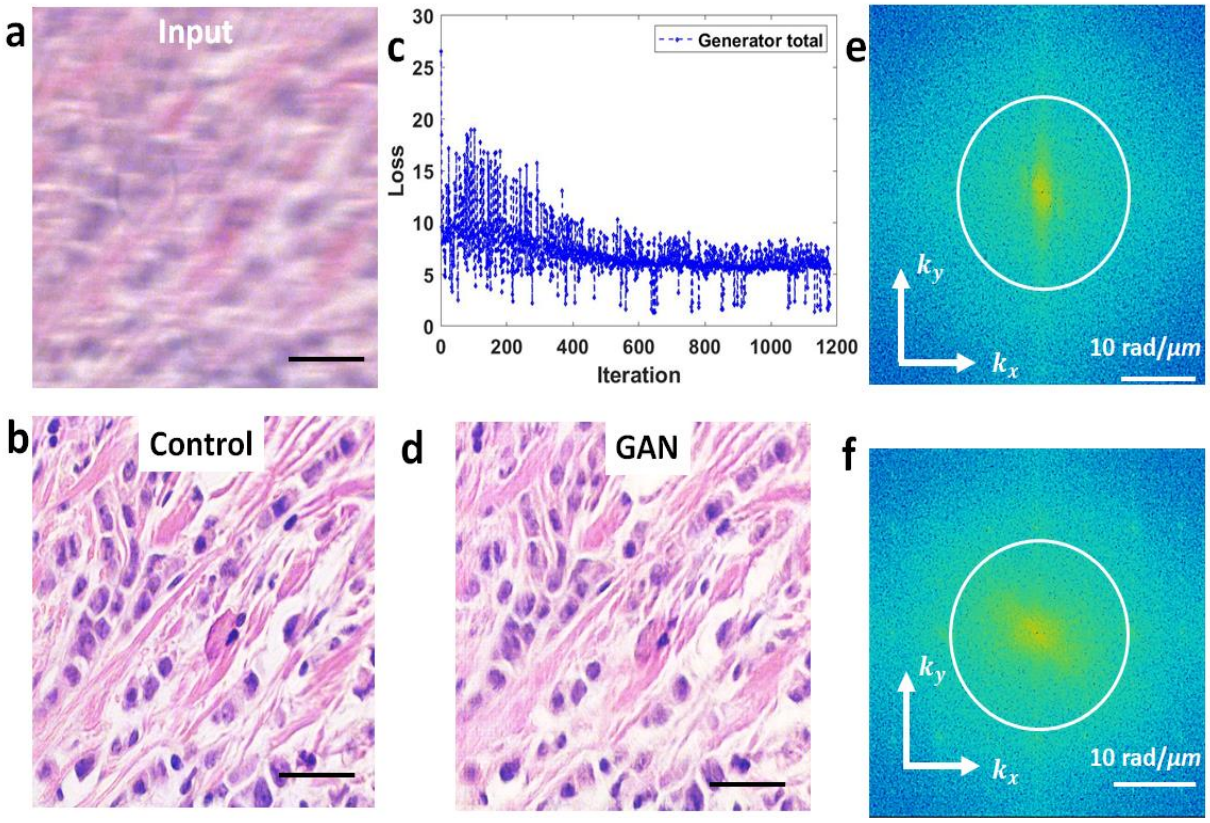

Figure 6.7 (a) Training example of the blurry input, **(b)** and control, **(c)** with the loss plot. **(d)** The generated result for a training instance. **(e)** The power spectra of the input and **f** of the result with a circle outlining the diffraction spot. Scale bar in **(a)**, **(b)**, and **(d) 25 µm.**

6.3.7 Performance Testing

Once the training was complete, the model was tested on 50 *unseen* images of the same slide of the dataset, and 160 images from slide corresponding to a different patient, as shown in Figures 6.8 and 6.9, respectively. 50 unseen blood smear images were also reconstructed, a sample of which is shown in Figure 6.10. The network does an effective job at restoring the high spatial frequencies of epithelial and stromal (fibrous) areas in biopsy samples, as compared to the line deconvolutions (Fig. 6.11). Since the cellular and fibrous areas are recovered with such high fidelity, the diagnostic information in the tissue images is maintained in full. In terms of numerical assessments, the first biopsy test sets achieved an average structural similarity index measure

(SSIM) of 0.82 and a mean peak signal-to-noise-ratio (PSNR) of 27 when calculated against their controls. For the same dataset, the deconvolution results gave inferior results of SSIM and PSRN of 0.71 and 26, respectively. The biopsy test set corresponding to a different patient achieved a similar average structural similarity index measure (SSIM) of 0.83 and a mean peak signal-to-noise-ratio (PSNR) of 26 when calculated against their controls, proving that the technique is applicable to samples entirely separate from of the training data (Fig 6.12). For the same dataset, the deconvolution results again gave inferior results of SSIM and PSRN of 0.77 and 25, respectively.

The same metrics were also calculated against stop-and-stare ground truths set. Figure 6.13 shows that there is no statistically significant difference between the values using the stop-and-stare and the 50 μm/s controls, indicating that the pairing strategy is valid.

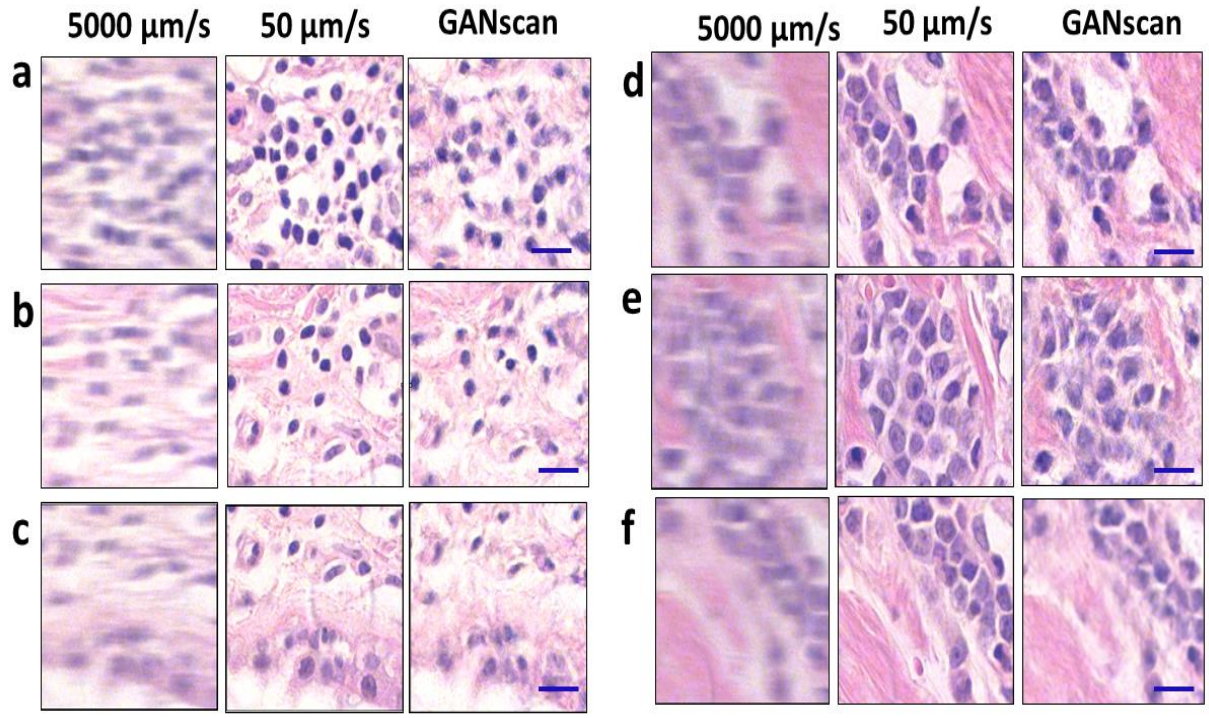

Figure 6.8 (a-f) Brightfield test set conversion of 5000 μm/s with control of 50 μm/s. Scale bar **5 μm.**

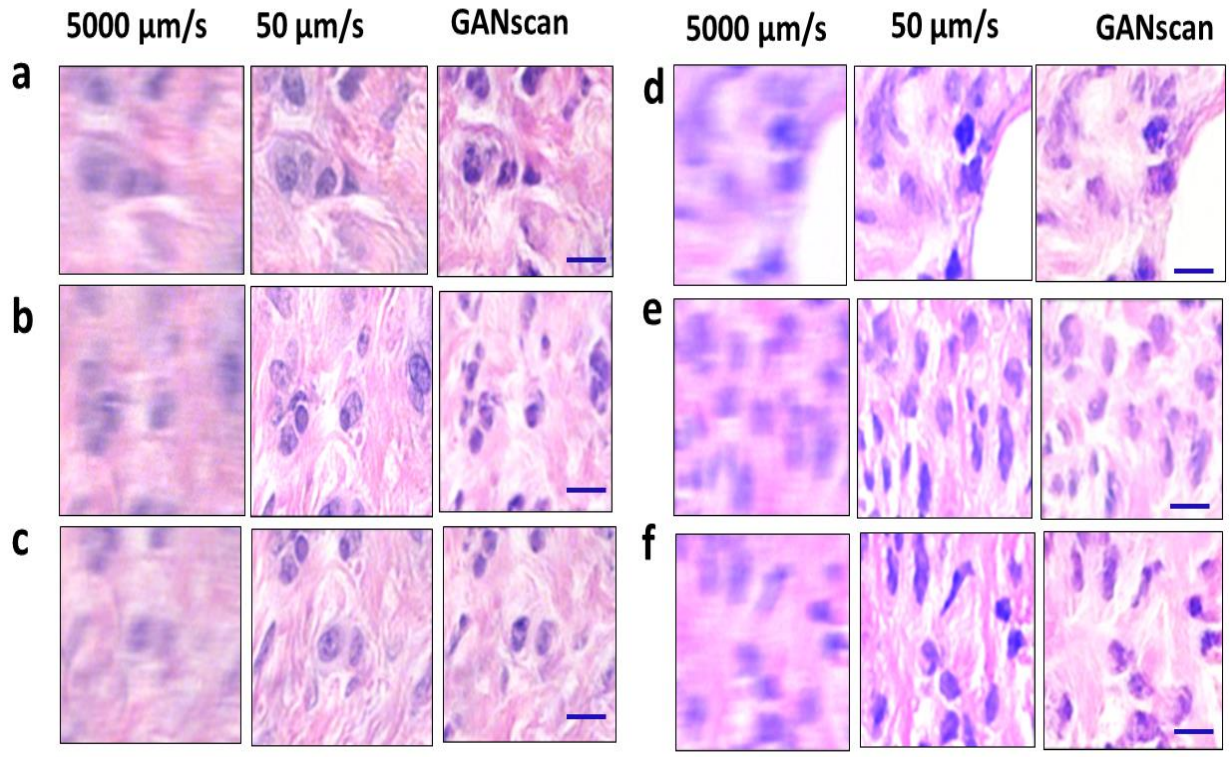

Figure 6.9 (a-c) and **(d-f)** Test set conversion of 5000 µm/s with control of 50 µm/s from two patients not included in the training dataset. Scale bar 5 µm.

Another way the results were evaluated was using line sections and plot profiles. Figure 6.14 shows a sample biopsy image in all three modes with their power spectra and line sections. The brightfield plot profiles show a strong overlap between the slow and reconstructed images, whereas the blurry image has a line profile that is smeared and diminished in intensity. In the frequency domain, the slow and reconstructed images show broader and higher frequencies as compared to the power spectrum of the blurry image, as expected.

The blood smear phase contrast images were reconstructed with similar success (Figure. 6.15). GANscan does an effective job at replicating a standard phase contrast image from a highly blurred input. Although some of the cell edges are not as smooth and round as in the control data, there rarely seems to be any hallucination of new cell boundaries. In this case, the test sets achieved

a slightly lower average structural similarity index measure (SSIM) of 0.73 and a mean peak signal-to-noise-ratio (PSNR) of 27 when calculated against their controls. For the same dataset, the deconvolution results gave inferior results of SSIM and PSRN of 0.66 and 26, respectively. A possible reason for the lower GANscan values with phase contrast microscopy may be that only the edges and halo of the blood cells contain any signal, causing a more severe blur in these images. Also, a single grayscale channel provides less information and context for the network to deal with.

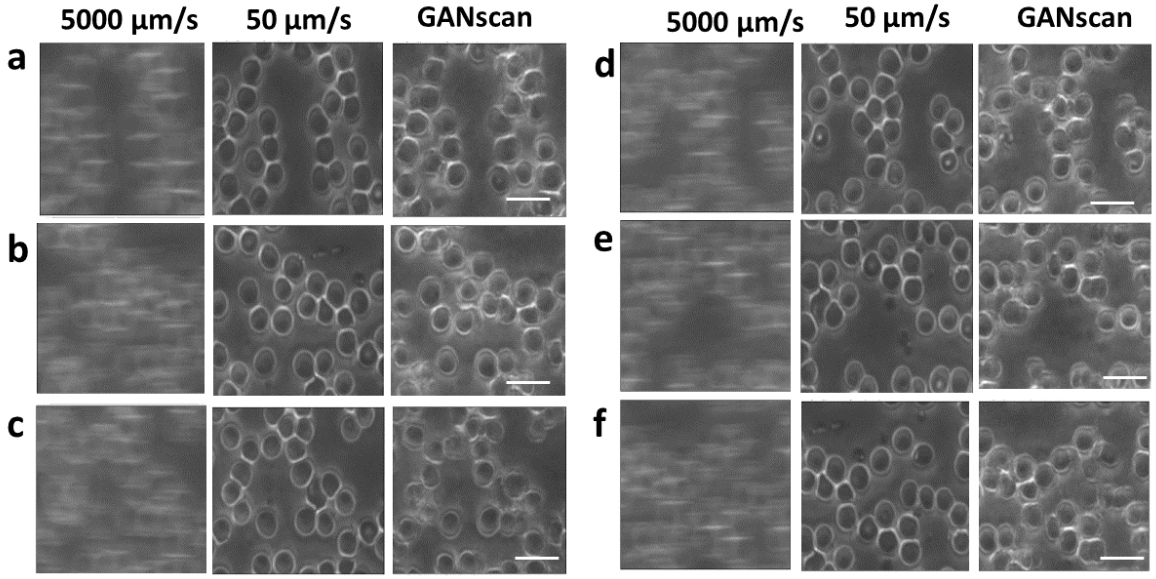

Figure 6.10 (a-f) Test set conversion of phase contrast unlabeled blood smear images moving at 5000 µm/s with control at 50 µm/s. Scale bar **5 µm.**

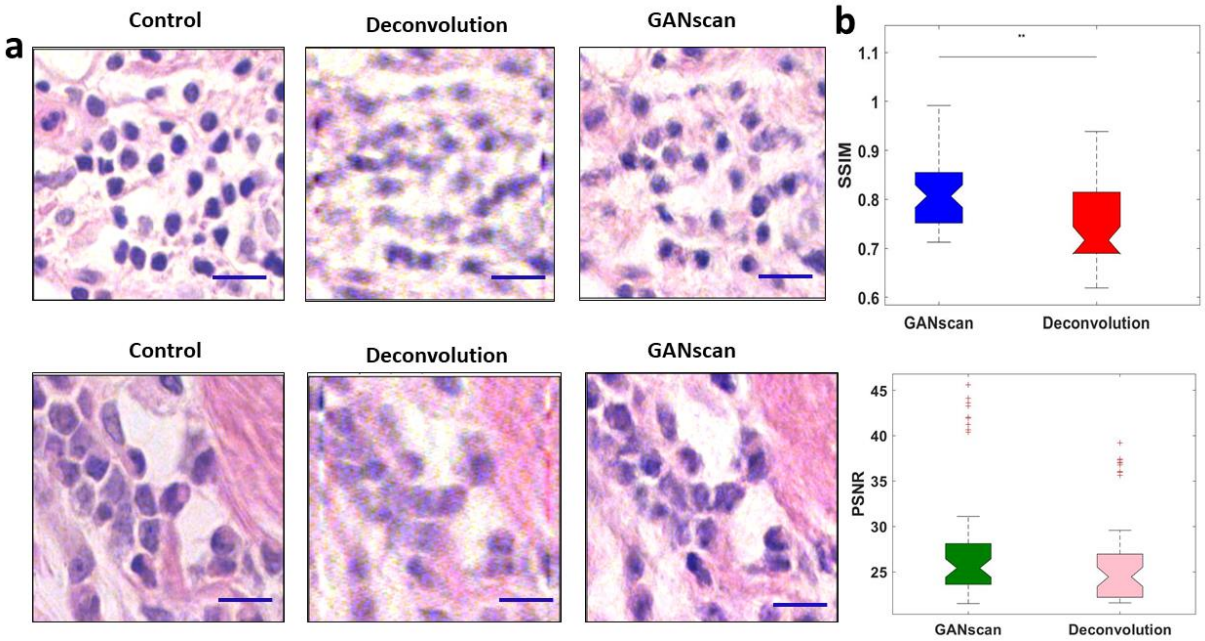

Figure 6.11 (a) Comparison of examples of deconvolved images with GANscan results, as well as **(b)** SSIM and PSNR values for the test sets. (**) indicates a p value<0.01. Scale bar **25 µm.**

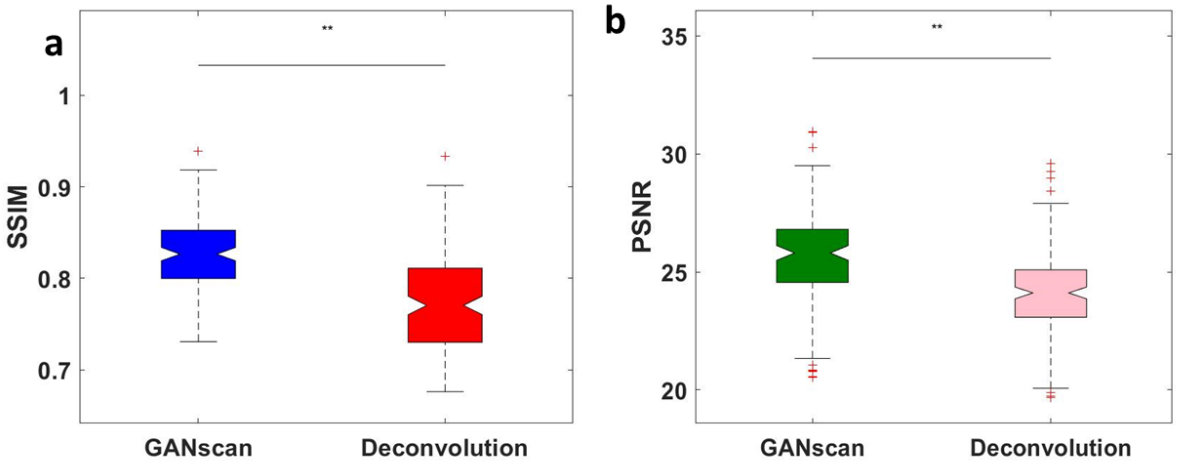

Figure 6.12 (a) SSIM and **(b)** PSNR comparisons between GANscan results and Deconvolution for the different patient test set. (**) indicates a p value<0.01.

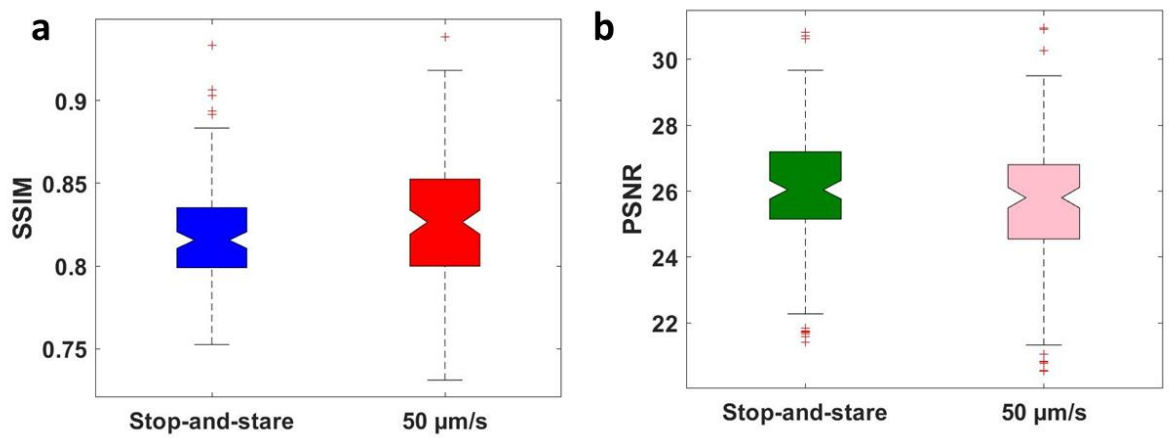

Figure 6.13 (a) SSIM values for the test sets with comparison of stop-and-stare ground truth with 50 µm/s ground truth. **(b)** SSIM values for the test sets with comparison of stop-and-stare ground truth with 50 µm/s ground truth.

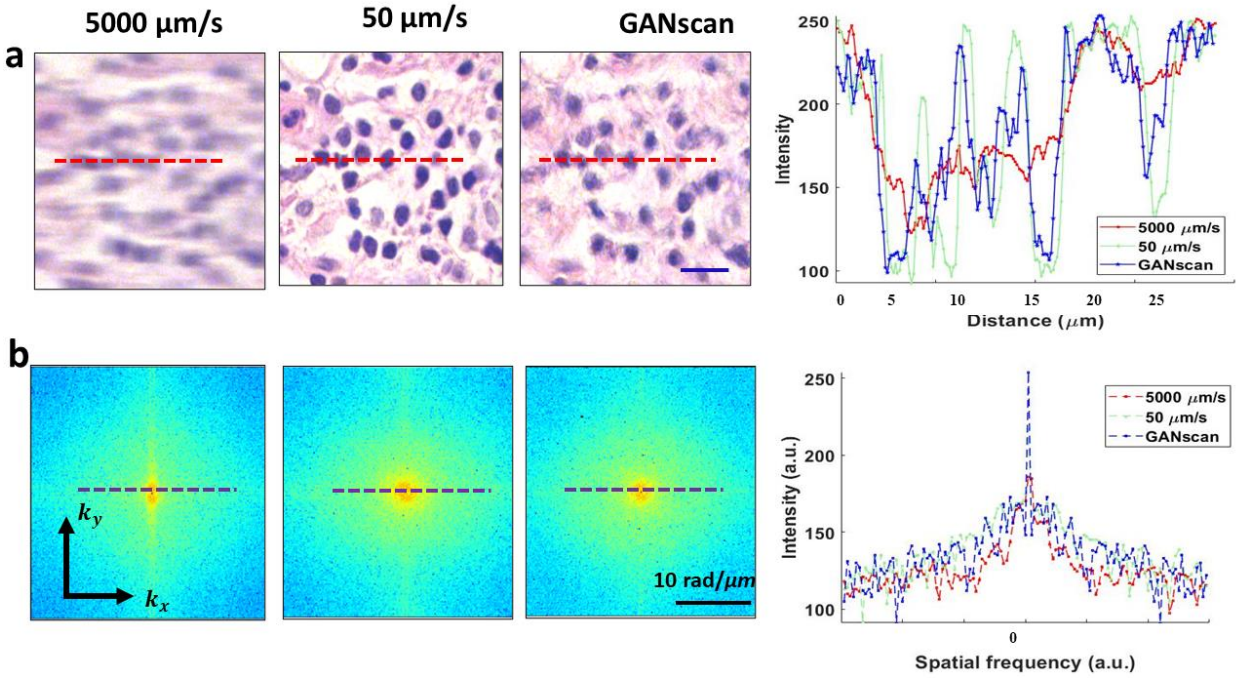

Figure 6.14 (a) Example test images in fast, slow and reconstructed versions with the intensity plot profiles of the red dash line through the image. **(b)** The power spectra of a with plot profile of purple dashed line in the images. Scale bar **5 µm.**

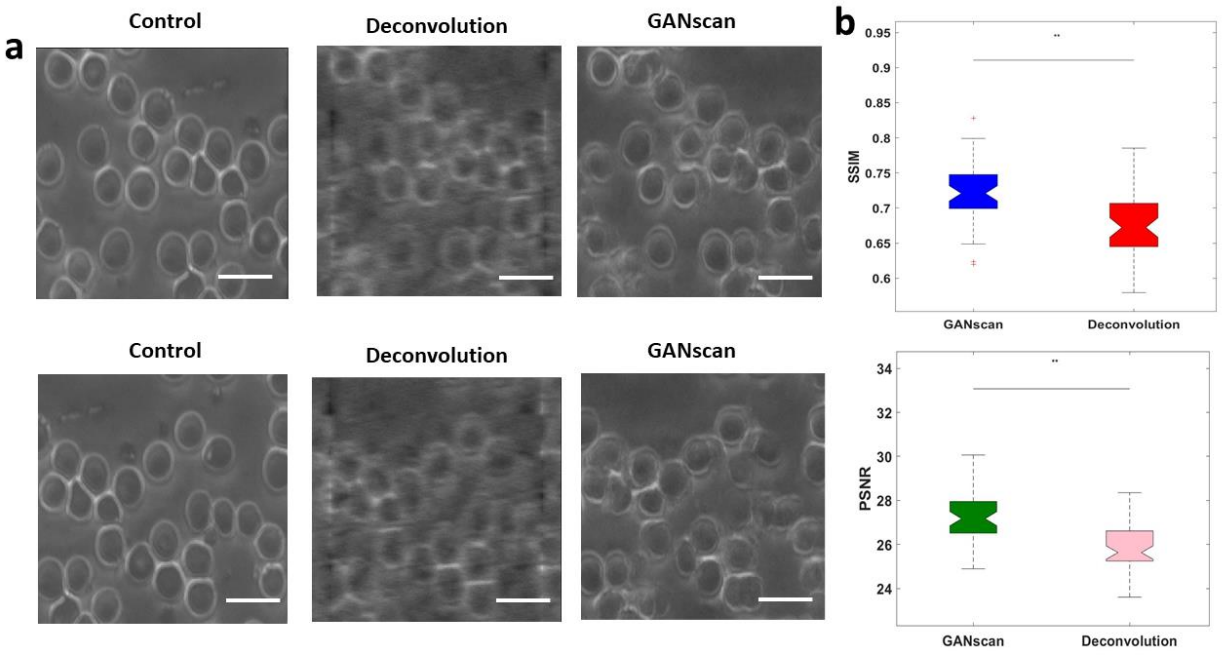

Figure 6. 15 (a) Comparison of examples of deconvolved phase contrast blood smear images with GANscan results, as well as **(b)** SSIM and PSNR values for the test sets. (**) indicates a p value<0.01. Scale bar **25 µm.**

Large mosaics of the motioned blurred biopsy images were also reconstructed (Fig. 6.16) by concatenating the images horizontally and vertically in their respective scanning order, producing a 7 x 15 stitch of roughly 3 mm x 1.5 mm in size. The difference in clarity is much less apparent with such a large FOV, but at a closer look it is evident there is significant improvement in the overall distinction of features. Stitches for 4,000 µm/s were also made for comparison (Fig. 6.17).

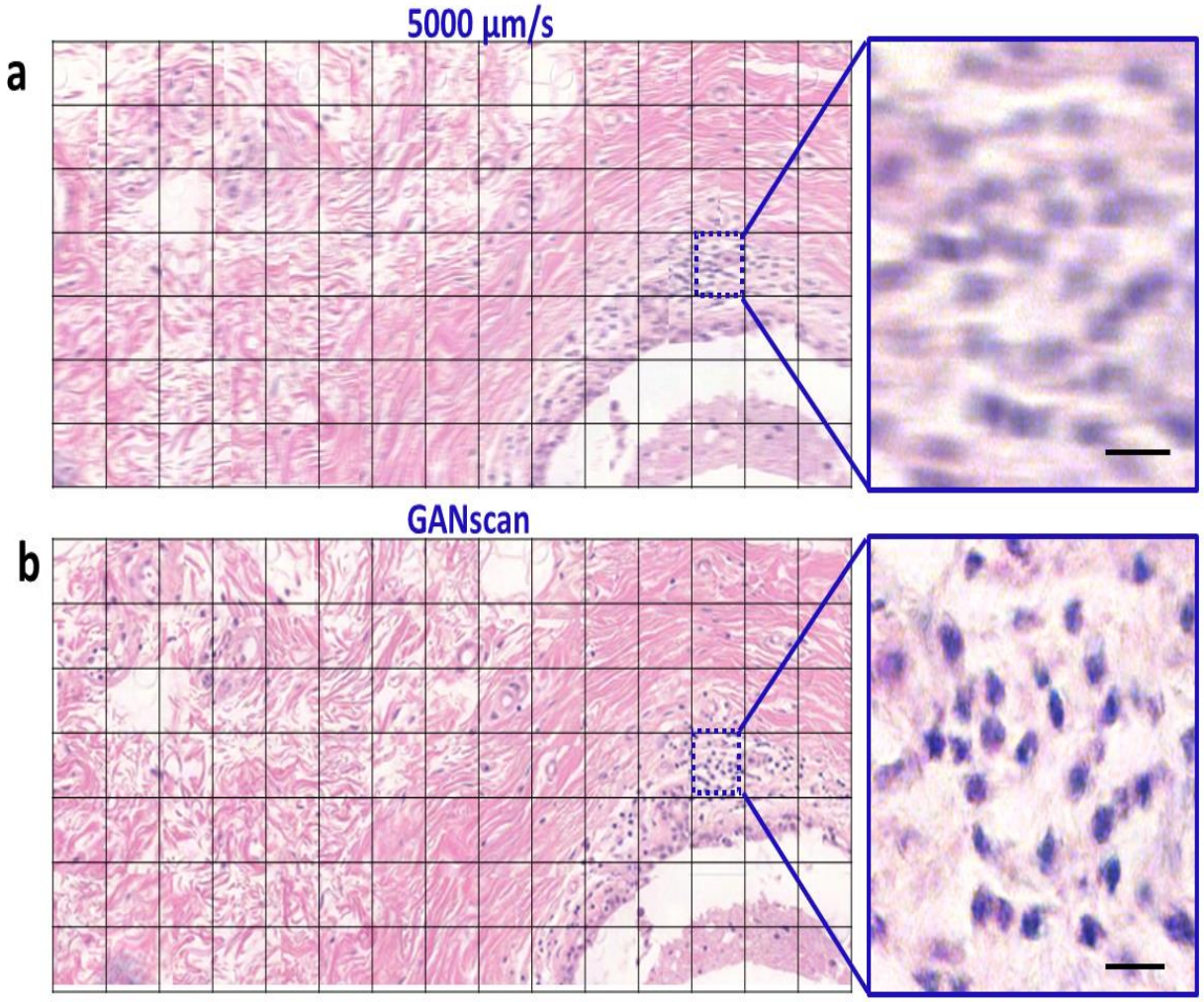

Figure 6.16 (a) Stitch of the motion blurred images, **(b)** as well as the reconstructed GANscan, showing a large area of a breast biopsy, with respective zoom-ins. Scale bar **5 µm.**

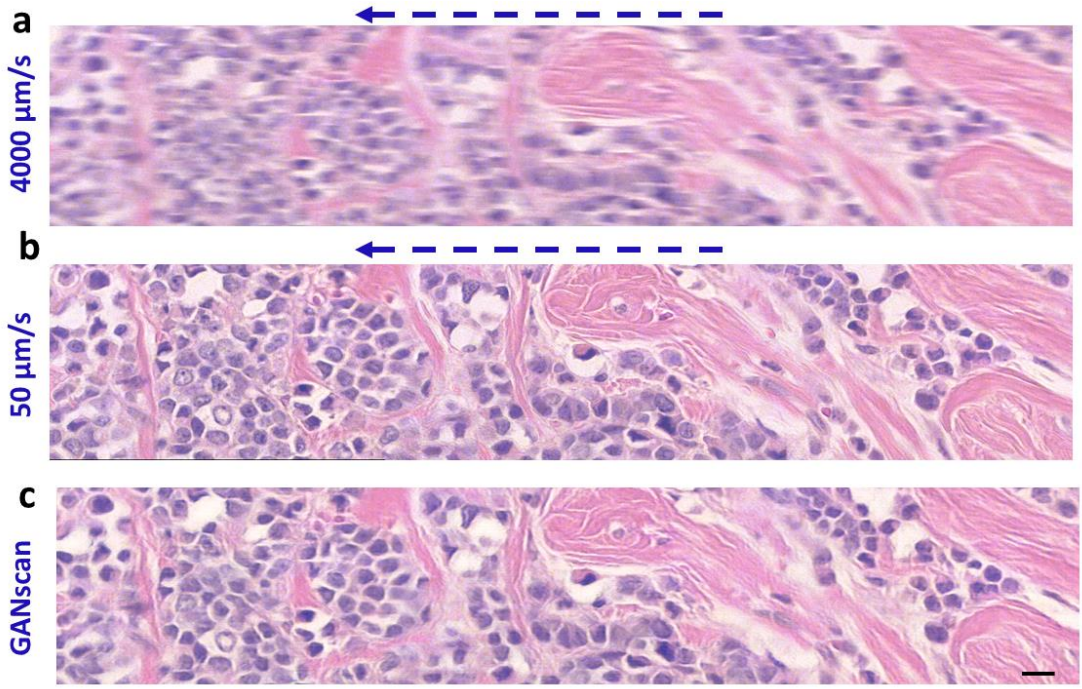

Figure 6.17 Example of a stitch with training data of **(a)** blurry, **(b)** sharp control and **c** reconstructed images. Scale bar **25 µm.**

6.3.8 Adjusting Out-of-focus Images

In order to assess the ability of GANscan to repair defocused images, the test set from a different patient was captured at 5000 µm/s at the plane of focus, but also at -10 µm, -5 µm, +5 µm, and +10 µm. This idea was inspired by previous work addressing autofocusing methods using GAN models[10]. Figure 6.18a shows a sample of images in all three modes at various levels of focus. They are not corresponding FOVs, as it is not possible to perfectly match different focal scans of blurry images. As it can be seen, the reconstructed images become progressively worse with increasing distance from the focal plane. Figure 6.18b shows the SSIM and PSNR curves for the whole test set with standard deviation margins from 30 instances (images) per level of focus. It is clear that the SSIM and PSNR start dipping as the image loses focus, from over 0.82 and 25, respectively, dropping to below 0.65 and 22 at the +/- 10 µm mark.

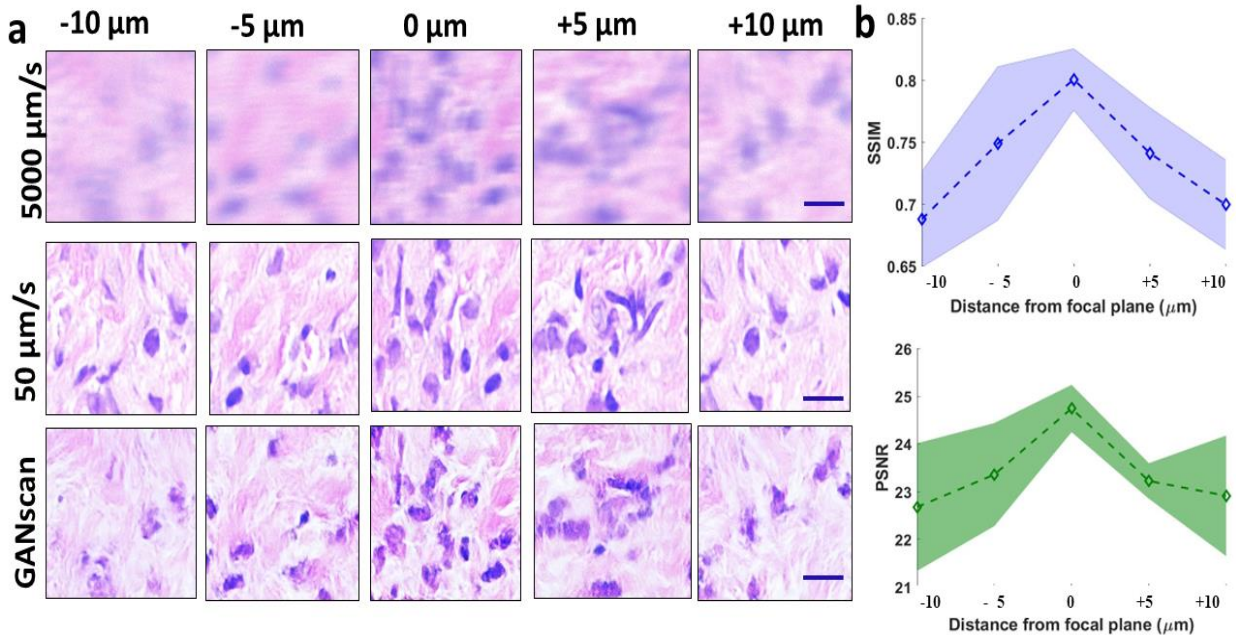

Figure 6.18 (a) example images from 5 different points of focus in fast, slow and reconstructed modes. **(b)** SSIM and PSRN values at the different points in the focal plane with shading representing the standard deviation across the 150-image (30 per plane) test set. Scale bar **5 µm.**

6.4 Discussion

I presented in this chapter a high-throughput imaging approach, GANscan, which employs continuous motion deblurring using labelled GAN reconstruction. Through both theoretical and experimental analysis, we have demonstrated the applicability of our method to brightfield and phase contrast microscopy on tissue slides. Our results indicate that GAN models provide, in combination with greater stage speeds, up to 30x faster acquisition rates than in conventional microscopy. This throughput is superior or on par with the state-of-the-art rapid scanning techniques, which in turn use nonstandard hardware. GANscan requires no specialized equipment and generates restored images with successfully removed motion blur. Of course, should a camera with a higher frame rate be used, the stage speed can be scaled up proportionally. Further, our

proposed deep learning deblurring method produces high-quality reconstructions which restores the high frequency portions of the tissue and cells, as opposed to deconvolution operations.

Such a methodology will not only provide a drastic benefit in the clinical setting for pathologists for diagnosis of cancer in biopsies and cell abnormalities in blood smears, but at the research level as well, including cell cultures of large dimensions. Future work should address achieving similar results with different microscope modalities, such as fluorescence and quantitative phase imaging.

References

1 Zarella, M. D. *et al.* A practical guide to whole slide imaging: a white paper from the digital pathology association. *Archives of pathology & laboratory medicine* **143**, 222-234 (2019).

2 Jahn, S. W., Plass, M. & Moinfar, F. Digital pathology: advantages, limitations and emerging perspectives. *Journal of Clinical Medicine* **9**, 3697 (2020).

3 Rivenson, Y. & Ozcan, A. Deep learning accelerates whole slide imaging for next-generation digital pathology applications. *Light: Science & Applications* **11**, 1-3 (2022).

4 Rajaganesan, S. *et al.* Comparative assessment of digital pathology systems for primary diagnosis. *Journal of Pathology Informatics* **12**, 25 (2021).

5 Gustafsson, M. G. Surpassing the lateral resolution limit by a factor of two using structured illumination microscopy. *Journal of microscopy* **198**, 82-87 (2000).

6 Rodenburg, J. M. & Faulkner, H. M. A phase retrieval algorithm for shifting illumination. *Applied physics letters* **85**, 4795-4797 (2004).

7 Zheng, G., Horstmeyer, R. & Yang, C. Wide-field, high-resolution Fourier ptychographic microscopy. *Nature photonics* **7**, 739-745 (2013).

8 Luo, W., Greenbaum, A., Zhang, Y. & Ozcan, A. Synthetic aperture-based on-chip microscopy. *Light: Science & Applications* **4**, e261-e261 (2015).

9 Tian, L., Li, X., Ramchandran, K. & Waller, L. Multiplexed coded illumination for Fourier Ptychography with an LED array microscope. *Biomedical optics express* **5**, 2376-2389 (2014).

10 Luo, Y., Huang, L., Rivenson, Y. & Ozcan, A. Single-shot autofocusing of microscopy images using deep learning. *ACS Photonics* **8**, 625-638 (2021).

11 Rivenson, Y. *et al.* Virtual histological staining of unlabelled tissue-autofluorescence images via deep learning. *Nature biomedical engineering* **3**, 466-477 (2019).

12 Fanous, M. J. & Popescu, G. GANscan: continuous scanning microscopy using deep learning deblurring. *Light: Science & Applications* **11**, 265, doi:10.1038/s41377-022-00952-z (2022).

13 Isola, P., Zhu, J.-Y., Zhou, T. & Efros, A. A. in *Proceedings of the IEEE conference on computer vision and pattern recognition.* 1125-1134.

14 Pang, Y., Lin, J., Qin, T. & Chen, Z. Image-to-image translation: Methods and applications. *IEEE Transactions on Multimedia* (2021).

15 Goodfellow, I. *et al.* Generative adversarial networks. *Communications of the ACM* **63**, 139-144 (2020).

16 Torre, L. A. *et al.* Global cancer statistics, 2012. *CA: a cancer journal for clinicians* **65**, 87-108 (2015).

17 Rahib, L. *et al.* Projecting cancer incidence and deaths to 2030: the unexpected burden of thyroid, liver, and pancreas cancers in the United States. *Cancer research* **74**, 2913-2921 (2014).

18 Lu, D. *et al.* Two-phase helical CT for pancreatic tumors: pancreatic versus hepatic phase enhancement of tumor, pancreas, and vascular structures. *Radiology* **199**, 697-701 (1996).

19 Rickes, S., Unkrodt, K., Neye, H., Ocran, K. & Wermke, W. Differentiation of pancreatic tumours by conventional ultrasound, unenhanced and echo-enhanced power Doppler sonography. *Scandinavian journal of gastroenterology* **37**, 1313-1320 (2002).
20 Diehl, S. J. *et al.* MR imaging of pancreatic lesions: comparison of manganese-DPDP and gadolinium chelate. *Investigative radiology* **34**, 589 (1999).
21 Sendler, A. *et al.* Preoperative evaluation of pancreatic masses with positron emission tomography using 18 F-fluorodeoxyglucose: diagnostic limitations. *World journal of surgery* **24**, 1121-1129 (2000).
22 Chang, K. J., Nguyen, P., Erickson, R. A., Durbin, T. E. & Katz, K. D. The clinical utility of endoscopic ultrasound–guided fine-needle aspiration in the diagnosisand staging of pancreatic carcinoma. *Gastrointestinal endoscopy* **45**, 387-393 (1997).
23 Vander Noot III, M. R. *et al.* Diagnosis of gastrointestinal tract lesions by endoscopic ultrasound-guided fine-needle aspiration biopsy. *Cancer Cytopathology: Interdisciplinary International Journal of the American Cancer Society* **102**, 157-163 (2004).
24 Brand, B. *et al.* Endoscopic ultrasound for differential diagnosis of focal pancreatic lesions, confirmed by surgery. *Scandinavian journal of gastroenterology* **35**, 1221-1228 (2000).
25 Jain, R. K. *et al.* Atypical ductal hyperplasia: interobserver and intraobserver variability. *Modern Pathology* **24**, 917 (2011).
26 Neuzillet, C. *et al.* State of the art and future directions of pancreatic ductal adenocarcinoma therapy. *Pharmacology & therapeutics* **155**, 80-104 (2015).
27 Drifka, C. R. *et al.* Highly aligned stromal collagen is a negative prognostic factor following pancreatic ductal adenocarcinoma resection. *Oncotarget* **7**, 76197 (2016).
28 Yamada, K. M. & Cukierman, E. Modeling tissue morphogenesis and cancer in 3D. *Cell* **130**, 601-610 (2007).
29 Richter, A. *et al.* Long-term results of partial pancreaticoduodenectomy for ductal adenocarcinoma of the pancreatic head: 25-year experience. *World journal of surgery* **27**, 324-329 (2003).
30 Sinn, M. *et al.* Does long-term survival in patients with pancreatic cancer really exist?—Results from the CONKO-001 study. *Journal of surgical oncology* **108**, 398-402 (2013).
31 Rhim, A. D. *et al.* EMT and dissemination precede pancreatic tumor formation. *Cell* **148**, 349-361 (2012).
32 Blackford, A. *et al.* SMAD4 gene mutations are associated with poor prognosis in pancreatic cancer. *Clinical cancer research* **15**, 4674-4679 (2009).
33 Pandol, S., Edderkaoui, M., Gukovsky, I., Lugea, A. & Gukovskaya, A. Desmoplasia of pancreatic ductal adenocarcinoma. *Clinical Gastroenterology and Hepatology* **7**, S44-S47 (2009).
34 Bever, K. M. *et al.* The prognostic value of stroma in pancreatic cancer in patients receiving adjuvant therapy. *Hpb* **17**, 292-298 (2015).
35 Provenzano, P. P. *et al.* Collagen reorganization at the tumor-stromal interface facilitates local invasion. *BMC medicine* **4**, 38 (2006).
36 Nadiarnykh, O., LaComb, R. B., Brewer, M. A. & Campagnola, P. J. Alterations of the extracellular matrix in ovarian cancer studied by Second Harmonic Generation imaging microscopy. *BMC cancer* **10**, 94 (2010).

37 Hanley, C. J. *et al.* A subset of myofibroblastic cancer-associated fibroblasts regulate collagen fiber elongation, which is prognostic in multiple cancers. *Oncotarget* **7**, 6159 (2016).
38 Levental, K. R. *et al.* Matrix crosslinking forces tumor progression by enhancing integrin signaling. *Cell* **139**, 891-906 (2009).
39 Tung, J. C. *et al.* Tumor mechanics and metabolic dysfunction. *Free Radical Biology and Medicine* **79**, 269-280 (2015).
40 Drifka, C. R. *et al.* Periductal stromal collagen topology of pancreatic ductal adenocarcinoma differs from that of normal and chronic pancreatitis. *Modern Pathology* **28**, 1470 (2015).
41 Campagnola, P. J. & Loew, L. M. Second-harmonic imaging microscopy for visualizing biomolecular arrays in cells, tissues and organisms. *Nature biotechnology* **21**, 1356 (2003).
42 Oldenbourg, R. & Mei, G. New polarized light microscope with precision universal compensator. *Journal of microscopy* **180**, 140-147 (1995).
43 Keikhosravi, A. *et al.* Quantification of collagen organization in histopathology samples using liquid crystal based polarization microscopy. *Biomedical optics express* **8**, 4243-4256 (2017).
44 Wang, Z. *et al.* Spatial light interference microscopy (SLIM). *Optics express* **19**, 1016-1026 (2011).
45 Majeed, H., Okoro, C., Kajdacsy-Balla, A., Toussaint, J. K. C. & Popescu, G. Quantifying collagen fiber orientation in breast cancer using quantitative phase imaging. *Journal of Biomedical Optics* **22**, 046004-046004, doi:10.1117/1.JBO.22.4.046004 (2017).
46 Majeed, H. *et al.* Breast cancer diagnosis using spatial light interference microscopy. *Journal of biomedical optics* **20**, 111210 (2015).
47 Popescu, G. *Quantitative phase imaging of cells and tissues*. (McGraw Hill Professional, 2011).
48 Bredfeldt, J. S. *et al.* Computational segmentation of collagen fibers from second-harmonic generation images of breast cancer. *Journal of biomedical optics* **19**, 016007 (2014).
49 Hu, C. & Popescu, G. Quantitative Phase Imaging (QPI) in Neuroscience. *IEEE Journal of Selected Topics in Quantum Electronics* **25**, 1-9, doi:10.1109/JSTQE.2018.2869613 (2019).
50 Lee, M. *et al.* Label-free optical quantification of structural alterations in Alzheimer's disease. *Sci Rep* **6**, 31034, doi:10.1038/srep31034 (2016).
51 Wang, P., Bista, R., Bhargava, R., Brand, R. E. & Liu, Y. Spatial-domain low-coherence quantitative phase microscopy for cancer diagnosis. *Optics letters* **35**, 2840-2842 (2010).
52 Nguyen, T. H. *et al.* Automatic Gleason grading of prostate cancer using quantitative phase imaging and machine learning. *Journal of biomedical optics* **22**, 036015 (2017).
53 Majeed, H. *et al.* Quantitative phase imaging for medical diagnosis. *Journal of biophotonics* **10**, 177-205 (2017).
54 Sridharan, S., Macias, V., Tangella, K., Kajdacsy-Balla, A. & Popescu, G. Prediction of prostate cancer recurrence using quantitative phase imaging. *Scientific reports* **5**, 9976 (2015).

55 Takabayashi, M., Majeed, H., Kajdacsy-Balla, A. & Popescu, G. Disorder strength measured by quantitative phase imaging as intrinsic cancer marker in fixed tissue biopsies. *PloS one* **13**, e0194320 (2018).
56 Hu, C. *et al.* Imaging collagen properties in the uterosacral ligaments of women with pelvic organ prolapse using spatial light interference microscopy (SLIM). *Frontiers in Physics* **7**, 72 (2019).
57 Park, H. S., Rinehart, M., Walzer, K. A., Chi, J. T. A. & Wax, A. Automated Detection of P. falciparum Using Machine Learning Algorithms with Quantitative Phase Images of Unstained Cells. *Plos One* **11**, doi:ARTN e0163045
58 Majeed, H. *et al.* Quantitative histopathology of stained tissues using color spatial light interference microscopy (cSLIM). *Scientific reports* **9** (2019).
59 Popescu, G. *et al.* Optical imaging of cell mass and growth dynamics. *Am J Physiol Cell Physiol* **295**, C538-544 (2008).
60 Kandel, M. E. *et al.* Label-free tissue scanner for colorectal cancer screening. *Journal of biomedical optics* **22**, 066016 (2017).
61 Mukaka, M. M. A guide to appropriate use of correlation coefficient in medical research. *Malawi Medical Journal* **24**, 69-71 (2012).
62 Fields, R. D. White matter matters. *Scientific American* **298**, 54-61 (2008).
63 Yakovlev, P. The myelogenetic cycles of regional maturation of the brain. *Regional development of the brain in early life*, 3-70 (1967).
64 Deoni, S., Dean III, D., Joelson, S., O'Regan, J. & Schneider, N. Early nutrition influences developmental myelination and cognition in infants and young children. *Neuroimage* **178**, 649-659 (2018).
65 Bartzokis, G. Age-related myelin breakdown: a developmental model of cognitive decline and Alzheimer's disease. *Neurobiology of aging* **25**, 5-18 (2004).
66 Bartzokis, G. *et al.* Apolipoprotein E affects both myelin breakdown and cognition: implications for age-related trajectories of decline into dementia. *Biological psychiatry* **62**, 1380-1387 (2007).
67 Morrison, J. H. & Baxter, M. G. The ageing cortical synapse: hallmarks and implications for cognitive decline. *Nature Reviews Neuroscience* **13**, 240 (2012).
68 Ábrahám, H. *et al.* Myelination in the human hippocampal formation from midgestation to adulthood. *International Journal of Developmental Neuroscience* **28**, 401-410 (2010).
69 Nakagawa, H. *et al.* Normal myelination of anatomic nerve fiber bundles: MR analysis. *American journal of neuroradiology* **19**, 1129-1136 (1998).
70 Radlowski, E. C. *et al.* A neonatal piglet model for investigating brain and cognitive development in small for gestational age human infants. *PLoS One* **9**, e91951 (2014).
71 Ozanne, S. E., Fernandez-Twinn, D. & Hales, C. N. in *Seminars in perinatology*. 81-87 (Elsevier).
72 Geva, R., Eshel, R., Leitner, Y., Valevski, A. F. & Harel, S. Neuropsychological outcome of children with intrauterine growth restriction: a 9-year prospective study. *Pediatrics* **118**, 91-100 (2006).
73 Eikenes, L. *et al.* Being born small for gestational age reduces white matter integrity in adulthood: a prospective cohort study. *Pediatric research* **72**, 649 (2012).
74 Strauss, R. S. Adult functional outcome of those born small for gestational age: twenty-six–year follow-up of the 1970 British birth cohort. *Jama* **283**, 625-632 (2000).

75 Larroque, B., Bertrais, S., Czernichow, P. & Léger, J. School difficulties in 20-year-olds who were born small for gestational age at term in a regional cohort study. *Pediatrics* **108**, 111-115 (2001).
76 Eide, M. *et al.* Degree of fetal growth restriction associated with schizophrenia risk in a national cohort. *Psychological medicine* **43**, 2057-2066 (2013).
77 Ong, K. K. Catch-up growth in small for gestational age babies: good or bad? *Current Opinion in Endocrinology, Diabetes and Obesity* **14**, 30-34 (2007).
78 Blössner, M. & Villar, J. Levels and patterns of intrauterine growth retardation in developing countries. *European journal of clinical nutrition* **52**, S5-15 (1998).
79 Mathews, T. & MacDorman, M. F. Infant mortality statistics from the 2006 period linked birth/infant death data set. (2010).
80 Salthouse, T. Luxol fast blue ARN: a new solvent azo dye with improved staining qualities for myelin and phospholipids. *Stain technology* **37**, 313-316 (1962).
81 Stueber, C. *et al.* Myelin and iron concentration in the human brain: a quantitative study of MRI contrast. *Neuroimage* **93**, 95-106 (2014).
82 Wilhelm, M. J. *et al.* Direct magnetic resonance detection of myelin and prospects for quantitative imaging of myelin density. *Proceedings of the National Academy of Sciences* **109**, 9605-9610 (2012).
83 Laule, C. *et al.* Myelin water imaging of multiple sclerosis at 7 T: correlations with histopathology. *Neuroimage* **40**, 1575-1580 (2008).
84 Li, Y., Fanous, M. J., Kilian, K. A. & Popescu, G. Quantitative phase imaging reveals matrix stiffness-dependent growth and migration of cancer cells. *Scientific reports* **9**, 248 (2019).
85 Park, Y., Depeursinge, C. & Popescu, G. Quantitative phase imaging in biomedicine. *Nature Photonics* **12**, 578-589, doi:10.1038/s41566-018-0253-x (2018).
86 Nguyen, T. H., Kandel, M. E., Rubessa, M., Wheeler, M. B. & Popescu, G. Gradient light interference microscopy for 3D imaging of unlabeled specimens. *Nature communications* **8**, 210 (2017).
87 Kandel, M. E. *et al.* Epi-illumination gradient light interference microscopy for imaging opaque structures. *Nature communications* **10**, 1-9 (2019).
88 Kandel, M. E., Fanous, M., Best-Popescu, C. & Popescu, G. Real-time halo correction in phase contrast imaging. *Biomedical optics express* **9**, 623-635 (2018).
89 Popescu, G. *et al.* Optical imaging of cell mass and growth dynamics. *American Journal of Physiology-Cell Physiology* **295**, C538-C544 (2008).
90 Ding, H., Nguyen, F., Boppart, S. A. & Popescu, G. Optical properties of tissues quantified by Fourier-transform light scattering. *Optics letters* **34**, 1372-1374 (2009).
91 Lue, N. *et al.* Live cell refractometry using microfluidic devices. *Optics letters* **31**, 2759-2761 (2006).
92 Bhaduri, B., Pham, H., Mir, M. & Popescu, G. Diffraction phase microscopy with white light. *Optics letters* **37**, 1094-1096 (2012).
93 Bhaduri, B., Tangella, K. & Popescu, G. Fourier phase microscopy with white light. *Biomedical optics express* **4**, 1434-1441 (2013).
94 Wang, Z. *et al.* Spatial light interference tomography (SLIT). *Optics express* **19**, 19907-19918 (2011).
95 Wang, Z., Tangella, K., Balla, A. & Popescu, G. Tissue refractive index as marker of disease. *Journal of Biomedical Optics* **16**, 116017 (2011).

96 Chung, K. & Deisseroth, K. CLARITY for mapping the nervous system. *Nat Methods* **10**, 508 (2013).
97 Caputo, M. P. *et al.* Hydrolyzed fat formula incrased brain white matter in small for gestational age and appropriate for gestational age neonatal piglets. *Frontiers in Pediatrics Neonatology* **(in press)** (2019).
98 Rytych, J. L. *et al.* Early life iron deficiency impairs spatial cognition in neonatal piglets. *The Journal of nutrition* **142**, 2050-2056 (2012).
99 Council, N. R. *Nutrient requirements of swine*. (National Academies Press, 2012).
100 Blakemore, W. & Harding, J. Ultrastructural observations on the spinal cords of piglets affected with congenital tremor type AIV. *Research in veterinary science* **17**, 248-255 (1974).
101 Tomer, R., Ye, L., Hsueh, B. & Deisseroth, K. Advanced CLARITY for rapid and high-resolution imaging of intact tissues. *Nature protocols* **9**, 1682 (2014).
102 Nguyen, T. H., Edwards, C., Goddard, L. L. & Popescu, G. Quantitative phase imaging with partially coherent illumination. *Optics letters* **39**, 5511-5514 (2014).
103 Sridharan, S. *et al.* Prediction of prostate cancer recurrence using quantitative phase imaging: Validation on a general population. *Scientific reports* **6**, 33818 (2016).
104 Ferraro, P. *et al.* Quantitative phase-contrast microscopy by a lateral shear approach to digital holographic image reconstruction. *Optics letters* **31**, 1405-1407 (2006).
105 Eldridge, W. J. *et al.* Shear modulus measurement by quantitative phase imaging and correlation with atomic force microscopy. *Biophysical journal* **117**, 696-705 (2019).
106 Park, H. S. *et al.* Quantitative phase imaging of erythrocytes under microfluidic constriction in a high refractive index medium reveals water content changes. *Microsystems & nanoengineering* **5**, 1-9 (2019).
107 Eldridge, W. J., Hoballah, J. & Wax, A. Molecular and biophysical analysis of apoptosis using a combined quantitative phase imaging and fluorescence resonance energy transfer microscope. *Journal of biophotonics* **11**, e201800126 (2018).
108 Park, H. S., Ceballos, S., Eldridge, W. J. & Wax, A. Invited Article: Digital refocusing in quantitative phase imaging for flowing red blood cells. *APL photonics* **3**, 110802 (2018).
109 Casteleiro Costa, P., Ledwig, P., Bergquist, A., Kurtzberg, J. & Robles, F. E. Noninvasive white blood cell quantification in umbilical cord blood collection bags with quantitative oblique back-illumination microscopy. *Transfusion* **60**, 588-597 (2020).
110 Ledwig, P. & Robles, F. E. Quantitative 3D refractive index tomography of opaque samples in epi-mode. *Optica* **8**, 6-14 (2021).
111 Robles, F. E. in *Label-free Biomedical Imaging and Sensing (LBIS) 2020.* 112511Y (International Society for Optics and Photonics).
112 Kemper, B., Vollmer, A., von Bally, G., Rommel, C. E. & Schnekenburger, J. Simplified approach for quantitative digital holographic phase contrast imaging of living cells. *Journal of biomedical optics* **16**, 026014 (2011).
113 Di Caprio, G. *et al.* Quantitative label-free animal sperm imaging by means of digital holographic microscopy. *IEEE Journal of Selected Topics in Quantum Electronics* **16**, 833-840 (2010).
114 Marquet, P. *et al.* Digital holographic microscopy: a noninvasive contrast imaging technique allowing quantitative visualization of living cells with subwavelength axial accuracy. *Optics letters* **30**, 468-470 (2005).

115 Lee, K. *et al.* Quantitative phase imaging techniques for the study of cell pathophysiology: from principles to applications. *Sensors* **13**, 4170-4191 (2013).
116 Jin, D., Zhou, R., Yaqoob, Z. & So, P. T. Tomographic phase microscopy: principles and applications in bioimaging. *JOSA B* **34**, B64-B77 (2017).
117 Fanous, M. *et al.* Quantifying myelin content in brain tissue using color Spatial Light Interference Microscopy (cSLIM). *PLOS ONE* **15**, e0241084, doi:10.1371/journal.pone.0241084 (2020).
118 Caputo, M. P. *et al.* Hydrolyzed Fat Formula Increases Brain White Matter in Small for Gestational Age and Appropriate for Gestational Age Neonatal Piglets. *Frontiers in pediatrics* **8**, 32 (2020).
119 Rivenson, Y. *et al.* PhaseStain: the digital staining of label-free quantitative phase microscopy images using deep learning. *Light: Science & Applications* **8**, 23 (2019).
120 de Haan, K. *et al.* Automated screening of sickle cells using a smartphone-based microscope and deep learning. *NPJ Digital Medicine* **3**, 1-9 (2020).
121 Subramanian, S. *et al.* MedICaT: A Dataset of Medical Images, Captions, and Textual References. *arXiv preprint arXiv:2010.06000* (2020).
122 MacAvaney, S., Cohan, A., Goharian, N. & Filice, R. in *European Conference on Information Retrieval.* 238-245 (Springer).
123 Kohlberger, T. *et al.* Whole-slide image focus quality: Automatic assessment and impact on ai cancer detection. *Journal of pathology informatics* **10** (2019).
124 Krause, J. *et al.* Grader variability and the importance of reference standards for evaluating machine learning models for diabetic retinopathy. *Ophthalmology* **125**, 1264-1272 (2018).
125 Poplin, R. *et al.* Predicting cardiovascular risk factors from retinal fundus photographs using deep learning. arXiv 2017. *arXiv preprint arXiv:1708.09843*.
126 Liu, Y. *et al.* Detecting cancer metastases on gigapixel pathology images. *arXiv preprint arXiv:1703.02442* (2017).
127 Zhang, J. K., He, Y. R., Sobh, N. & Popescu, G. Label-free colorectal cancer screening using deep learning and spatial light interference microscopy (SLIM). *APL Photonics* **5**, 040805, doi:10.1063/5.0004723 (2020).
128 Hou, L. *et al.* in *Proceedings of the ieee conference on computer vision and pattern recognition.* 2424-2433.
129 Kandel, M. E. *et al.* Phase Imaging with Computational Specificity (PICS) for measuring dry mass changes in sub-cellular compartments. *Nature communications* **11**, 1-10 (2020).
130 Goswami, N. *et al.* in *Quantitative Phase Imaging VII.* 1165313 (SPIE).
131 Chollet, F. in *Proceedings of the IEEE conference on computer vision and pattern recognition.* 1251-1258.
132 Sandler, M., Howard, A., Zhu, M., Zhmoginov, A. & Chen, L.-C. in *Proceedings of the IEEE conference on computer vision and pattern recognition.* 4510-4520.
133 Targ, S., Almeida, D. & Lyman, K. Resnet in resnet: Generalizing residual architectures. *arXiv preprint arXiv:1603.08029* (2016).
134 Gavai, N. R., Jakhade, Y. A., Tribhuvan, S. A. & Bhattad, R. in *2017 International Conference on Big Data, IoT and Data Science (BID).* 154-158 (IEEE).
135 Jo, Y. *et al.* Data-driven multiplexed microtomography of endogenous subcellular dynamics. *bioRxiv* (2020).

136 Blumenreich, M. S. The white blood cell and differential count. *Clinical Methods: The History, Physical, and Laboratory Examinations. 3rd edition* (1990).
137 Bacusmber, J. W. & Gose, E. E. Leukocyte pattern recognition. *IEEE Transactions on Systems, Man, and Cybernetics*, 513-526 (1972).
138 Nassar, M. *et al.* Label-free identification of white blood cells using machine learning. *Cytometry Part A* **95**, 836-842 (2019).
139 Spitzer, M. H. & Nolan, G. P. Mass cytometry: single cells, many features. *Cell* **165**, 780-791 (2016).
140 Lippeveld, M. *et al.* Classification of human white blood cells using machine learning for stain-free imaging flow cytometry. *Cytometry Part A* **97**, 308-319 (2020).
141 Goswami, N. *et al.* Rapid SARS-CoV-2 Detection and Classification Using Phase Imaging with Computational Specificity. *bioRxiv* (2020).
142 de Haan, K. *et al.* Deep learning-based transformation of H&E stained tissues into special stains. *Nature communications* **12**, 1-13 (2021).
143 Zhang, Z. in *2018 IEEE/ACM 26th International Symposium on Quality of Service (IWQoS)*. 1-2 (IEEE).
144 Tan, M., Pang, R. & Le, Q. V. in *Proceedings of the IEEE/CVF conference on computer vision and pattern recognition.* 10781-10790.
145 Deng, J. *et al.* in *2009 IEEE conference on computer vision and pattern recognition.* 248-255 (Ieee).
146 Hutchison, R. E. & Schexneider, K. Leukocytic disorders. *Henry's Clinical Diagnosis and Management by Laboratory Methods. Philadelphia: Saunders Elsevier* (2011).
147 Chernecky, C. & Berger, B. Differential leukocyte count (diff)-peripheral blood. *Laboratory tests and diagnostic procedures*, 440-446 (2013).
148 Kandel, M. Phase Imaging with Computational Specificity (PICS) for measuring dry mass changes in sub-cellular compartments. *Nat. Commun.(submitted)*.
149 Horstmeyer, R., Ou, X., Zheng, G., Willems, P. & Yang, C. Digital pathology with Fourier ptychography. *Computerized Medical Imaging and Graphics* **42**, 38-43 (2015).
150 Potsaid, B., Bellouard, Y. & Wen, J. T. Adaptive Scanning Optical Microscope (ASOM): A multidisciplinary optical microscope design for large field of view and high resolution imaging. *Optics express* **13**, 6504-6518 (2005).
151 Webb, R. H. & Rogomentich, F. Confocal microscope with large field and working distance. *Applied optics* **38**, 4870-4875 (1999).
152 Alegro, M. *et al.* Automating cell detection and classification in human brain fluorescent microscopy images using dictionary learning and sparse coding. *Journal of neuroscience methods* **282**, 20-33 (2017).
153 Brodin, P. & Christophe, T. High-content screening in infectious diseases. *Current opinion in chemical biology* **15**, 534-539 (2011).
154 Messner, C. B. *et al.* Ultra-fast proteomics with Scanning SWATH. *Nature biotechnology*, 1-9 (2021).
155 Remmelinck, M. *et al.* How could static telepathology improve diagnosis in neuropathology? *Analytical Cellular Pathology* **21**, 177-182 (2000).
156 Gareau, D. S. *et al.* Confocal mosaicing microscopy in Mohs skin excisions: feasibility of rapid surgical pathology. *Journal of biomedical optics* **13**, 054001 (2008).

157 Phillips, Z. F., Dean, S., Recht, B. & Waller, L. High-throughput fluorescence microscopy using multi-frame motion deblurring. *Biomedical optics express* **11**, 281-300 (2020).
158 Ho, J. *et al.* Use of whole slide imaging in surgical pathology quality assurance: design and pilot validation studies. *Human pathology* **37**, 322-331 (2006).
159 Hamamatsu. High throughput imaging in low light applications. *TDI Solutions* (2011).
160 De Moor, P. *et al.* in *2014 IEEE International Electron Devices Meeting.* 4.6. 1-4.6. 4 (IEEE).
161 Iftimia, N. V. *et al.* Adaptive ranging for optical coherence tomography. *Opt. Express* **12**, 4025-4034 (2004).
162 Prabhat, P., Ram, S., Ward, E. S. & Ober, R. J. Simultaneous imaging of different focal planes in fluorescence microscopy for the study of cellular dynamics in three dimensions. *IEEE transactions on nanobioscience* **3**, 237-242 (2004).
163 Abrahamsson, S. *et al.* Fast multicolor 3D imaging using aberration-corrected multifocus microscopy. *Nature methods* **10**, 60-63 (2013).
164 Bouchard, M. B. *et al.* Swept confocally-aligned planar excitation (SCAPE) microscopy for high-speed volumetric imaging of behaving organisms. *Nature photonics* **9**, 113-119 (2015).
165 Nakano, A. Spinning-disk confocal microscopy—a cutting-edge tool for imaging of membrane traffic. *Cell structure and function* **27**, 349-355 (2002).
166 Li, H. *et al.* Fast, volumetric live-cell imaging using high-resolution light-field microscopy. *Biomedical Optics Express* **10**, 29-49 (2019).
167 Martínez-Corral, M. & Javidi, B. Fundamentals of 3D imaging and displays: a tutorial on integral imaging, light-field, and plenoptic systems. *Advances in Optics and Photonics* **10**, 512-566 (2018).
168 Hu, C., Kandel, M. E., Lee, Y. J. & Popescu, G. Synthetic aperture interference light (SAIL) microscopy for high-throughput label-free imaging. *Applied Physics Letters* **119**, 233701 (2021).
169 Farahani, N., Parwani, A. V. & Pantanowitz, L. Whole slide imaging in pathology: advantages, limitations, and emerging perspectives. *Pathology and Laboratory Medicine International* **7**, 23-33 (2015).
170 Lohmann, A. W., Dorsch, R. G., Mendlovic, D., Zalevsky, Z. & Ferreira, C. Space–bandwidth product of optical signals and systems. *JOSA A* **13**, 470-473 (1996).
171 Nguyen, T., Xue, Y., Li, Y., Tian, L. & Nehmetallah, G. Deep learning approach for Fourier ptychography microscopy. *Optics express* **26**, 26470-26484 (2018).
172 Rivenson, Y. *et al.* Deep learning microscopy. *Optica* **4**, 1437-1443 (2017).
173 Xue, Y., Cheng, S., Li, Y. & Tian, L. Reliable deep-learning-based phase imaging with uncertainty quantification. *Optica* **6**, 618-629 (2019).
174 Nehme, E., Weiss, L. E., Michaeli, T. & Shechtman, Y. Deep-STORM: super-resolution single-molecule microscopy by deep learning. *Optica* **5**, 458-464 (2018).
175 Bayramoglu, N., Kaakinen, M., Eklund, L. & Heikkila, J. in *Proceedings of the IEEE International Conference on Computer Vision Workshops.* 64-71.
176 Christiansen, E. M. *et al.* In silico labeling: predicting fluorescent labels in unlabeled images. *Cell* **173**, 792-803. e719 (2018).

177 Ounkomol, C., Seshamani, S., Maleckar, M. M., Collman, F. & Johnson, G. R. Label-free prediction of three-dimensional fluorescence images from transmitted-light microscopy. *Nature methods* **15**, 917-920 (2018).
178 Fanous, M. *et al.* Label-free screening of brain tissue myelin content using phase imaging with computational specificity (PICS). *Apl Photonics* **6**, 076103 (2021).
179 Goswami, N. *et al.* Label-free SARS-CoV-2 detection and classification using phase imaging with computational specificity. *Light: Science & Applications* **10**, 1-12 (2021).
180 Hu, C. *et al.* Live-dead assay on unlabeled cells using phase imaging with computational specificity. *Nature Communications* **13**, 713, doi:10.1038/s41467-022-28214-x (2022).
181 Pinkard, H., Phillips, Z., Babakhani, A., Fletcher, D. A. & Waller, L. Deep learning for single-shot autofocus microscopy. *Optica* **6**, 794-797 (2019).
182 Barbastathis, G., Ozcan, A. & Situ, G. On the use of deep learning for computational imaging. *Optica* **6**, 921-943 (2019).
183 Popescu, G. *Principles of Biophotonics, Volume 1 - "Linear systems and the Fourier transform in optics"*. (IOP Publishing, 2018).